

Dynamics and Stability Analysis of IPMSM Position Sensorless Control for xEV Drive System

A DISSERTATION SUBMITTED TO THE GRADUATE SCHOOL
OF ENGINEERING AND SCIENCE
OF SHIBAURA INSTITUTE OF TECHNOLOGY

BY

DONGWOO LEE

IN PARTIAL FULFILLMENT OF THE REQUIREMENTS
FOR THE DEGREE OF

DOCTOR OF PHILOSOPHY

SEPTEMBER 2019

To my family

Abstract

In this thesis, the new method has been studied for the improvement of dynamic characteristics and stability on the sensorless control of an interior permanent magnet synchronous motor (IPMSM) used as traction motors of electrified vehicle (xEV) today. The xEV is divided into four main categories: battery electric vehicle (BEV), hybrid electric vehicle (HEV), plugin hybrid electric vehicle (PHEV) and fuel cell electric vehicle (FCEV). The inverter control for IPMSM-drives intended for xEV applications has specific features such as reliability and robustness, high torque at low speed and a high power at high speed, wide speed range, fast torque response, high efficiency over the wide speed and torque range, high efficiency for regenerative braking, and so on. Among other things, high reliability and robustness of the control system are basic and essential for a driver safety. To do this, although the fault of sensors utilized traction motor control occurs, the compensation method to ensure normal operation has been proposed continuously. To achieve high performance of xEV traction motor, the precise inverter control using sensor signals is necessary. The sensors comprise four elements: voltage sensor, current sensor, temperature sensor and position of rotor sensor. Conventionally, the position sensor is attached to the rotor shaft mechanically. From this cause, the position sensor has a high probability of sensor fault due to high variation of temperature. Therefore, the algorithm transition from sensed to sensorless control and continuously motor control when the position sensor fault occurs are requested.

This thesis presents the fault detection strategy using difference value between sensor signal and estimated signal. To detect the sensor fault, the sensorless algorithm is operated in parallel. And, the method for fast fault detection and algorithm transition proposes to ensure the stability of control system when the position sensor fault occurs. Also, the design method of controllers for the stable and fast response in sensorless control is analyzed. On the basis of a designed sensorless drive, the new strategies which improve the dynamics of controller and the stability of sensorless control in transient state have been proposed. The effectiveness and feasibility of proposed algorithm and analysis results are verified by computer simulation and experimental results.

Contents

Abstract.....	i
Symbol List.....	vi
Chart Contents.....	viii
Table Contents.....	x
Chapter 1 Introduction.....	1
1.1 Research background.....	1
1.1.1 Social background.....	1
1.1.2 Technical background.....	2
1.2 Research purpose and method.....	3
1.3 Chapter summary.....	5
Chapter 2 Drive theory and modeling of IPMSM.....	6
2.1 Structure and drive theory of IPMSM.....	6
2.2 Mathematical modeling of IPMSM.....	7
2.3 Chapter summary.....	10
Chapter 3 Sensorless control theory of IPMSM.....	11
3.1 Sensorless control method.....	11
3.2 IPMSM model in the rotor reference frame.....	12
3.3 Extended EMF estimation.....	15
3.4 Speed and position estimation.....	16
3.4.1 Analysis of PLL-type estimator.....	16
3.4.2 Bandwidth design of speed & position estimator.....	17
3.5 Current controller bandwidth design.....	18
3.6 Minimum operation speed design.....	19
3.7 Stable gain selection process.....	20
3.8 Chapter summary.....	21

Chapter 4 Dynamic performance and stability improvement.....	22
4.1 Sensorless control performance using gain selection method.....	22
4.1.1 Function block diagram for sensorless control	22
4.1.2 Simulation and experimental results	23
4.2 Improvement of speed response using the proposed speed and position estimator	31
4.2.1 Compensation design of estimated position error	31
4.2.2 Compensation design of estimated speed error.....	33
4.2.3 Simulation and experimental results	35
4.3 Improvement of torque response using current feedback control	39
4.3.1 The design of current feedback control.....	39
4.3.2 Stability analysis of current feedback control.....	40
4.3.3 Simulation and experimental results	41
4.4 Performance comparison on speed and position estimator	43
4.5 Chapter summary	46
Chapter 5 Sensor fault detection and algorithm transition.....	47
5.1 Introduction.....	47
5.2 Encoder sensor fault detection	47
5.3 CUSUM algorithm application	49
5.4 Adaptive threshold design.....	50
5.5 Algorithm transition analysis	52
5.5.1 Experimental results on parameter variation.....	52
5.5.2 Simulation and experimental results	53
5.6 xEV application of proposed algorithms.....	61
5.6 Chapter summary	63
Chapter 6 Conclusion	63
6.1 Conclusion of this paper	63
6.2 Issue and future task.....	63
Reference.....	64
Research achievement	67

Symbol List

V_{as}, V_{bs}, V_{cs}	: instantaneous values of the stator voltages in phases a, b, c respectively
i_{as}, i_{bs}, i_{cs}	: instantaneous values of the stator currents in stator phases a, b, c respectively
$\lambda_{as}, \lambda_{bs}, \lambda_{cs}$: instantaneous values of stator flux linkages in stator phases a, b, c respectively
$\lambda_{abcs(s)}$: instantaneous values of flux linkages between stator winding and stator winding
$\lambda_{abcs(r)}$: instantaneous values of flux linkages between stator winding and rotor winding
ϕ_a, ϕ_b, ϕ_c	: flux linkage of permanent magnet in stator phases a, b, c respectively
ϕ_f	: maximum flux linkage of permanent magnet in stator phase
p	: differential operator
V_d, V_q	: stator voltage in the d - q reference frame
V_γ, V_δ	: stator voltage in the γ - δ reference frame
$\varepsilon_\gamma, \varepsilon_\delta$: back-EMF in the γ - δ reference frame
e_γ, e_δ	: back-EMF of extended EMF equation in the γ - δ reference frame
L_{as}, L_{bs}, L_{cs}	: self inductance of motor
L_{ab}, L_{bc}, L_{ca}	: mutual inductance of motor
L_{ls}	: leakage inductance of motor
L_{ms}	: magnetizing inductance of motor
$T(\theta)$: coordinate transformation matrix
R_s, L_d, L_q	: motor resistance, d - q axis inductance
$\bar{R}, \bar{L}_d, \bar{L}_q$: nominal motor parameters
θ	: rotor position
ω_r	: rotor angular speed
\wedge	: estimated signal value
$\Delta\theta$: position error between the d - q and γ - δ reference frame
$\vec{V}_{\gamma\delta}$: stator voltage vector in the γ - δ reference frame
$\vec{V}_{\gamma\delta}^*$: reference voltage vector in the γ - δ reference frame
$\hat{\vec{E}}_{\gamma\delta}$: back-EMF vector in the γ - δ reference frame
$\vec{I}_{\gamma\delta}$: stator current vector in the γ - δ reference frame
s	: Complex number
g_{ob}	: Disturbance observer bandwidth
k_e	: back-EMF constant
m	: tuning parameter
α_c	: Current controller bandwidth

Symbol List

$\Delta\omega_r^*$: the stable equilibrium points of rotor speed difference by Lyapunov theory
$\Delta\theta^*$: the stable equilibrium points of rotor angle difference by Lyapunov theory
$\Delta\omega_r$: speed estimation error ($=\omega_r - \hat{\omega}_r$)
$\Delta\theta$: position estimation error ($=\theta - \hat{\theta}$)
ρ	: bandwidth of the speed & position estimator
$ \dot{\omega}_r _{max}$: maximal normally occurring acceleration
$ \Delta\theta _{max}$: maximum allowed transient error angle
t_r	: rising time from 10% to 90%
ω_{r_min}	: minimum speed on stable estimator bandwidth
i_{d_min}	: minimum d-axis current under rated speed
i_{q_max}	: maximum q-axis current under rated speed
t_{a_max}	: maximum acceleration time
T_{a_max}	: maximum acceleration torque
T_e	: electromagnetic torque
T_L	: load torque
A	: System matrix
i_q^*	: reference q-axis current in the $d - q$ reference frame
i_δ	: δ -axis current
k_p, k_i	: PI gain for controller
θ_{FC}	: compensation angle for alignment in transient state
\tilde{X}_{ρ_st}	: Max. error value of ρ in steady state
\tilde{X}_{ρ_tr}	: Max. error value of ρ in transient state
\tilde{X}_{max_st}	: Max. error on motor parameter variation in steady state
\tilde{X}_{min_st}	: Min. error on motor parameter variation in steady state
μ_0	: Mean value of signal θ_{err} or ω_{err} before fault
μ_1	: Mean value of signal θ_{err} or ω_{err} after fault
$r(k)$: Absolute value of error signal
$g(k)$: CUSUM function (set to zero value before the fault detection)
Δt_{det}	: fault detection delay time
k	: sample time
t_s	: sampling time
J	: motor inertia
B	: friction coefficient
k	: sample time

Figure List

1.1	Annual Emissions per Vehicle	1
1.2	EV share by region (% of total car sales)	2
1.3	Traction motor and inverter in xEV	3
1.4	Limp-home mode operation	3
2.1	Structure of PMSM.....	6
2.2	Current and position sensor for the vector control of PMSM.....	7
2.3	Analysis model for PMSM	8
3.1	dq-axis equivalent circuit for PMSM	12
3.2	Space vector diagram of PMSM.....	13
3.3	Equivalent form for the extended EMF estimation	14
3.4	Pole placement for 2nd order system approximation	15
3.5	Block diagram of PLL-type estimator	16
4.1	Block diagram of sensorless control based extended EMF method	22
4.2	Experimental setup for sensorless drive	23
4.3	Back-EMF waveforms at 1000 min ⁻¹	24
4.4	Steady state waveforms under 1.8 Nm	25
4.5	Low speed waveforms under 1.8 Nm.....	26
4.6	Steady state waveforms at $\rho=100$ rad/s under 1.8 Nm	27
4.7	Transient response on ρ value at 300 min ⁻¹	28
4.8	Transient response on ρ value at 500 min ⁻¹	28
4.9	Transient response on ρ value at 1500 min ⁻¹	28
4.10	Stable map of sensorless control on ρ vaule from 500 to 1500 min ⁻¹	29
4.11	Comparison results on the minimum ρ vaule from 200 to 1500 min ⁻¹	30
4.12	Speed rampwise response at 1.8 Nm	30
4.13	d -q components of i_δ vector.....	31
4.14	d -q components of i_γ vector.....	32
4.15	Proposed PLL-type estimator using estimated angle and speed error compensation	34
4.16	Transient waveforms of d-q axis current and speed in conventional PLL-type estimator	35
4.17	Transient waveforms of estimated position error and torque in conventional PLL-type estimator	35
4.18	Transient waveforms of d-q axis current and speed with proposed PLL-type estimator	36
4.19	Transient waveforms of estimated position error and torque in proposed PLL-type estimator	36
4.20	Overshoot comparison of estimated speed error in acceleration and deceleration time	37

Figure List

4.21	Transient waveforms in conventional PLL-type estimator.....	38
4.22	Transient waveforms with proposed PLL-type estimator.....	38
4.23	Block diagram of proposed current feedback control.....	39
4.24	Overshoot of estimated position error on rapidly torque variation in sensorless control.....	41
4.25	Overshoot response without angle compensation at 1000 min^{-1}	41
4.26	Overshoot response with angle compensation at 1000 min^{-1}	42
4.27	Overshoot response comparison at 1000 min^{-1} (from 1.8 to 0.1 Nm).....	42
4.28	Comparison results of overshoot value at $\rho=100 \text{ rad/s}$ in transient state.....	43
4.29	Various position and speed estimators using back-EMF estimation method.....	44
4.30	Overshoot waveforms of PLL-type estimator.....	45
5.1	Encoder fault detection using rotor position error.....	48
5.2	Encoder fault detection using rotor speed error.....	48
5.3	Flow chart for encoder fault detection using rotor angle error.....	49
5.4	Block diagram on position and speed sensor fault detection.....	50
5.5	Position error on variation of parameters under 0.1 Nm.....	52
5.6	Position error on variation of parameters under 1.8 Nm.....	52
5.7	Speed and position error on ρ variation under 0.1 Nm.....	53
5.8	Overshoot of dq-axis current during holding time at 1500 min^{-1} under 1.8 Nm.....	53
5.9	Overshoot of $\Delta\hat{\theta}$ on the variation of PLL-type estimator gain ρ under 1.8 Nm.....	54
5.10	Overshoot of estimated position error in algorithm transition under 1.8 Nm.....	54
5.11	Algorithm transition using ω_{err} under 0.1 Nm.....	55
5.12	Threshold value of CUSUM algorithm under 0.1 Nm.....	55
5.13	Overshoot waveforms under 1.8 Nm.....	56
5.14	Waveforms of adaptive threshold method in transient state under 0.1 Nm.....	56
5.15	Overshoot of d-q axis current and holding time in conventional threshold method under 500 min^{-1} & 0.5 Nm.....	57
5.16	Overshoot of d-q axis current and holding time in conventional threshold method under 500 min^{-1} & 1.8 Nm.....	57
5.17	Overshoot of d-q axis current and holding time in conventional threshold method under 1500 min^{-1} & 0.5 Nm.....	58
5.18	Overshoot of d-q axis current and holding time in conventional threshold method under 1500 min^{-1} & 1.8 Nm.....	58
5.19	Overshoot of d-q axis current and rotor angle error in adaptive threshold method under 500 min^{-1} & 0.5 Nm.....	59
5.20	Overshoot of d-q axis current and rotor angle error in adaptive threshold method under 500 min^{-1} & 1.8 Nm.....	59

Figure List

5.21	Overshoot of d-q axis current and rotor angle error in adaptive threshold method under 1500 min^{-1} & 0.5 Nm	60
5.22	Overshoot of d-q axis current and rotor angle error in adaptive threshold method under 1500 min^{-1} & 1.8 Nm	60
5.23	Proposed algorithm application for xEV drive system	61

Table List

Table 3.1	Sensorless algorithm comparison	11
Table 3.2	Speed and position estimation method	12
Table 3.3	Motor parameters	20
Table 4.1	Stable region on torque step response from 0.1 to 1.8 Nm (200 to 1500 min ⁻¹)	29
Table 4.2	Estimator comparison results on the torque and speed variation	45

Chapter 1 Introduction

1.1 Research background

1.1.1 Social background

The carbon emission problems must be solved to reduce global warming. So, many countries already have limits about CO₂ emission of vehicles to protect environment. Eco-friendly vehicles, which are becoming popular all over the world, is one way to achieve significant reductions of CO₂ emissions. Such as figure 1.1, Annual emissions per eco-friendly vehicle are about 50% in comparison with the conventional Gas vehicle. Also, the many vehicle manufactures agreed to reduce about 27% CO₂ emission until 2020 in figure 1^[1]. As an extension of the consensus, the growth of xEV share is expected to be exponential rather than linear from 2020 onwards^[2]. The rapid growth of xEV is caused by the widely charging infrastructure, performance improvements, increased reliability and the cost reduction of electrical components such as lithium-ion batteries^[3]. Especially, the reliability on functional safety and life-cycle management of xEV has been improved to protect a driver because the fault of power electronic devices has caused serious problems in vehicles^[4]^[5]. Therefore, to expend eco-friendly vehicle, the high reliability of traction motor & inverter is required because an electrified powertrain such as traction motor & inverter is continuously exposed to high temperature and vibrations.

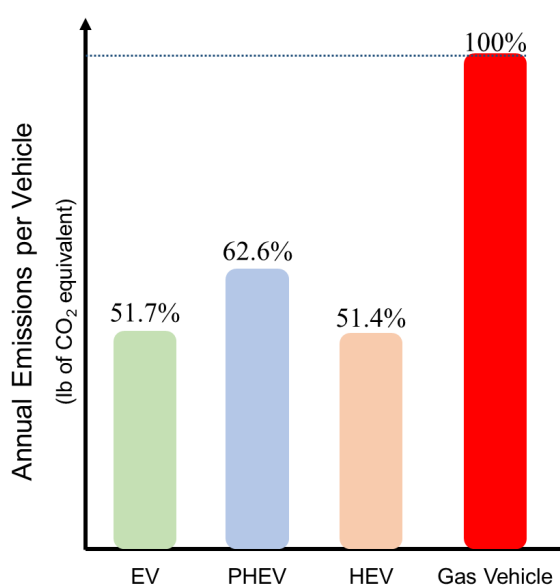


Fig. 1.1 Annual Emissions per Vehicle^[1]

1.1.2 Technical background

During the last decade, permanent magnet synchronous motors (PMSMs) have been widely used in many industrial applications due to their high torque density and efficiency. Recently, PMSMs are receiving especial attentions as powertrain system in automotive applications due to simple structure and high-speed operation range. Hence, automotive companies such as Toyota, Tesla Motors, Nissan, Mitsubishi, BMW, General Motors, etc. have been developing some of xEV using PMSMs^[6]. To achieve high performance of PMSMs used xEV, the vector control of PMSMs is needed. The vector control technique of PMSMs requires the information of rotor position and speed that can be measured by means of position sensors such as hall-effect ICs, resolvers and encoders. However, the position sensors are expensive, complex and very sensitive to mechanical environments^{[7]-[9]}. To solve this problem, the position sensorless schemes have been proposed for PMSMs, which can be classified into two categories. One uses the information available in the back electromotive force (back-EMF) from a middle speed to a high speed range because the magnitude of a back-EMF is rotor position dependent^{[10]-[15]}. Another uses an injected high-frequency voltage signals at standstill and low speed^{[16]-[19]}. Based on this fact, the proper conversion method from back-EMF method to signal injection method or vice versa is needed to allow for stable operation in the all speed range considering speed and load torque variation^{[20][21]}. These sensorless algorithms can be applied to PMSMs control system for high reliability that it is continuous operation regardless of sensor faults as well as fault detection of sensors^{[22]-[32]}. The majority of these contributions have been focused on fault detection and design of fault-tolerant controller for limp-home mode operation^{[33]-[34]}. That means driver of xEV can arrive their destination despite sensor fault. To stable control system of xEV, additional research are required as follow.

- 1) Fast fault detection and algorithm transition when position sensor faults occur.
- 2) Stable gain design of sensorless controllers considering acceleration, deceleration and load variation.
- 3) Compensation method on acceleration, deceleration and load variation.

1.2 Research purpose and method

Recently, in various industry fields such as traction motor control, the position sensorless control is used in parallel with sensed control for automatically reconfigured operation when position sensor fault occurs. To detect the position sensor fault, the residual analysis is discussed because the residual allows the isolation of a faulty sensor directly and insensitive to parameters variations. The residual threshold is defined greater than the amplitude of the residuals which depend on the waveform of measured signal in healthy mode. Hence, the low threshold has good performance on fast fault detection and algorithm conversion^{[23][24]}.

Generally, the residual threshold cannot be decreased unless the overshoot of measured signal has

low value in variation of load torque and speed. Therefore, the analysis on the gain selection of position sensorless controllers is needed to decrease the overshoot value in the transient state. If the proper gain is selected, the stability of sensorless control is increased without the degraded performance of fast dynamic response ^{[21] [35]-[37]}.

The relationship between fast response performance and response stability is a trade-off. So, the stable gain selection in order to ensure the stable control and fast response performance is required through the analysis of controller design of sensorless control system. In the Ref (21), the reasonable values of algorithm conversion between signal injection and back-EMF estimation was set to the start point ω_{ls} from 0.05 PU(Per Unit) to 0.1 PU(1PU is current controller bandwidth) and the end point $\omega_{hs} = 2\omega_{ls}$ and PLL-type estimator bandwidth is selected as $\rho = \alpha_c/30$. And, the maximum allowed acceleration angle to define the PLL-type estimator is decided at 10 degree from his experiment results. However, there is not calculated value. In the Ref. (35), the stable gain selection method of sensorless control system with extended EMF estimation was proposed by new mathematical model. However, the analysis of dynamic response on torque variation is insufficiency. In the Ref. (36), the various sensorless control methods included back-EMF estimation and signal injection method were introduced. But, the paper focuses on the optimized motor design in order to high sensorless drive performance. In the Ref. (37), the saliency tracking observer for position and speed estimation is proposed. The observer bandwidth must have adequate value in order to maintain adequate dynamic stiffness. However, the paper does not include a detailed explanation about the observer bandwidth and the minimum rotor speed in theory and test result does not analyze. The control parameters are very important for the stability and fast dynamic response of sensorless control. So, the parameters should be decided by theoretical considerations.

To estimate the back-EMF of the PMSMs, various approaches such as state observer have been suggested using extended EMF mathematical model ^{[10] [35]}. And, some phase locked loop (PLL) type estimators have been proposed to extract the estimated speed and position from the amplitude of estimated back-EMF ^{[38]-[43]}, but the evaluation at low speed is not included as well as not considering the low overshoot of estimated speed error in torque variation and the proper gain selection of observer and PLL-type estimator in the speed and torque variation is difficult or complicated.

In the Ref. (44), the stable selection method of controller bandwidth is shown by using the analysis of sensorless control system. A higher value of allowable maximum angle error must be selected at low speed for the stable sensorless control. Then, the bandwidth of position and speed estimator is decreased in the transient state that the rotor speed is changed such as acceleration or deceleration. However, the study on a design of the stable estimator bandwidth at constant low speed is not considered. In the Ref. (45), the study shows that the stability of sensorless control could be increased through the use of proposed angle compensator in order to decrease the overshoot of

estimated error angle when the load torque is rapidly changed. However, the research on the estimator bandwidth considering the minimum speed in the steady state is not included.

Recently, for the traction control of electric/hybrid vehicle, fault detection and fault tolerance of position sensor such as encoder and resolver are important not only for the reliability of the control system but also for the normal operation despite position sensor fault. The faulty position sensor should be detected quickly to avoid a serious damage of the control system^{[27] [30]-[33]}. Then, a fast fault detection and isolation is required to eliminate the fault effects. A Fault Detection and Isolation (FDI) method and algorithm transition from sensed to sensorless control have been developed for PMSM drives^{[25] [43]}. If the difference between the measured speed and the estimated speed is higher than a threshold value, the control algorithm should be changed from sensed to sensorless control. However, most of them focused on the faults in steady state of a control system and the threshold value for fault detection was defined in steady state.

1.3 Chapter summary

In this paper, the sensorless control based on the extended EMF model with stable controller gain is studied in the rotor reference frame for fast response at high speed^{[10] [39]}. And the PLL-type estimator is used to obtain the estimated rotor speed and position because the high frequency noise included in the estimated position error and oscillation caused by disturbances can be filtered without mechanical parameter^{[37] [38]}. The selection strategy on the control gains in order to ensure the stable sensorless control of IPMSM in torque and speed variation is defined. Also, the maximum overshoot values of estimated speed error on designed gains of position estimator and the selection method of stable threshold value to detect the fault condition when the motor is accelerate and decelerate are analyzed.

The contributions of this paper is as follows.

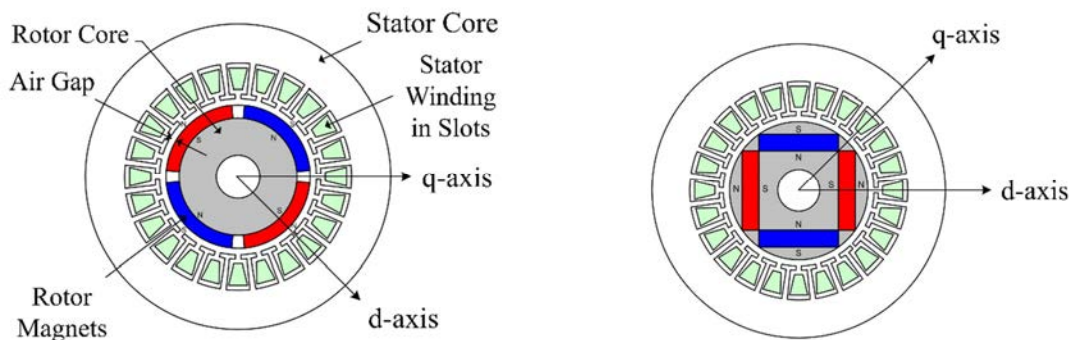
- 1) Stable and nonstop driving of xEV.
 - ✓ Encoder sensor fault detection.
 - ✓ CUSUM algorithm application.
 - ✓ Algorithm transition analysis including motor parameter variations.
- 2) Stable sensorless control of xEV.
 - ✓ Stable gain selection process.
- 3) High performance driving of xEV.
 - ✓ The proposed current feedback control.
 - ✓ The proposed speed and position estimator.

Chapter 2 Drive theory and modeling of IPMSM

2.1 Structure and drive theory of IPMSM

The PMSM motors are divided into two types in accordance with the attached structure of magnet. One is an IPMSM (Interior Permanent Magnet Synchronous Motor) and the other is a SPMSM (Surface Permanent Magnet Synchronous Motor). Figure 2.1 shows the PMSM construction with two pole-pair on the rotor. In case of SPMSM, the permanent magnet is attached to the surface of rotor and the flux path of d-axis is composed of rotor core, rotor magnet, air gap and stator core. But, the flux path of q-axis is made up of rotor core, air gap and stator core without rotor magnet. The rotor magnets of IPMSM are mounted inside the rotor core and the flux path construction of dq-axis is the same as SPMSM. However, although the flux path construction and mechanical configuration are similar to each other, there is a notable difference in the viewpoint of electromagnetic ^{[7][9]}.

The air gap thickness of SPMSM is constant regardless of rotor position because the rotor magnet of SPMSM is attached to the rotor surface. Therefore, the electrical and mechanical structure is symmetry because the reluctance difference of rotor flux is constant. The IPMSM that the permanent magnet is mounted inside the rotor has a higher reluctance of d-axis flux path than the reluctance of q-axis flux path because the effect of additional air gap caused by permanent magnet of d-axis. Hence, the inductance of q-axis is higher than the inductance of d-axis in accordance with high reluctance of d-axis flux path.



(a) Surface Mounted Synchronous Motor (SPMSM) (b) Interior Mounted Synchronous Motor (IPMSM)

Fig. 2.1 Structure of PMSM

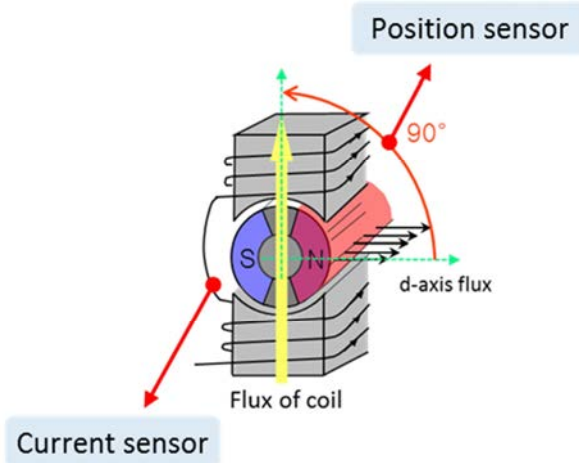


Fig. 2.2 Current and position sensor for vector control of PMSM

Therefore, the IPMSM can obtain a higher torque than the SPMSM because the reluctance torque can be used.

In figure 2.2, we can find the motor operating theory. The coil current induces the q-axis flux related the torque. And for vector control of PMSM, the d-axis flux information is needed such as difference angle between the d-axis flux and permanent magnet flux. Therefore, the rotor position sensor and current sensor are important. A reactance torque of PMSM is generated by an interaction of two magnetic fields (one on the stator and one on the rotor). The stator magnetic field is represented by the magnetic flux and stator current. The magnetic field of the rotor is represented by the magnetic flux of permanent magnets that is constant, except for the field weakening operation.

2.2 Mathematical modeling of IPMSM

To derive the mathematical modeling of PMSM, the analysis model is defined by fig. 4.

The stator 3 phase of PMSM is located in 120 degree between phase and phase. So, the phase variables circuit equation of stator 3 phase winding in abc 3 phase stationary frame is defined as below

$$V_{abcs} = R_s \cdot i_{abcs} + p \cdot \lambda_{abcs} \quad (2.1)$$

where

$$V_{abcs} = \begin{bmatrix} V_{as} \\ V_{bs} \\ V_{cs} \end{bmatrix}, \quad i_{abcs} = \begin{bmatrix} i_{as} \\ i_{bs} \\ i_{cs} \end{bmatrix}, \quad \lambda_{abcs} = \begin{bmatrix} \lambda_{as} \\ \lambda_{bs} \\ \lambda_{cs} \end{bmatrix} \quad (2.2)$$

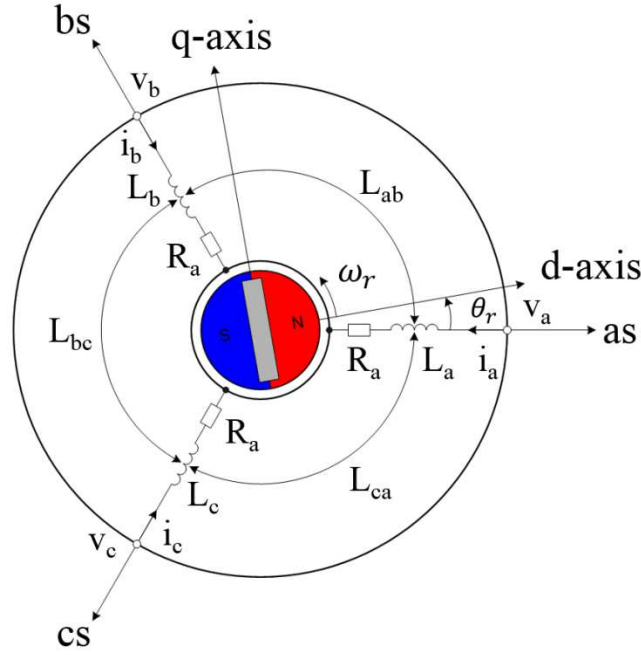


Fig. 2.3 Analysis model for PMSM

Where the magnetic flux linkage by phase current is

$$\lambda_{abc_s} = \lambda_{abc_s(s)} + \lambda_{abc_s(r)} = L_s i_{abc_s} + L_r i_f \quad (2.3)$$

$\lambda_{abc_s(s)}$ is the magnet flux between stator winding and stator winding. And, $\lambda_{abc_s(r)}$ is the magnet flux between stator winding and rotor winding. Also, i_f is the equivalent constant current source in order to substitute $\lambda_{abc_s(r)}$ because the flux caused by permanent magnet is constant.

$$\lambda_{abc_s(s)} = \begin{bmatrix} L_{as} & L_{abs} & L_{acs} \\ L_{abs} & L_{bs} & L_{bcs} \\ L_{acs} & L_{bcs} & L_{cs} \end{bmatrix} \cdot i_{abc_s}$$

$$= \begin{bmatrix} L_s + L_A - L_B \cos 2\theta & -\frac{L_A}{2} - L_B \cos 2\left(\theta - \frac{\pi}{3}\right) & -\frac{L_A}{2} - L_B \cos 2\left(\theta + \frac{\pi}{3}\right) \\ -\frac{L_A}{2} - L_B \cos 2\left(\theta - \frac{\pi}{3}\right) & L_s + L_A - L_B \cos 2\left(\theta - \frac{2\pi}{3}\right) & -\frac{L_A}{2} - L_B \cos 2\theta \\ -\frac{L_A}{2} - L_B \cos 2\left(\theta + \frac{\pi}{3}\right) & -\frac{L_A}{2} - L_B \cos 2\theta & L_s + L_A - L_B \cos 2\left(\theta + \frac{2\pi}{3}\right) \end{bmatrix} \cdot i_{abc_s} \quad (2.4)$$

$$L_{ar}i_f = \phi_f \cos \theta = \phi_a, \quad L_{br}i_f = \phi_f \cos\left(\theta - \frac{2\pi}{3}\right) = \phi_b, \quad L_{cr}i_f = \phi_f \cos\left(\theta + \frac{2\pi}{3}\right) = \phi_c \quad (2.5)$$

$$\frac{d\lambda_{abcs(r)}}{dt} = e_{abcs} = \begin{bmatrix} e_{as} \\ e_{bs} \\ e_{cs} \end{bmatrix} = \begin{bmatrix} p\phi_a \\ p\phi_b \\ p\phi_c \end{bmatrix} = \begin{bmatrix} -\omega_r \phi_f \sin \theta \\ -\omega_r \phi_f \sin\left(\theta - \frac{2\pi}{3}\right) \\ -\omega_r \phi_f \sin\left(\theta + \frac{2\pi}{3}\right) \end{bmatrix} \quad (2.6)$$

Therefore, the voltage equation of PMSM in abc 3-phase stationary reference frame is given by

$$\begin{bmatrix} V_{as} \\ V_{bs} \\ V_{cs} \end{bmatrix} = \frac{d}{dt} \begin{bmatrix} L_{ls} + L_A - L_B \cos 2\theta & -\frac{L_A}{2} - L_B \cos 2\left(\theta - \frac{\pi}{3}\right) & -\frac{L_A}{2} - L_B \cos 2\left(\theta + \frac{\pi}{3}\right) \\ -\frac{L_A}{2} - L_B \cos 2\left(\theta - \frac{\pi}{3}\right) & L_{ls} + L_A - L_B \cos 2\left(\theta - \frac{2\pi}{3}\right) & -\frac{L_A}{2} - L_B \cos 2\theta \\ -\frac{L_A}{2} - L_B \cos 2\left(\theta + \frac{\pi}{3}\right) & -\frac{L_A}{2} - L_B \cos 2\theta & L_{ls} + L_A - L_B \cos 2\left(\theta + \frac{2\pi}{3}\right) \end{bmatrix} \cdot \begin{bmatrix} i_{as} \\ i_{bs} \\ i_{cs} \end{bmatrix} + \begin{bmatrix} -\omega_r \phi_f \sin \theta \\ -\omega_r \phi_f \sin\left(\theta - \frac{2\pi}{3}\right) \\ -\omega_r \phi_f \sin\left(\theta + \frac{2\pi}{3}\right) \end{bmatrix} \quad (2.7)$$

As the transient-state analysis of PMSM is difficult in abc 3-phase stationary reference frame due to complicated equation, the transformation matrix $T(\theta)$ can be used to transfer the 3-phase reference frame to 2-phase reference frame. The matrix can be defined as below

$$T(\theta) = \frac{2}{3} \begin{bmatrix} \cos \theta & \cos\left(\theta - \frac{2\pi}{3}\right) & \cos\left(\theta + \frac{2\pi}{3}\right) \\ -\sin \theta & -\sin\left(\theta - \frac{2\pi}{3}\right) & -\sin\left(\theta + \frac{2\pi}{3}\right) \\ \frac{1}{\sqrt{2}} & \frac{1}{\sqrt{2}} & \frac{1}{\sqrt{2}} \end{bmatrix} \quad (2.8)$$

The voltage equation of PMSM in stationary reference frame is given as follows

$$T(0) \cdot V_{abcs} = T(0) \cdot R_s \cdot i_{abcs} + T(0) \cdot p \cdot \lambda_{abcs} \quad (2.9)$$

$$V_{\alpha\beta} = R_s \cdot i_{\alpha\beta} + T(0) \cdot \frac{dT(0)^{-1} \lambda_{\alpha\beta}}{dt} = R_s \cdot i_{\alpha\beta} + \frac{d\lambda_{\alpha\beta}}{dt} \quad (2.10)$$

Where

$$\lambda_{\alpha\beta} = \begin{bmatrix} L_{ls} + \frac{3}{2}(L_A - L_B \cos 2\theta) & -\frac{3}{2}L_B \sin 2\theta \\ -\frac{3}{2}L_B \sin 2\theta & L_{ls} + \frac{3}{2}(L_A + L_B \cos 2\theta) \end{bmatrix} \begin{bmatrix} i_\alpha \\ i_\beta \end{bmatrix} + \lambda_f \begin{bmatrix} \cos \theta \\ \sin \theta \end{bmatrix} \quad (2.11)$$

Therefore

$$\begin{bmatrix} V_{ds}^s \\ V_{qs}^s \end{bmatrix} = \begin{bmatrix} V_\alpha \\ V_\beta \end{bmatrix} = \begin{bmatrix} R_s + p(L_0 - L_1 \cos 2\theta) & pL_1 \sin 2\theta \\ pL_1 \sin 2\theta & R_s + p(L_0 - L_1 \cos 2\theta) \end{bmatrix} \begin{bmatrix} i_\alpha \\ i_\beta \end{bmatrix} + \omega_r \lambda_f \begin{bmatrix} -\sin \theta \\ \cos \theta \end{bmatrix} \quad (2.12)$$

$$L_0 = L_{ls} + 1.5L_A, \quad L_1 = -1.5L_B$$

The voltage equation in rotating d-q reference frame is represented by matrix equation $T(\theta)$

$$T(\theta_r) \cdot V_{abcs} = T(\theta_r) \cdot R_s \cdot i_{abcs} + T(\theta_r) \cdot p \cdot \lambda_{abcs} \quad (2.13)$$

$$\begin{bmatrix} V_{ds}^r \\ V_{qs}^r \end{bmatrix} = \begin{bmatrix} V_d \\ V_q \end{bmatrix} = \begin{bmatrix} R_s + pL_d & -\omega_r L_q \\ \omega_r L_d & R_s + pL_q \end{bmatrix} \cdot \begin{bmatrix} i_{ds}^r \\ i_{qs}^r \end{bmatrix} + \begin{bmatrix} 0 \\ \omega_r \phi_f \end{bmatrix} \quad (2.14)$$

Also, the input power can be defined in rotor reference frame as below

$$P_{in} = \frac{3}{2}(V_{ds}^r i_{ds}^r + V_{qs}^r i_{qs}^r) = \frac{3}{2}R_s \left((i_{ds}^r)^2 + (i_{qs}^r)^2 \right) + \frac{3}{2} \frac{L_s}{2} \frac{d}{dt} \left((i_{ds}^r)^2 + (i_{qs}^r)^2 \right) + \frac{3}{2} \omega_r \phi_f i_{ds}^r \quad (2.15)$$

The torque equation of PMSM in rotor reference frame is below equation ^{[46] [52]}.

$$T_e = \frac{3}{2} P \left(\phi_f i_{qs}^r + (L_d - L_q) \cdot i_{ds}^r i_{qs}^r \right) \quad (2.16)$$

2.3 Chapter summary

In this chapter, the electrical and mechanical structure of PMSM is introduced and the electrical characteristics are defined on mounted type of permanent magnet. Also, the mathematical modeling of PMSM is determined by equations.

Chapter 3 Sensorless control theory of IPMSM

3.1 Sensorless control method

Sensorless control methods are composed fundamental excitation method such as Flux estimation, back-EMF(Electro-Motive Force) estimation included observer, etc. and saliency and signal injection method such as injects discrete voltage signals, continuous sinusoidal signal injection, HF(High Frequency) square-wave signal injection. The various estimators for estimating back-EMF and rotor position of PMSM have been investigated such as observer based estimation method with state filter and extended EMF estimation method with disturbance observer. However, the back-EMF magnitude is very low at extremely low speed and rotor standstill condition even if it is accurately estimated. To overcome this demerit, the high frequency signal injection-based method has been proposed as a high performance method at low speed or stall condition. However, the injection-based method essentially has the disadvantage of frequency noise and additional power losses because the injected signal is applied. In addition, if the spatial saliency of inductance does not exist in the PMSM, the injection-based method is difficult to use for the sensorless control. The transition region from to back-EMF method to signal injection method or vice versa is frequently selected based on test results considering the range of motor speed where both back-EMF method and injected signal method are properly worked ^{[46]-[50] [65]-[71]}.

Among the many methods, back-EMF estimation and HF signal injection are generally used to sensorless drive without position and speed sensor. In accordance with the control method, various advantage and disadvantage can be defined such as Table 3.1 and Table 3.2. So, this paper will apply to PLL-type estimator and disturbance observer in rotor reference frame in order to improve the transient performance ^{[57]-[62]}.

Table 3.1 Sensorless algorithm comparison

Estimator	Advantage	Disadvantage
Signal injection type	Very low speed operation	Increase the complexity & cost
Observer based type	Strong robustness & high accuracy over full speed region	Low speed region & stall condition

Table 3.2 Speed and position estimation method

Estimator	Advantage	Disadvantage
Signal injection type	Very low speed operation	Increase the complexity & cost
Observer based type	Strong robustness & high accuracy over full speed region	Low speed region & stall condition

3.2 IPMSM model in the rotor reference frame

From the voltage equation (2.14) in rotor reference frame, it can be noted that the coupling terms, $-\omega_r L_q i_q^e$ and $\omega_r L_d i_d^e$, are originated from rotating the coordinate and they make an interference between d-axis and q-axis dynamics. The rotor flux linkage is equivalently expressed as a product of d-axis inductance L_d and a virtual current i_f as depicted in the equation as below.

$$\phi_f = L_d i_f \quad (3.1)$$

With i_f , a PMSM equivalent circuit can be depicted as shown in the Figure 3.1.

In IPMSM, the inductance changes depending on the rotor position. The flux linkage change is described by a sinusoidal function of the rotor angle θ . As considering the flux linkage of a-phase winding for different rotor positions, we can note that the effective air gap changes, as the rotor rotates.

The effective air gap reaches its peak, when the flux lines cross the cavities at the right angle. However, it reduces to the minimum value, when the lines do not cross the cavities^[46].

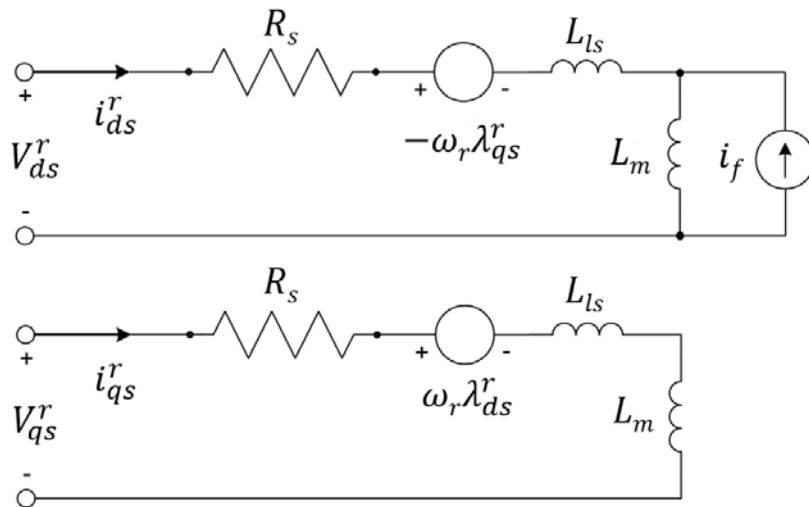
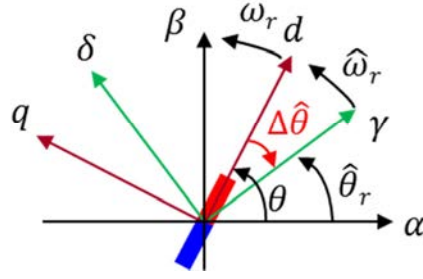


Fig. 3.1 d-q axis equivalent circuit for PMSM


 Fig. 3.2 Space vector diagram of PMSM ^[10]

The α - β and d - q frames represent the stationary and the rotor reference frames, respectively. The γ - δ frame is an estimated frame used in sensorless vector control using the rotor reference frame. The relationship between the three frames is shown in Figure 3.2. $\Delta\theta$ is the position error between the d - q and γ - δ reference frame.

The voltage equation of the IPMSM in the estimated rotating reference frame (γ - δ frame) is represented as follow ^[10]:

$$\begin{bmatrix} V_\gamma \\ V_\delta \end{bmatrix} = \begin{bmatrix} R_s + pL_d & -\omega_r L_q \\ \omega_r L_d & R_s + pL_q \end{bmatrix} \cdot \begin{bmatrix} i_\gamma \\ i_\delta \end{bmatrix} + \begin{bmatrix} \mathcal{E}_\gamma \\ \mathcal{E}_\delta \end{bmatrix} \quad (3.2)$$

$$\begin{aligned} \begin{bmatrix} \mathcal{E}_\gamma \\ \mathcal{E}_\delta \end{bmatrix} &= \omega_r \phi_f \begin{bmatrix} -\sin \Delta\theta \\ \cos \Delta\theta \end{bmatrix} + L_1 p \begin{bmatrix} i_\gamma \\ i_\delta \end{bmatrix} + \omega_r L_2 \begin{bmatrix} i_\gamma \\ i_\delta \end{bmatrix} + (\hat{\omega}_r - \omega_r) L_3 \begin{bmatrix} i_\gamma \\ i_\delta \end{bmatrix} \\ L_1 &= \begin{bmatrix} -(L_d - L_q) \sin^2 \Delta\theta & (L_d - L_q) \sin \Delta\theta \cdot \cos \Delta\theta \\ (L_d - L_q) \sin \Delta\theta \cdot \cos \Delta\theta & (L_d - L_q) \sin^2 \Delta\theta \end{bmatrix} \\ L_2 &= \begin{bmatrix} -(L_d - L_q) \sin \Delta\theta \cdot \cos \Delta\theta & -(L_d - L_q) \sin^2 \Delta\theta \\ -(L_d - L_q) \sin^2 \Delta\theta & (L_d - L_q) \sin \Delta\theta \cdot \cos \Delta\theta \end{bmatrix} \\ L_3 &= \begin{bmatrix} (L_d - L_q) \sin \Delta\theta \cdot \cos \Delta\theta & -L_q \cos^2 \Delta\theta - L_q \sin^2 \Delta\theta \\ L_d \sin^2 \Delta\theta + L_q \cos^2 \Delta\theta & -(L_d - L_q) \sin \Delta\theta \cdot \cos \Delta\theta \end{bmatrix} \end{aligned} \quad (3.3)$$

In (3.3), the voltage equation in γ - δ frame is simple in a nonsalient pole motor. However, in the salient pole motor such as IPMSM, they are very complex equation. To solve this problem, an extended EMF method is proposed as below ^[10].

In (3.2), the voltage equation of the IPMSM in the d - q frame can be derived as follow

$$\begin{bmatrix} V_d \\ V_q \end{bmatrix} = \begin{bmatrix} R_s + pL_d & -\omega_r L_q \\ \omega_r L_q & R_s + pL_d \end{bmatrix} \cdot \begin{bmatrix} i_d \\ i_q \end{bmatrix} + \begin{bmatrix} 0 \\ E_{ex} \end{bmatrix} \quad (3.4.a)$$

$$E_{ex} = \omega_r \left[(L_d - L_q) i_d + \phi_f \right] - (L_d - L_q) (p i_q) \quad (3.4.b)$$

Where $p = d/dt$, and E_{ex} is the extended EMF voltage.

The voltage equation in the γ - δ frame can be obtained as (3.5.a), (3.5.b):

$$\begin{bmatrix} V_\gamma \\ V_\delta \end{bmatrix} = \begin{bmatrix} R + pL_d & -\omega_r L_q \\ \omega_r L_q & R + pL_d \end{bmatrix} \cdot \begin{bmatrix} i_\gamma \\ i_\delta \end{bmatrix} + \begin{bmatrix} e_\gamma \\ e_\delta \end{bmatrix} \quad (3.5.a)$$

$$\begin{bmatrix} e_\gamma \\ e_\delta \end{bmatrix} = E_{ex} \cdot \begin{bmatrix} -\sin \Delta\theta \\ \cos \Delta\theta \end{bmatrix} + (\hat{\omega}_r - \omega_r) L_d \begin{bmatrix} -i_\delta \\ i_\gamma \end{bmatrix} \quad (3.5.b)$$

Under the steady-state condition, the last term of (3.5.b) can be ignored since the speed error could be sufficiently small. So, (3.5.a) can be rewritten as (3.6)

$$\begin{bmatrix} V_\gamma \\ V_\delta \end{bmatrix} = \begin{bmatrix} R + pL_d & -\omega_r L_q \\ \omega_r L_q & R + pL_d \end{bmatrix} \cdot \begin{bmatrix} i_\gamma \\ i_\delta \end{bmatrix} + E_{ex} \cdot \begin{bmatrix} -\sin \Delta\theta \\ \cos \Delta\theta \end{bmatrix} \quad (3.6)$$

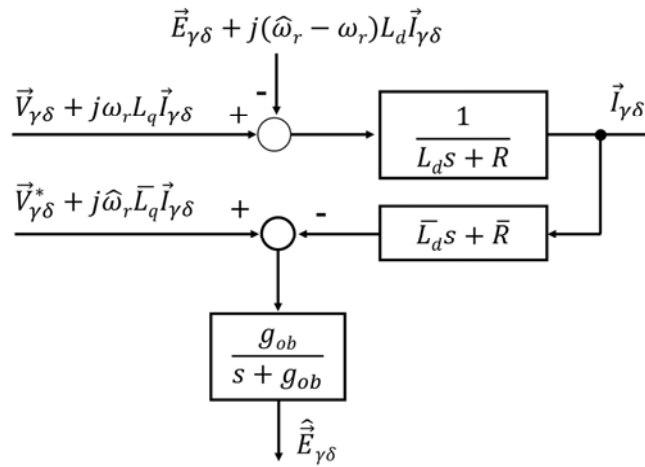


Fig. 3.3 Equivalent form for extended EMF estimation ^[10]

From the estimated E_{ex} in the γ - δ frame, the estimated position error $\Delta\hat{\theta}$ can be derived by (3.7)

$$\Delta\hat{\theta} = \tan^{-1}\left(\frac{-E_{ex} \cdot \sin \Delta\theta}{E_{ex} \cdot \cos \Delta\theta}\right) = -\tan^{-1}\left(\frac{\hat{e}_\gamma}{\hat{e}_\delta}\right) \quad (3.7)$$

3.3 Extended EMF estimation

The equivalent form for the estimation of extended EMF using disturbance observer is shown in Fig. 3.3. The disturbance observer contains a differential operator in order to obtain the reverse model of the system. Hence, the disturbance observer should include a low-pass and a high-pass filters as shown (3.8) for minimizing the negative effects of the differential operation. Therefore, the proper selection of observer gain g_{ob} is important to improve the transient stability^{[10]-[14] [35]-[38]}.

$$\hat{\vec{E}}_{\gamma\delta} = \frac{g_{ob}}{s + g_{ob}} \left(\vec{V}_{\gamma\delta}^* + j\hat{\omega}_r \bar{L}_q \cdot \vec{I}_{\gamma\delta} - \bar{R} \cdot \vec{I}_{\gamma\delta} \right) - \frac{s}{s + g_{ob}} \left(\bar{L}_d \cdot g_{ob} \cdot \vec{I}_{\gamma\delta} \right) \quad (3.8)$$

The observer gain g_{ob} should be sufficiently larger than the angular speed of rotor ω_r . In general, the g_{ob} is set as two times of ω_r . However, the minimum value should be considered. So, the g_{ob} can be defined as (3.9).

$$|\omega_r| \cdot n \leq g_{ob} < \alpha_c, \quad \left(n = k_e / \sqrt{m_{ob}^2 - (L_d - L_q)^2 |i|_{\max}^2} \right) \quad (3.9)$$

where α_c is the current controller bandwidth and k_e is the back-EMF constant. Also, m_{ob} is the tuning parameter for the reliable back-EMF estimation and $|i|_{\max}$ is the maximum stator current^[35].

3.4 Speed and position estimation

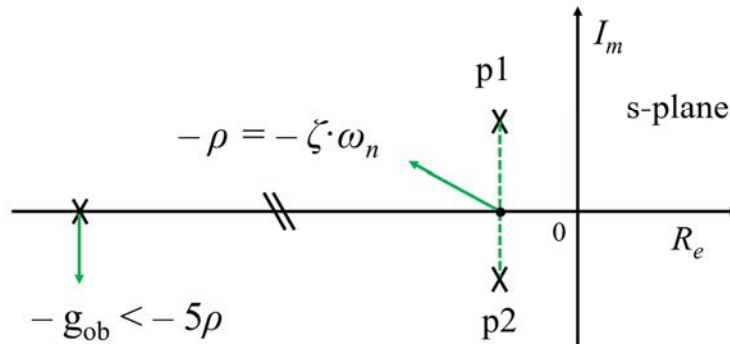


Fig. 3.4 Pole placement for 2nd order system approximation

3.4.1 Analysis of PLL-type estimator

The estimation of the rotor position and speed from the output value of disturbance observer can be defined by using PLL-type estimator ^{[10] [37]-[41]}. When the difference between estimated position error and actual position error is very small, (3.13) can be derived from Fig. 3.4.

$$\Delta\hat{\theta} \approx \Delta\theta = \theta - \hat{\theta} \quad (3.10)$$

$$\hat{\theta} = \frac{K_{ep} \cdot s + K_{ei}}{s^2 + K_{ep} \cdot s + K_{ei}} \cdot \theta \quad (3.11)$$

where K_{ep} and K_{ei} are PI gain for PLL-type estimator. s is the complex frequency variable associated with the Laplace transform.

In Fig. 3.5, the PLL-type estimator consists of a PI controller and integrator to generate the estimated rotor position $\hat{\theta}$ and estimated angular speed $\hat{\omega}_r$. In general, the integrator output $\hat{\omega}_r$ of PI regulator is used as the estimated speed for speed control and extended EMF estimation. The $\hat{\theta}$ is used to estimate the real rotor angle and to perform the coordinate transformations ^[10].

This $\hat{\theta}$ and $\hat{\omega}_r$ can be used to achieve synchronism between the γ - δ frame and the d-q frame. From (3.11) with Fig. 3.5, the estimated rotor angular speed $\hat{\omega}_r$ is calculated as (3.12).

$$\hat{\omega}_r = \left(\frac{g_{ob}}{s + g_{ob}} \right) \cdot \frac{K_{ei}}{s} \cdot \Delta\hat{\theta} \approx \left(\frac{g_{ob}}{s + g_{ob}} \right) \cdot \frac{K_{ei}}{s} \cdot (\theta - \hat{\theta}) \quad (3.12)$$

By substituting (3.11) into (3.12) and using the reasonable assumption that the g_{ob} of five times higher than an PLL-type estimator bandwidth is selected, the effect of g_{ob} in transfer function of system can be ignored and the $\hat{\omega}_r$ is given by

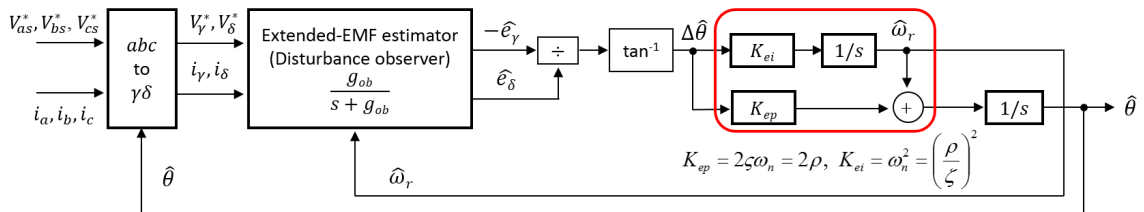


Fig. 3.5 Block diagram of PLL-type estimator

$$\hat{\omega}_r \approx \left(\frac{K_{ei} \cdot s}{s^2 + K_{ep} \cdot s + K_{ei}} \right) \cdot \theta = \left(\frac{K_{ei}}{s^2 + K_{ep} \cdot s + K_{ei}} \right) \cdot \omega_r \quad (3.13)$$

In order to analyze the stable gain of transfer function in (3.13), the standard form of 3rd order characteristic polynomial is compared such as (3.14).

$$c(s) = (s^2 + K_{ep} \cdot s + K_{ei}) = (s^2 + 2\zeta\omega_n s + \omega_n^2) \quad (3.14)$$

$$\therefore K_{ep} = 2\zeta\omega_n, \quad K_{ei} = \omega_n^2 \quad (3.15)$$

where ζ is damping ratio and ω_n is natural frequency. To guarantee the stability and tracking performance of estimator, ζ and ω_n should be taken into consideration. If the ζ is equal to 1, the stable system without oscillation can be obtained because two poles are located at $-\rho$. Therefore, the stability and dynamic response will be defined by selecting only ω_n value.

3.4.2 Bandwidth design of speed & position estimator

In order to set the estimator bandwidth, it is assumed that the actual rotor speed changes rampwise during a short interval of time and the acceleration of rotor speed is constant. Besides, if acceleration of estimated speed error $\Delta\dot{\omega}_r$ and estimated position error $\Delta\dot{\theta}$ are equal to 0, the asymptotic tracking errors can be obtained around the equilibrium point $\Delta\omega_r^* = \Delta\theta^* = 0$ ^{[20] [21] [37]}.

$$\Delta\omega_r^* = \frac{2\dot{\omega}_r}{\rho}, \quad \Delta\theta^* = \sin^{-1} \frac{\dot{\omega}_r}{\rho^2} \quad (3.16)$$

where $\Delta\omega_r^*$ and $\Delta\theta^*$ are the stable equilibrium points considering the error dynamics by Lyapunov principle. Also ρ is bandwidth of PLL-type estimator for the speed & position estimation. From (3.16), a rule for ρ value selection on the assumption that the acceleration is constant over a short time is given by (3.17).

$$\rho = \sqrt{\frac{|\dot{\omega}_r|_{\max}}{\sin|\Delta\theta|_{\max}}} \quad (3.17)$$

where $|\dot{\omega}_r|_{\max}$ is the allowed maximum acceleration and $|\Delta\theta|_{\max}$ is the allowed maximum error angle in the transient. $|\Delta\theta|_{\max}$ can be defined as (3.18).

$$|\Delta\theta|_{\max} = \Delta\omega_{r,\max} \cdot \Delta t_s \quad (3.18)$$

where $\Delta\omega_{r,\max}$ is the deference speed during acceleration time and Δt_s is the speed sampling time.

The state equation of the motor dynamics is given in (3.19).

$$\frac{d\omega_r}{dt} = \frac{1}{J}T_e - \frac{B}{J}\omega_r - \frac{1}{J}T_L \quad (3.19)$$

where J is the motor inertia, B is the friction coefficient, T_e is the electromagnetic torque and T_L is the load torque. If the load torque and friction coefficient are zero, the maximum acceleration of motor is selected. So, the maximum angular acceleration $|\dot{\omega}_r|_{\max}$ can be determined as below

$$\frac{d\omega_r}{dt} = \frac{1}{J}T_e \rightarrow |\dot{\omega}_r|_{\max} = \frac{T_{a,\max}}{J} \quad (3.20)$$

where $T_{a,\max}$ is allowed maximum acceleration torque.

3.5 Current controller bandwidth design

The feedback loop of current controller can be approximated as first-order systems with bandwidth, and the relation between the bandwidth for feedback loop of current controller α_c and the rising time t_r is then given by (3.22). The t_r is defined by (3.21). In general, the α_c should be designed as 10 times higher than the maximum bandwidth of ρ for the estimator performance ^[43].

$$\begin{aligned}
 0.1 &= e^{-\alpha_c \cdot t_{r1}} \rightarrow t_{r1} = (1/\alpha_c) \cdot \ln 10 \\
 0.9 &= e^{-\alpha_c \cdot t_{r2}} \rightarrow t_{r2} = (1/\alpha_c) \cdot (\ln 10 - \ln 9) \\
 \therefore t_r &= t_{r2} - t_{r1} = (1/\alpha_c) \cdot \ln 9
 \end{aligned} \tag{3.21}$$

$$\alpha_c = \frac{\ln 9}{t_r} \tag{3.22}$$

3.6 Minimum operation speed design

The error dynamics are linearized about the equilibrium point by Lyapunov theory ($\Delta\omega_r^* = \Delta\theta^* = 0$) as ^{[21] [35] [43] [47]-[48] [60]}

$$\begin{bmatrix} \Delta\dot{\hat{\omega}}_r \\ \Delta\dot{\hat{\theta}} \end{bmatrix} = \begin{bmatrix} -2\rho K & -\rho^2 \\ 1-4K & -2\rho \end{bmatrix} \cdot \begin{bmatrix} \Delta\hat{\omega}_r \\ \Delta\hat{\theta} \end{bmatrix} \tag{3.23}$$

$$K = \frac{\rho(L_q - L_d)i_q}{2\omega_r(\psi - (L_q - L_d) \cdot i_d)} \tag{3.24}$$

In (3.24), using the system matrix, the characteristic polynomial is defined such as

$$c(s) = \det(sI - A) = s^2 + 2\rho(1 + K)s + \rho^2 \tag{3.25}$$

If the stable root locus of characteristic polynomial and the impact of stability when K is varied consider, the K value is given by $K > -0.3$ for sufficient damping. Hence, the minimum speed $\omega_{r,min}$ on stable estimator bandwidth can be obtained as

$$\omega_{r,min} = \frac{5\rho(L_q - L_d) \cdot i_{q,max}}{3(\psi - (L_q - L_d) \cdot i_{d,min})} \tag{3.26}$$

where $i_{q,max}$ is maximum q-axis current under rated speed and $i_{d,min}$ is minimum d-axis current under rated speed. Therefore, the bandwidth for stable performance of PLL-type estimator can be defined from (3.15), (3.17), (3.18) and (3.20). Also, the current controller bandwidth and minimum speed can be selected by (3.22) and (3.26).

3.7 Stable gain selection process

On the base of analysis results of previous section, the stable gain using motor parameter (Table 3.3) can be defined as below ^[44]

- 1) Select to the rising time t_r considering the overshoot value and fast response of current.

$$: t_r = 0.7 \text{ ms from rising time of d-q axis current}$$

- 2) Select to the acceptable α_c from (3.22).

$$: \alpha_c = \ln 9 / t_r = \ln 9 / 0.7 \text{ ms} = 3139 \text{ rad/s}$$

- 3) Select to the $|\Delta\theta|_{\max}$ from (3.18).

$$: |\Delta\theta|_{\max} = \Delta\omega_{r,\max} \times \Delta t_s = 157.1 \text{ rad/s} \times 1 \text{ ms} \approx 10^\circ$$

- 4) Select to the $|\dot{\omega}_r|_{\max}$ from (3.20).

$$: |\dot{\omega}_r|_{\max} = T_{a,\max} / J = 3.4 \text{ Nm} / 0.001641 \text{ kg}\cdot\text{m}^2 = 2072.5 \text{ rad/s}^2$$

- 5) Select to the ρ considering acceptably fast acceleration from (3.17).

$$: \rho = \sqrt{\frac{|\dot{\omega}_r|_{\max}}{\sin|\Delta\theta|_{\max}}} = 109 \text{ rad/s} < 377 \text{ rad/s} \rightarrow \rho = 100 \text{ rad/s}$$

- 6) Select to the disturbance observer bandwidth g_{ob} from (3.9) and $5 \cdot \rho_{\max} < g_{ob,\min}$ from Fig. 3.4.

$$: |\omega_r| \cdot n \leq g_{ob} < \alpha_c, \quad 5\rho_{\max} < g_{ob,\min} \rightarrow 977 \text{ rad/s} \leq g_{ob} < 3139 \text{ rad/s} \rightarrow g_{ob} = 1000 \text{ rad/s}$$

- 7) Check the minimum speed for stable for stable estimator bandwidth from (3.26).

$$: \omega_{r,\min} = \frac{5\rho(L_q - L_d) \cdot i_{q,\max}}{3(\psi - (L_q - L_d) \cdot i_{d,\min})} = 49.88 \text{ rad/s} = 476 \text{ min}^{-1} \rightarrow 500 \text{ min}^{-1}$$

Table 3.3 Motor parameters

Parameter	Value
Number of poles	4
Rated Speed [min^{-1}]	1500
Stator resistance [Ω]	0.814
d-axis Inductance [mH]	10.7
q-axis Inductance [mH]	26.3
Back-EMF constant [$\text{V}\cdot\text{s}/\text{rad}$]	0.14693
Rotor inertia [$\text{kg}\cdot\text{m}^2$]	0.001641
Rated torque [Nm]	1.8

3.8 Chapter summary

In this chapter, the basic theory of IPMSM for sensorless control is discussed. The estimators to define the extended EMF estimation and speed & position estimation are studied. Also, the stable gain selection process is proposed to robust sensorless control considering the design of various controllers.

The error dynamics can be linearized about the equilibrium point by Lyapunov theory. And, from a system matrix of state equation, the acceptable minimum speed considering PLL-type estimator bandwidth is defined by characteristic polynomial and stability impact.

Chapter 4 Dynamic performance and stability improvement

4.1 Sensorless control performance using gain selection method

4.1.1 Functional block diagram for sensorless control

For an IPMSM drive, these sensors typically measure rotor position and speed, phase current and DC-link voltage. Although this paper focuses on sensorless control without position and speed sensor, all sensors are used to compare the performance of sensorless control based on the proposed method. The configuration of the sensorless drive system for simulation and experiment is shown in Fig. 4.1. The disturbance observer block is used for back-EMF estimation in $\gamma\delta$ -axis reference frame using estimated $\gamma\delta$ -axis current and rotor speed. The PLL-type estimator calculates estimated signals of rotor position and speed from the observed back-EMF. The estimated signals are compared to actual signals from encoder to verify the accuracy of estimated information. All the gains of each controller and observer are selected by the proposed gain selection process as mentioned in section 3.7 [14] [62].

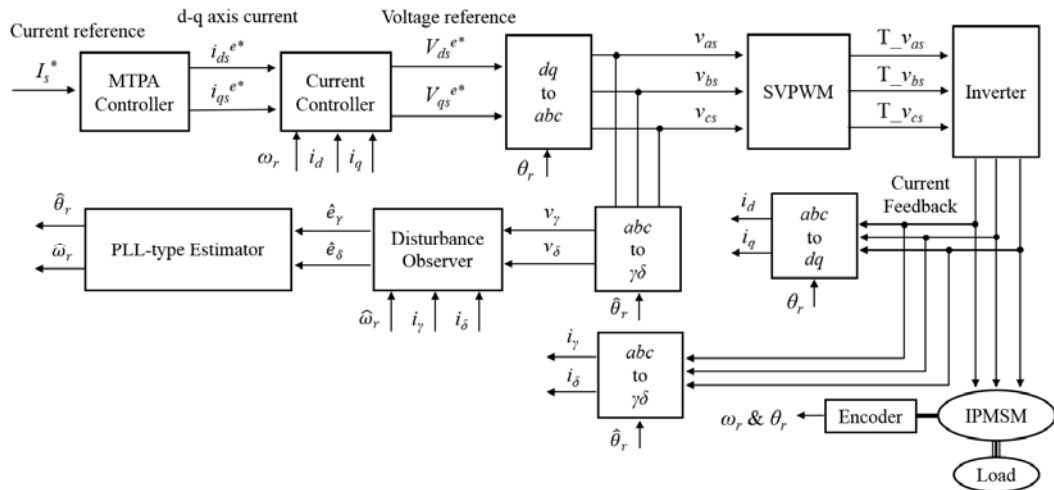


Fig. 4.1 Block diagram of sensorless control based extended EMF method

4.1.2 Simulation and experimental results

To evaluate the feasibility of proposed gain selection method, the experimental setup shown in Fig. 4.2 has been considered. The rating specifications of the 4-pole IPMSM are 1.8 Nm, 3Arms and 1500 r/min such as Table 3.3. The encoder is used for verifying the estimated rotor angle and speed instead of resolver. Also, the voltage reference V_{ds}^{e*} , V_{qs}^{e*} are used for the input factors of disturbance observer instead of V_γ , V_δ to decrease the noise effect. And, the switching frequency of the inverter is set to 10 kHz. From stable gain selection process, the sensorless control parameters can be set as below

$$t_r = 0.7 \text{ ms}, \quad \alpha_c = 3140 \text{ rad/s}, \quad |\Delta\theta|_{max} = 10 \text{ degree}, \quad |\dot{\omega}_r|_{max} = 2073 \text{ rad/s}^2, \quad g_{ob} = 1000 \text{ rad/s}, \\ m_{ob} = 0.12, \quad \rho = 100 \text{ rad/s}, \quad \omega_{r,min} = 476 \text{ min}^{-1} \doteq 500 \text{ min}^{-1}$$

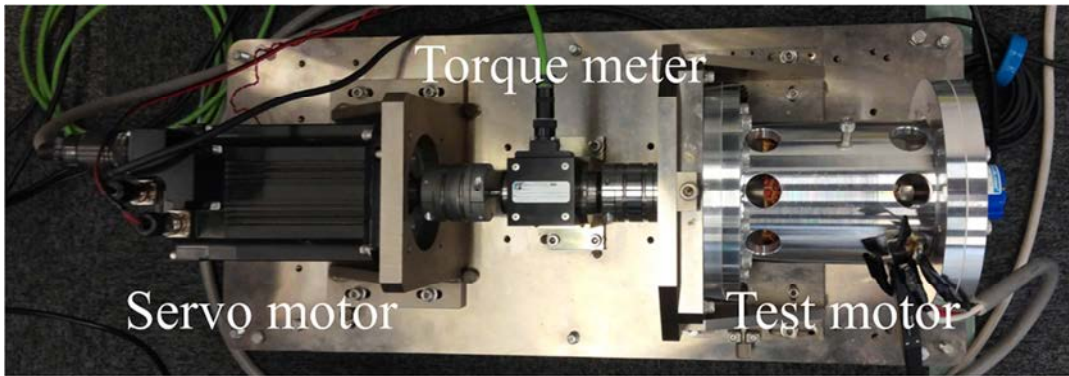
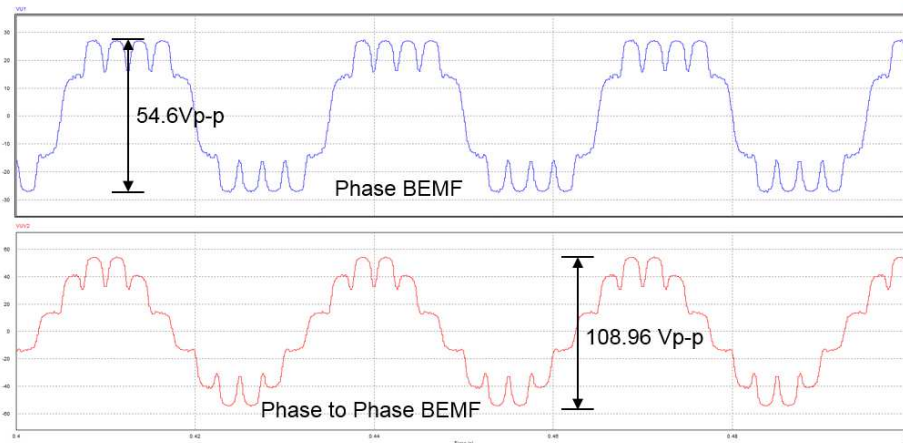
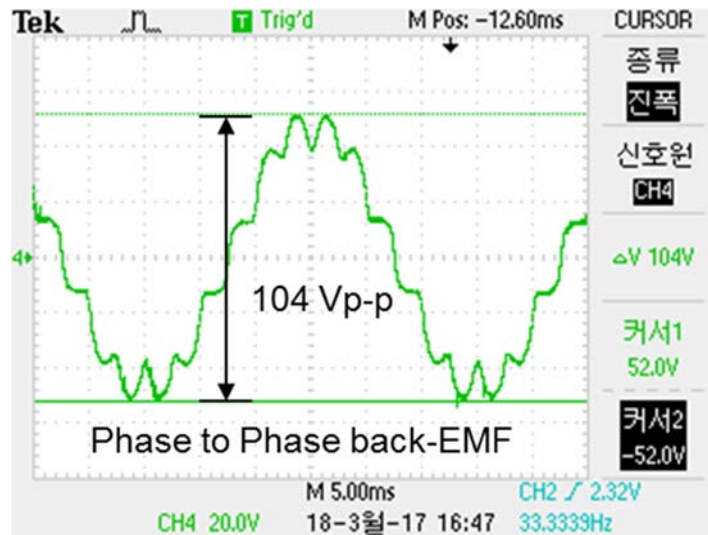


Fig. 4.2 Experimental setup for sensorless drive



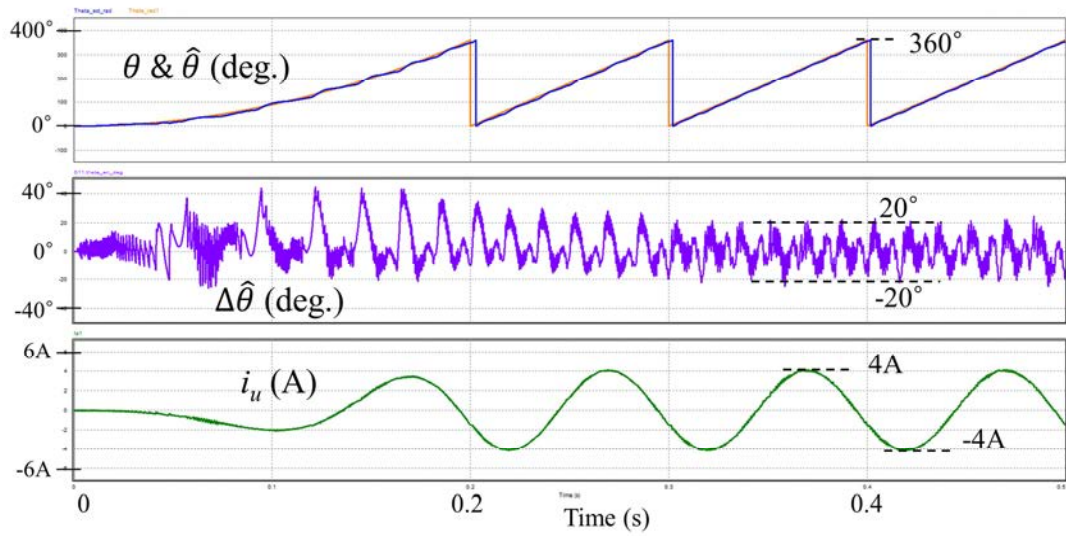
(a) Back-EMF in PSIM simulation at 1000 min^{-1}



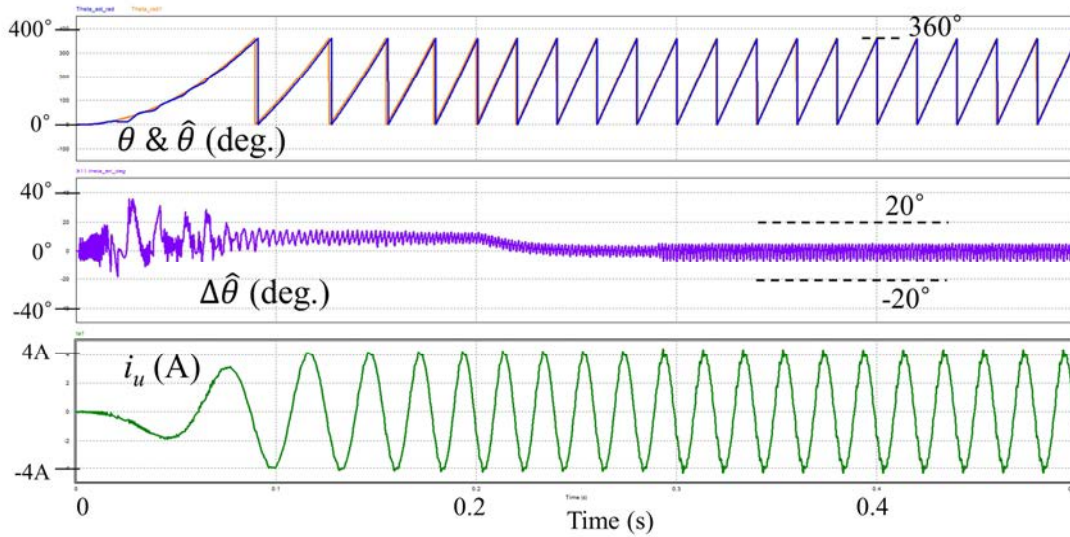
(b) Back-EMF in experiment at 1000 min^{-1}

Fig. 4.3 Back-EMF waveforms at 1000 min^{-1}

Fig. 4.3 shows the back-EMF waveforms of IPMSM at 1000 min^{-1} . The comparison results about simulation and experiment are almost the same because the RT model of JMAG is applied to PSIM simulation for high accuracy.



(a) 300 min^{-1}



(b) 1500 min^{-1}

Fig. 4.4 Steady state waveforms under 1.8 Nm

From Fig. 4.4, the steady state performance show stable waveforms when IPMSM is running with load of 1.8 Nm and speed from 300 min^{-1} to 1500 min^{-1} is given. It is clear that when the IPMSM is running in low-speed region, the maximum value of estimated position error isn't exceed 20 degree in steady state.

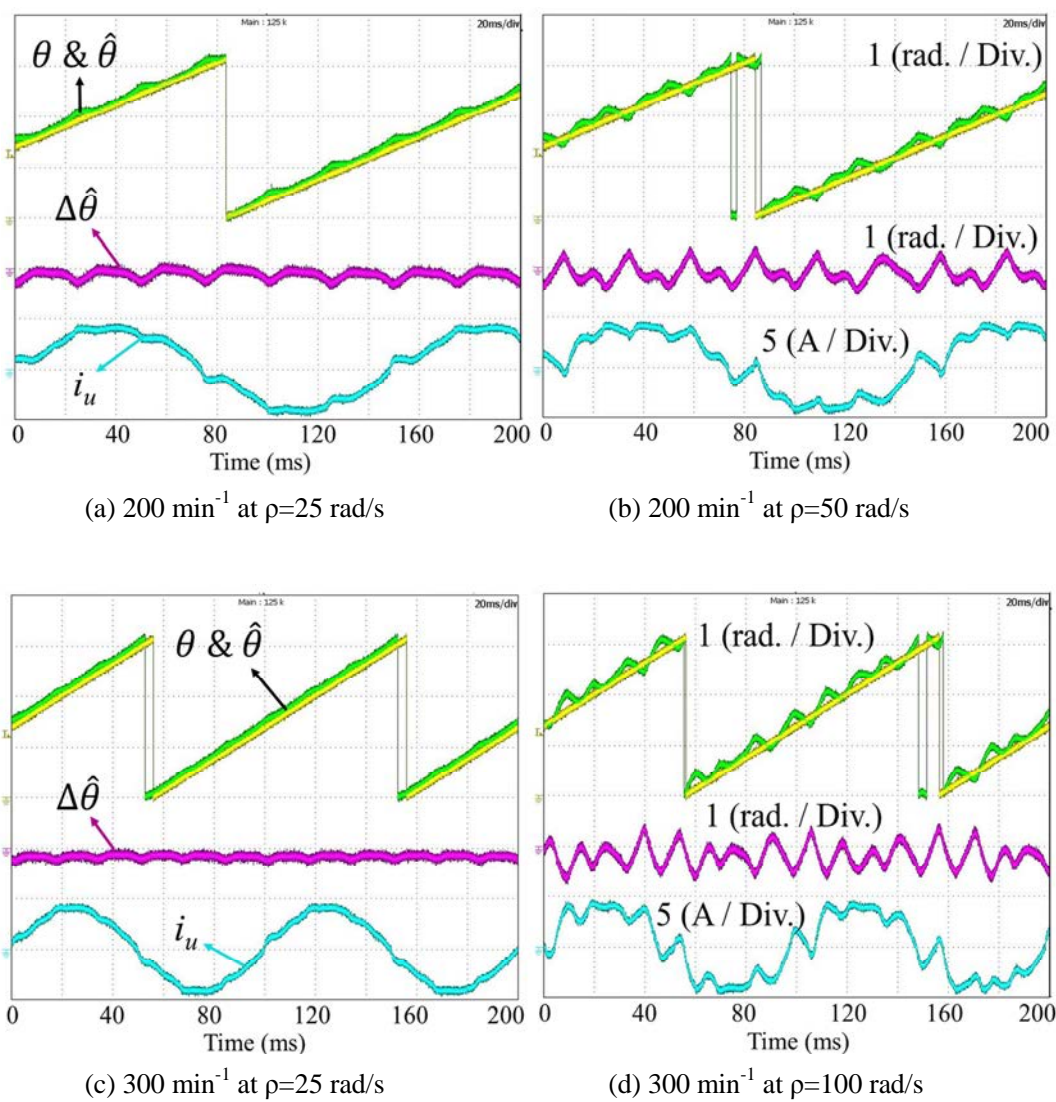


Fig. 4.5 Low speed waveforms under 1.8 Nm

Fig. 4.5 shows the low speed waveforms in the steady state. The bandwidth $\rho = 25$ rad/s is defined as the stable gain of sensorless control at 200 min⁻¹ and 300 min⁻¹. When the bandwidths are set to 50 rad/s and 100 rad/s respectively, the estimation error of $\Delta\hat{\theta}$ and i_u is increased as the noise signal effect becomes larger.

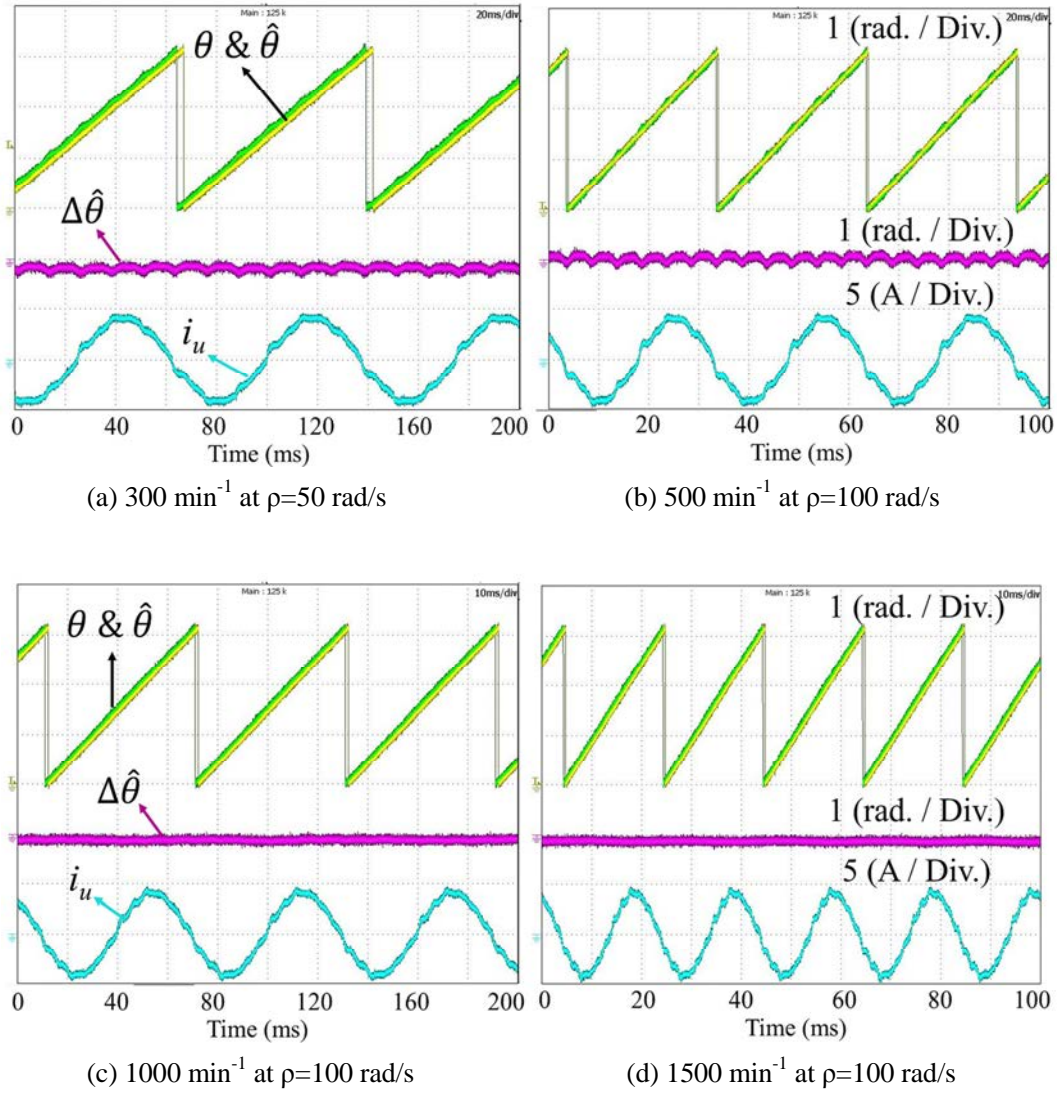


Fig. 4.6 Steady state waveforms at $\rho=100 \text{ rad/s}$ under 1.8 Nm

In Fig. 4.6, the stable waveforms in the steady state when IPMSM is controlled with 1.8 Nm load and speed from 300 min^{-1} to 1500 min^{-1} . The bandwidth ρ of PLL-type estimator is set to 50 rad/s and 100 rad/s respectively based on calculated results by stable gain selection process. The peak degrees of $\Delta\hat{\theta}$ waveforms gradually increased with a lower speed. However, the estimation performance of sensorless control is stable and the maximum error of estimated rotor position is limited within 1 radian.

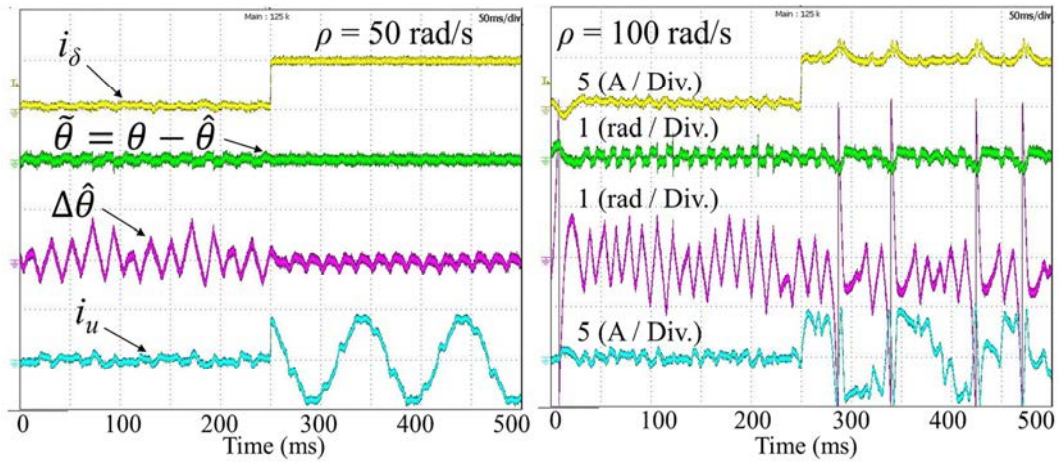


Fig. 4.7 Transient response on ρ value at 300 min^{-1}

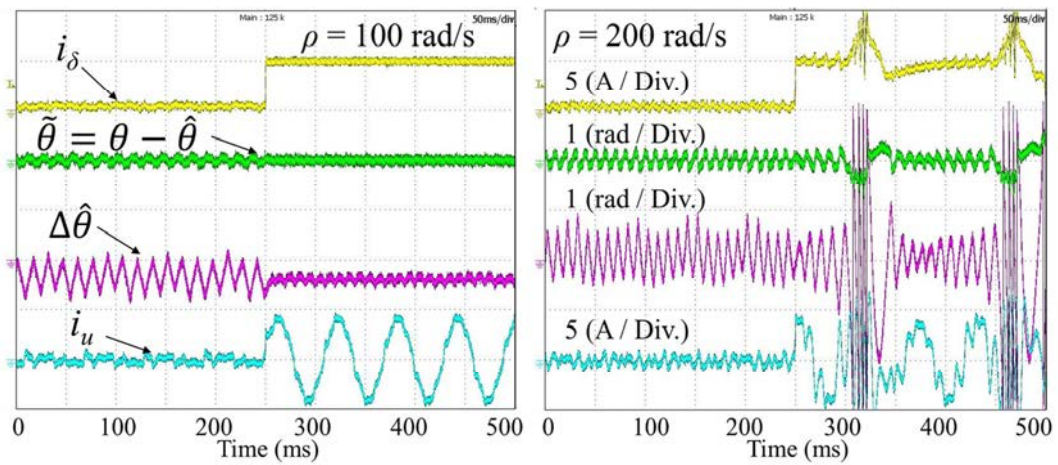


Fig. 4.8 Transient response on ρ value at 500 min^{-1}

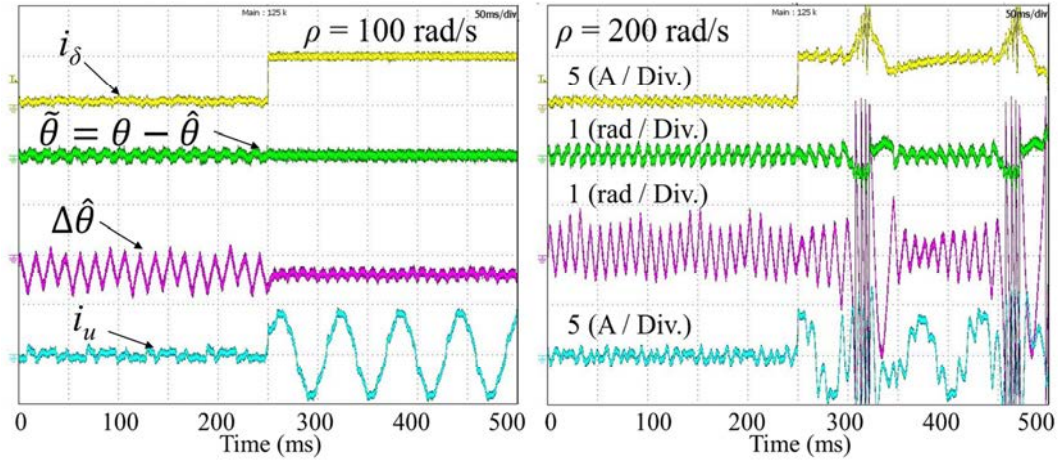


Fig. 4.9 Transient response on ρ value at 1500 min^{-1}

The transient response at 300 min^{-1} is shown in Fig. 4.7 when a step in i_δ at $t = 0.25 \text{ s}$. The selected bandwidth of PLL-type estimator $\rho = 50 \text{ rad/s}$ shows stable performance when the torque is increased rapidly from 0.1 Nm to 1.8 Nm . In contrast, a higher bandwidth $\rho = 100 \text{ rad/s}$ has unstable performance. Similarly, the $\rho = 100 \text{ rad/s}$ in 500 min^{-1} and 1500 min^{-1} has stable performance in Fig. 4.8 and in Fig. 4.9. However, in a higher bandwidth 200 rad/s and 400 rad/s respectively, the transient response of sensorless control is unstable. Therefore, in this experiment results, the stable performance in torque variation is obtained by the calculated parameter settings.

In Table 4.1, the stable region on the variation of ρ is shown. The position sensorless control is stable between 500 min^{-1} and 1500 min^{-1} when the ρ is set to 100 rad/s . And, Fig. 4.10 shows the stable map of sensorless control. A high ρ value makes a high overshoot of estimated rotor angle at low speed.

ρ [rad/s]	Speed [min^{-1}]													
	200	300	400	500	600	700	800	900	1000	1100	1200	1300	1400	1500
25	S	S	S	S	S	S	S	S	S	S	S	S	S	S
50	U	S	S	S	S	S	S	S	S	S	S	S	S	S
100	U	U	U	S	S	S	S	S	S	S	S	S	S	S
150	U	U	U	U	U	S	S	S	S	S	S	S	S	S
200	U	U	U	U	U	U	U	S	S	S	S	S	S	S
220	U	U	U	U	U	U	U	U	S	S	S	S	S	S
240	U	U	U	U	U	U	U	U	U	U	S	S	S	S
260	U	U	U	U	U	U	U	U	U	U	U	S	S	S
280	U	U	U	U	U	U	U	U	U	U	U	U	U	S

S : Stable U : Unstable

Table. 4.1 Stable region on torque step response from 0.1 to 1.8 Nm (200 to 1500 min^{-1})

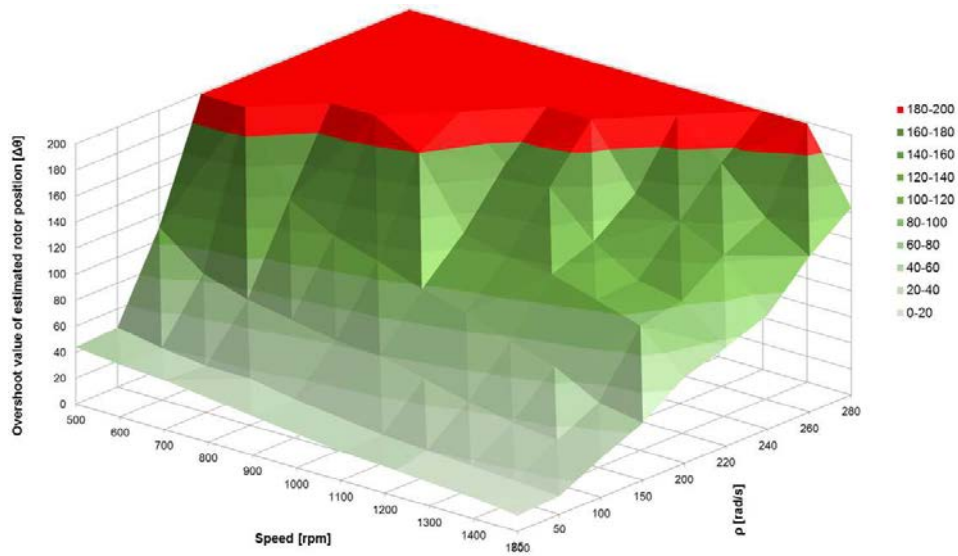


Fig. 4.10 Stable map of sensorless control on ρ value from 500 to 1500 min^{-1}

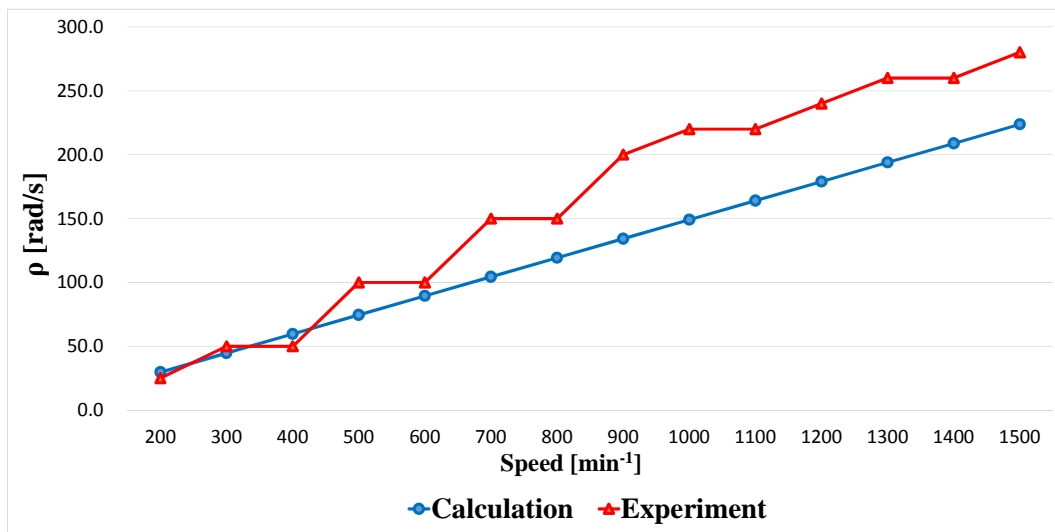


Fig. 4.11 Comparison results on the minimum ρ vaule from 200 to 1500 min^{-1}

Fig. 4.11 shows the comparison results on the minimum value of PLL-type estimator bandwidth ρ between the calculation results from (3.26) and experimental results under step torque response. As can be seen, the minimum ρ values in experimental results are chosen relatively high than the calculated minimum ρ values from 200 min^{-1} to 1500 min^{-1} .

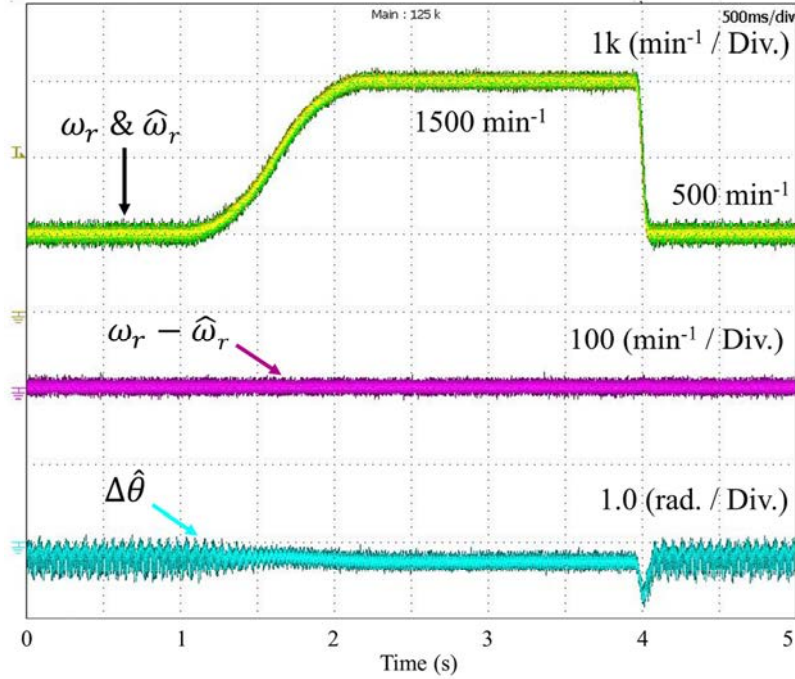


Fig. 4.12 Speed rampwise response at 1.8 Nm

In Fig. 4.12, the speed rampwise response from 500 min⁻¹ to 1500 min⁻¹ is stable when the PLL-type estimator is selected as $\rho = 100$ rad/s. The stable speed response can be obtained when the IPMSM is controlled by position sensorless drive during an acceleration time of 1s and deceleration time of 0.1s. Although the waveform of estimated position error $\Delta\hat{\theta}$ does have overshoot during rapid deceleration, the peak value of overshoot is confined within 1 radian.

4.2 Improvement of speed response using the proposed speed and position estimator

4.2.1 Compensation design of estimated position error

The estimated position error is defined as (3.7) on the assumption that the speed error is sufficiently small. But, if the estimated speed error is not small, the γ - δ axis currents can be expressed as d-q axis currents and $\Delta\hat{\theta}$ from Fig. 3.2.

$$i_{\delta} = i_d \sin \Delta\hat{\theta} + i_q \cos \Delta\hat{\theta} = \sqrt{i_d^2 + i_q^2} \cdot \cos \left(\Delta\hat{\theta} - \tan^{-1} \frac{i_d}{i_q} \right) \quad (4.1)$$

$$i_\gamma = -\left(i_q \sin \Delta\hat{\theta} - i_d \cos \Delta\hat{\theta}\right) = -\sqrt{i_d^2 + i_q^2} \cdot \sin\left(\Delta\hat{\theta} - \tan^{-1} \frac{i_d}{i_q}\right) \quad (4.2)$$

(where $i_d < 0, i_q \geq 0$)

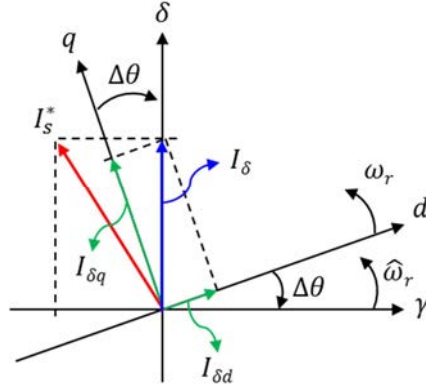


Fig. 4.13 -q components of I_δ vector

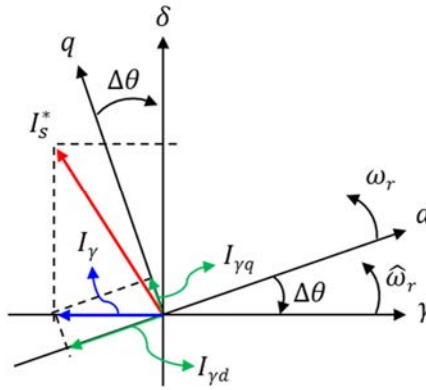


Fig. 4.14 -q components of I_γ vector

$$\begin{aligned} e_\gamma &= E_{ex} \cdot (-\sin \Delta\theta) + \Delta\omega_r L_d (-i_\delta) = -E_{ex} \sin \Delta\theta - \Delta\omega_r L_d \cdot \sqrt{i_d^2 + i_q^2} \cdot \cos\left(\Delta\theta - \tan^{-1} \frac{i_d}{i_q}\right) \\ &= -E_{ex} \sin \Delta\theta - \Delta\omega_r L_d \cdot \sqrt{i_d^2 + i_q^2} \cdot \left[\cos \Delta\theta \cdot \frac{1}{\sqrt{1 + (i_d / i_q)^2}} + \sin \Delta\theta \cdot \frac{(i_d / i_q)}{\sqrt{1 + (i_d / i_q)^2}} \right] \quad (4.3) \\ &= -\left((E_{ex} + \Delta\omega_r L_d i_d) \sin \Delta\theta + \Delta\omega_r L_d i_q \cos \Delta\theta\right) \end{aligned}$$

If $E_{ex} + \Delta\omega_r L_d i_d \geq 0$

$$e_\gamma = -\sqrt{(E_{ex} + \Delta\omega_r L_d i_d)^2 + (\Delta\omega_r L_d i_q)^2} \cdot \sin\left(\Delta\theta + \tan^{-1}\left(\frac{\Delta\omega_r L_d i_q}{E_{ex} + \Delta\omega_r L_d i_d}\right)\right) \quad (4.4)$$

Also, e_δ can be derived by similar equation.

$$\begin{aligned} e_\delta &= E_{ex} \cos \Delta\theta + \Delta\omega_r L_d i_\gamma = E_{ex} \cos \Delta\theta - \Delta\omega_r L_d \cdot \sqrt{i_d^2 + i_q^2} \cdot \sin\left(\Delta\theta - \tan^{-1}\frac{i_d}{i_q}\right) \\ &= E_{ex} \cos \Delta\theta - \Delta\omega_r L_d \cdot \sqrt{i_d^2 + i_q^2} \cdot \left(\sin \Delta\theta \cdot \frac{1}{\sqrt{1+(i_d/i_q)^2}} - \cos \Delta\theta \cdot \frac{(i_d/i_q)}{\sqrt{1+(i_d/i_q)^2}} \right) \\ &= (E_{ex} + \Delta\omega_r L_d i_d) \cos \Delta\theta - \Delta\omega_r L_d i_q \sin \Delta\theta \end{aligned} \quad (4.5)$$

If $\Delta\omega_r L_d i_q > 0$

$$e_\delta = \sqrt{(E_{ex} + \Delta\omega_r L_d i_d)^2 + (\Delta\omega_r L_d i_q)^2} \cdot \cos\left(\Delta\theta - \tan^{-1}\left(\frac{-\Delta\omega_r L_d i_q}{E_{ex} + \Delta\omega_r L_d i_d}\right)\right) \quad (4.6)$$

Comparing (4.1) and (4.2) with (3.5), the back-EMF in the γ - δ reference frame can be deduced as (4.7).

$$\frac{e_\gamma}{e_\delta} = \frac{E_{ex} \cdot (-\sin \hat{\Delta}\theta) + \Delta\omega_r L_d (-i_\delta)}{E_{ex} \cdot \cos \hat{\Delta}\theta + \Delta\omega_r L_d i_\gamma} = -\tan\left(\Delta\hat{\theta} + \tan^{-1}\left(\frac{\Delta\omega_r L_d i_q}{E_{ex} + \Delta\omega_r L_d i_d}\right)\right) \quad (4.7)$$

where $\Delta\omega_r = \omega_r - \hat{\omega}_r$ and if $-\frac{\pi}{2} < \Delta\theta + \tan^{-1}\left(\frac{\Delta\omega_r L_d i_q}{E_{ex} + \Delta\omega_r L_d i_d}\right) < \frac{\pi}{2}$

$$\tan^{-1}\left(-\frac{e_\gamma}{e_\delta}\right) = \Delta\hat{\theta} + \tan^{-1}\left(\frac{\Delta\omega_r L_d i_q}{E_{ex} + \Delta\omega_r L_d i_d}\right) = \Delta\hat{\theta} + \theta_{SC} \quad (4.8)$$

Where $-\frac{\pi}{2} < \Delta\hat{\theta} + \theta_{SC} < \frac{\pi}{2}$

Therefore, the estimated position error in transient state is expressed by (4.8).

θ_{SC} is compensation angle for alignment in transient-state. And $\Delta\omega_r$ can be estimated by (4.13) derived from the next section 4.2.2.

4.2.2 Compensation design of estimated speed error

As described in [20] [21] [31] [35], an input error signal of PLL-type estimator can be defined as (4.9) and (4.10).

$$\begin{aligned}\sigma_d &= (V_d - \hat{V}_d) = V_d^* - \hat{R} \cdot i_d^* + \hat{\omega}_r \cdot \hat{L}_q \cdot i_q^* \\ \sigma_q &= (V_q - \hat{V}_q) = V_q^* - \hat{R} \cdot i_q^* - \hat{\omega}_r \cdot \hat{L}_d \cdot i_d^*\end{aligned}\quad (4.9)$$

$$\begin{aligned}\sigma_d &= -\psi \cdot \omega_r \cdot \sin \Delta\hat{\theta} + \omega_r \cdot i_q \cdot \Delta L \sin^2 \Delta\hat{\theta} \\ \sigma_q &= \psi \cdot \omega_r \cdot \cos \Delta\hat{\theta} - \omega_r \cdot i_q \cdot \Delta L \sin \Delta\theta \cdot \cos \Delta\hat{\theta}\end{aligned}\quad (4.10)$$

where $\Delta L = L_q - L_d$ and σ_d, σ_q are the error signals of d-q axis. And the parameter errors are ignored. From (4.10), the absolute value of error signal and the estimated $\Delta\omega_r$ can be obtained as follow

$$|\sigma| = \sqrt{(\sigma_d^2 + \sigma_q^2)} = |\omega_r| \cdot (\psi - \Delta L \cdot i_q \cdot \sin \Delta\hat{\theta}) \quad (4.11)$$

$$|\omega_r| = \frac{|\sigma|}{\psi - \Delta L \cdot i_q \cdot \sin \Delta\hat{\theta}} \quad (4.12)$$

$$\Delta\hat{\omega}_r = \frac{|\sigma|}{\psi - \Delta L \cdot i_q \cdot \sin \Delta\hat{\theta}} \cdot \text{sign}(\hat{\omega}_r) - \hat{\omega}_r \quad (4.13)$$

$$\Delta\hat{\omega}_c = m_{SC} \cdot \Delta\hat{\omega}_r \quad (4.14)$$

The absolute value $|\sigma|$ of error signal can be obtained in (4.9). Therefore, the $\Delta\hat{\omega}_c$ can be utilized to compensate the speed difference error in transient state. And m_{sc} is manual tuning value on speed variation. The block diagram for angle compensation and estimated speed error compensation can be drawn as shown in Fig. 4.15. The compensation term $\Delta\hat{\omega}_c$ using (4.14) and θ_{SC} using (4.8) have some value in rapidly acceleration and deceleration.

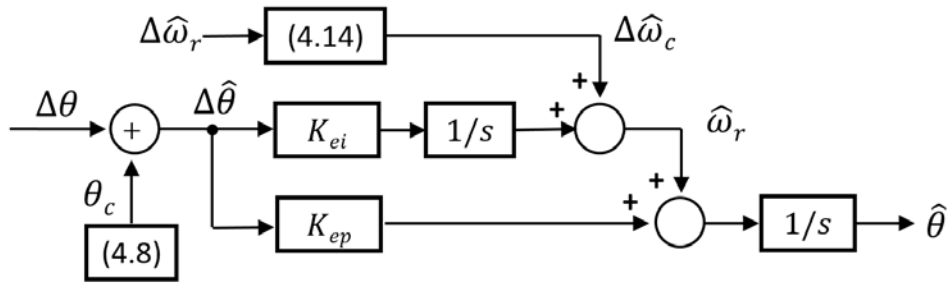


Fig. 4.15 Proposed PLL-type estimator using estimated angle and speed error compensation

4.2.3 Simulation and experimental results

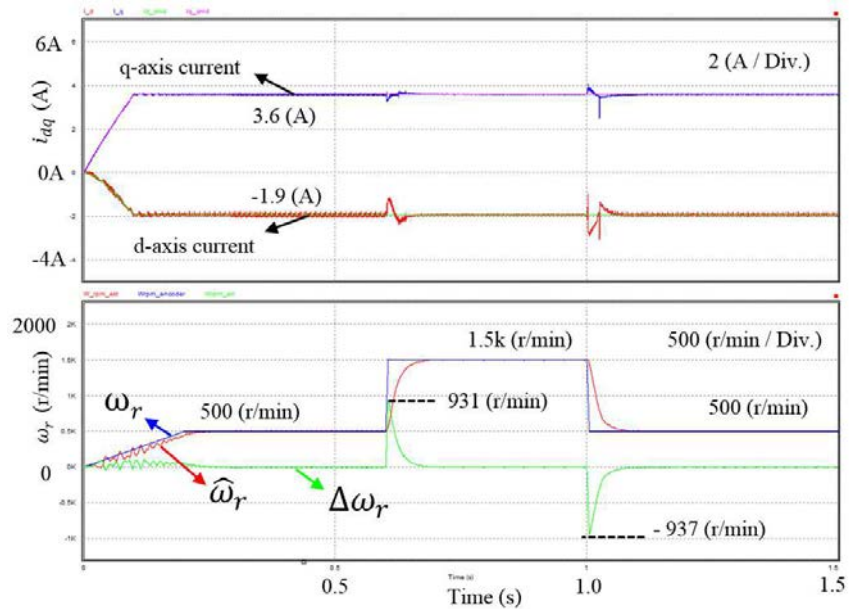


Fig. 4.16 Transient waveforms of d-q axis current and speed in conventional PLL-type estimator

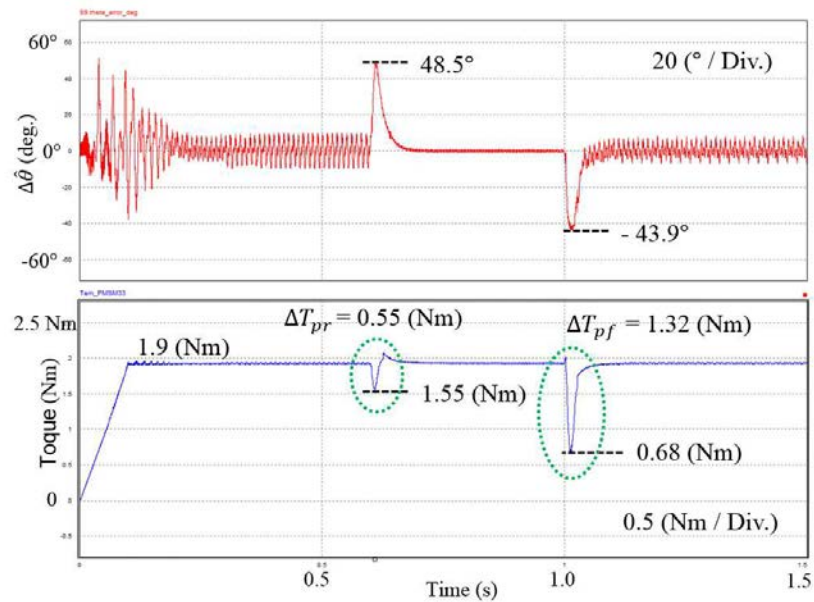


Fig. 4.17 Transient waveforms of estimated position error and torque in conventional PLL-type estimator

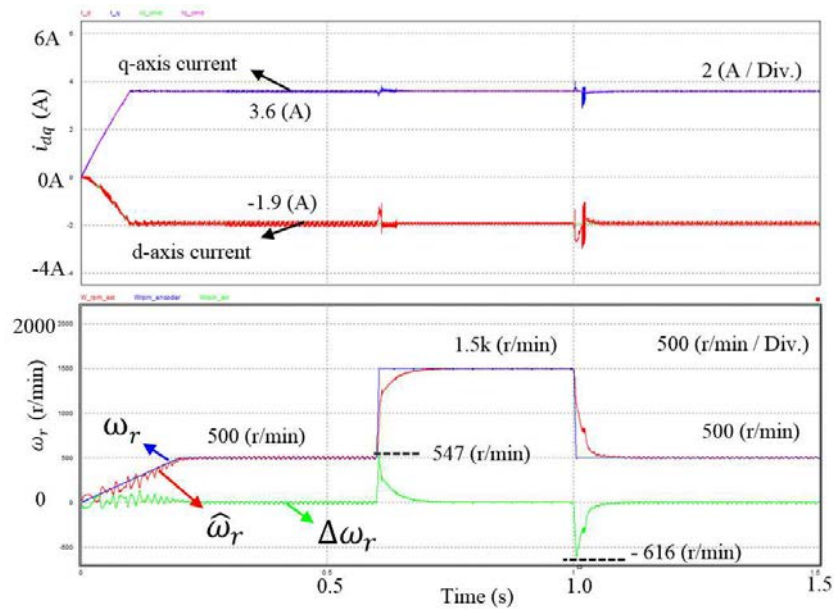


Fig. 4.18 Transient waveforms of d-q axis current and speed with proposed PLL-type estimator

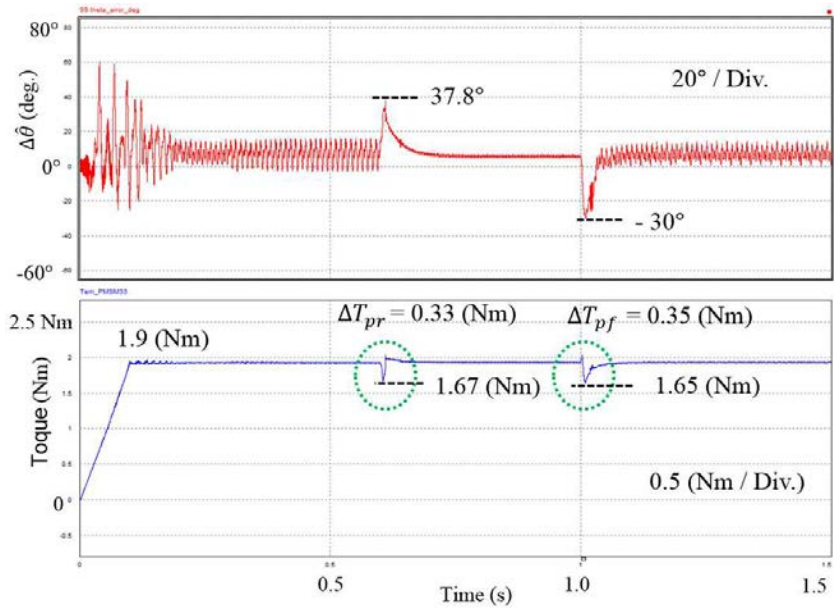


Fig. 4.19 Transient waveforms of estimated position error and torque with proposed PLL-type estimator

Fig. 4.16 shows the d-q axis current and speed response in the conventional PLL-type estimator when the rampwise change of speed occurs from 500 r/min to 1500 r/min during the rising and falling time of 5ms. The overshoot of speed difference term $\Delta\omega_r$ is occurred about 930 r/min when the speed is rapidly increased or decreased. At the same time, the overshoot of torque and estimated position error are occurred in Fig. 4.17. The overshoot values of $\Delta\hat{\theta}$ are 48.5 deg. and -43.9 deg. respectively. And the peak to peak values in acceleration ΔT_{pr} and in deceleration ΔT_{pf} are 0.55 Nm and 1.32 Nm respectively.

Fig. 4.18 shows the transient waveforms about d-q axis current and speed in the proposed PLL-type estimator. The overshoot values of $\Delta\omega_r$ in acceleration is about 547 r/min and -616 r/min in deceleration. Also, Fig. 4.19 represents the low overshoot of estimated position error and torque. The overshoot values of $\Delta\hat{\theta}$ are 37.8 deg. and -30 deg., and ΔT_{pr} is 0.33 Nm and ΔT_{pf} are 0.35 Nm respectively. Therefore, the PLL-type estimator with proposed compensation method shows lower overshoot values than the conventional PLL-type estimator. Therefore, the good dynamics can be obtained by the compensated PLL-type estimator.

Fig. 4.20 shows the simulation results on the overshoot comparison of $\Delta\omega_r$ in acceleration and deceleration time. The overshoot values of $\Delta\omega_r$ are reduced with compensated method compared to the no compensation method.

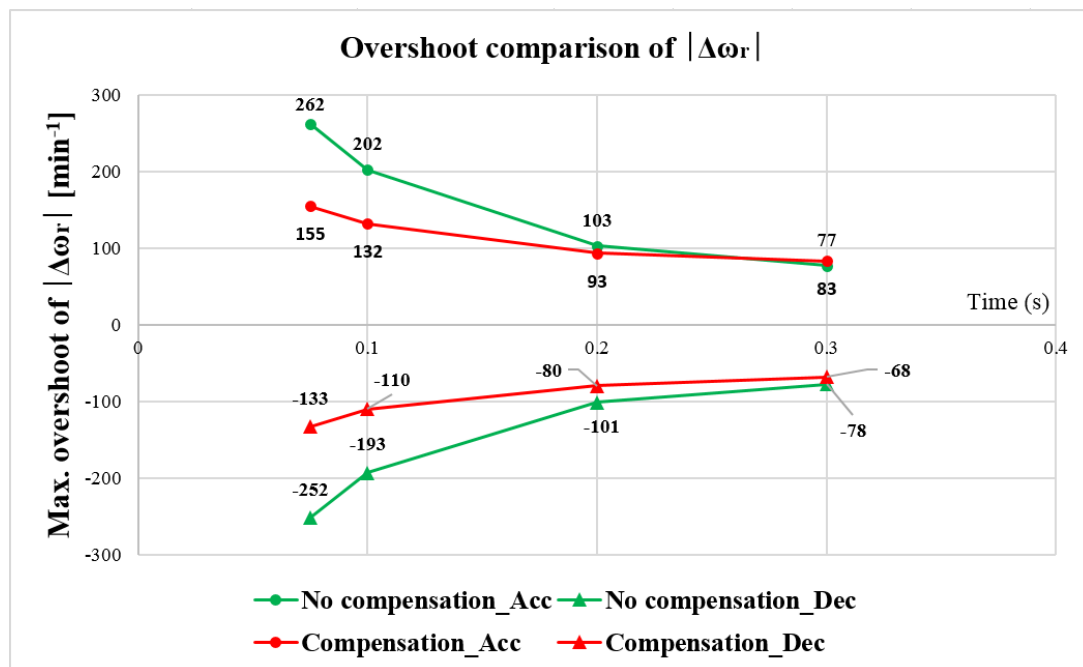


Fig. 4.20 Overshoot comparison of estimated speed error in acceleration and deceleration time

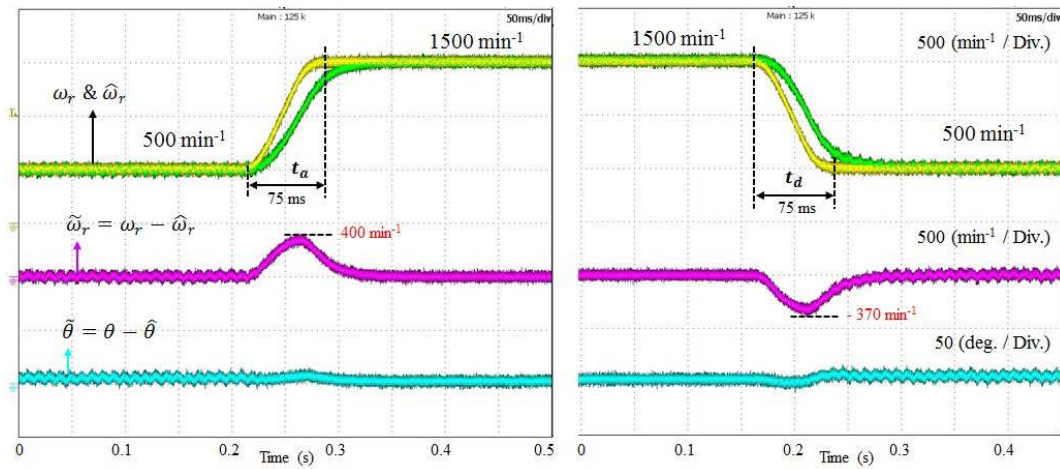


Fig. 4.21 Transient waveforms in conventional PLL-type estimator

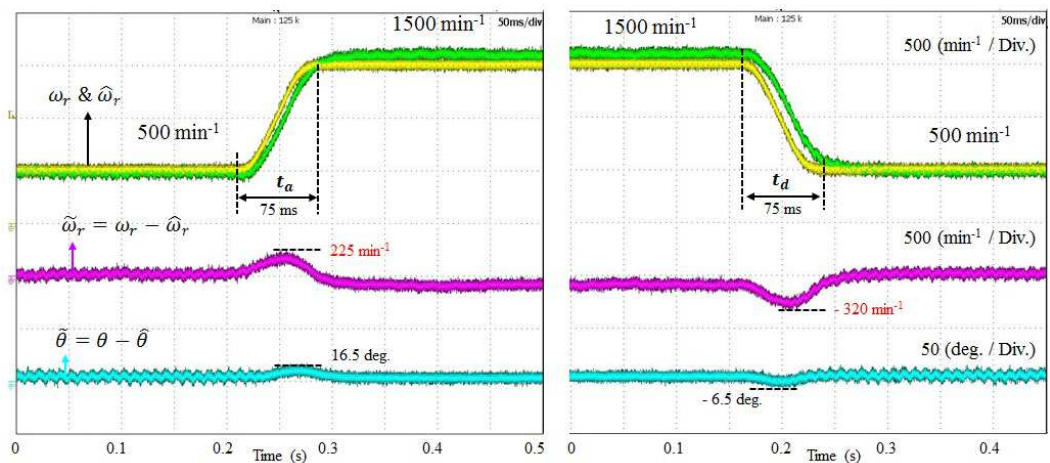


Fig. 4.22 Transient waveforms with proposed PLL-type estimator

Fig. 4.21 shows the speed response in the conventional PLL-type estimator when the rampwise change of speed occurs from 500 min^{-1} to 1500 min^{-1} during the rising and falling time of 75 ms. The overshoot of speed difference term $\tilde{\omega}_r$ is occurred about 400 min^{-1} and -370 min^{-1} at rising and falling time respectively when the speed is rapidly increased or decreased with $m_{sc} = 1$. Fig. 4.22 shows the transient waveforms of speed and position error difference in the proposed PLL-type estimator. The overshoot values of $\tilde{\omega}_r$ in acceleration are about 225 r/min and -320 r/min in deceleration. In this results, the PLL-type estimator with proposed compensation method shows lower overshoot values than the conventional PLL-type estimator. Therefore, the good dynamics can be obtained by the compensated PLL-type estimator.

4.3 Improvement of torque response using current feedback control

4.3.1 Design of current feedback control

In order to improve the transient stability, the overshoot value of estimated position error needs to decrease. If the reference torque is decreased, the q-axis current is decreased. And the q-axis inductance is increased instantaneously. The increased q-axis inductance causes the overshoot of estimated position error. The high estimated position error can increase the possibility of control angle slip. This angle slip can result in the instability of sensorless control system. Therefore, the overshoot of estimated position error should be decreased. The overshoot is occurred when the speed are changed in short time from (3.3), (3.5).

If it is assumed that the estimated speed error is not small, (3.5) can be expressed in (4.15) as mentioned in section 4.2.1 and (4.8).

$$\tan^{-1}\left(-\frac{e_\gamma}{e_\delta}\right) = \Delta\theta + \tan^{-1}\left(\frac{\Delta\omega_r L_d i_q}{E_{ex} + \Delta\omega_r L_d i_d}\right) = \Delta\theta + \theta_{FC} \quad (4.15)$$

Where $\Delta\omega_r$ is $\hat{\omega}_r - \omega_r$ and θ_{FC} is compensation angle for alignment in transient state. $\Delta\omega_r$ and E_{ex} are dominant terms related q-axis current and generally the estimation error of q-axis current is fed to the PI controller to get the speed estimation value. Therefore, the θ_{FC} can be compensated by current feedback control as (4.16) [70].

$$\frac{d\theta_{FC}}{dt} = m_{ac} \times \left(k_p \cdot (i_q^* - i_\delta) + k_i \int (i_q^* - i_\delta) \cdot dt \right) \quad (4.16)$$

Where k_p and k_i are PI gain for current feedback controller. And the constant m_{ac} is a manual tuning value to make zero level between estimated position error and position error in transient state. The block diagram for angle compensation can be drawn as shown in Fig. 4.23 [45].

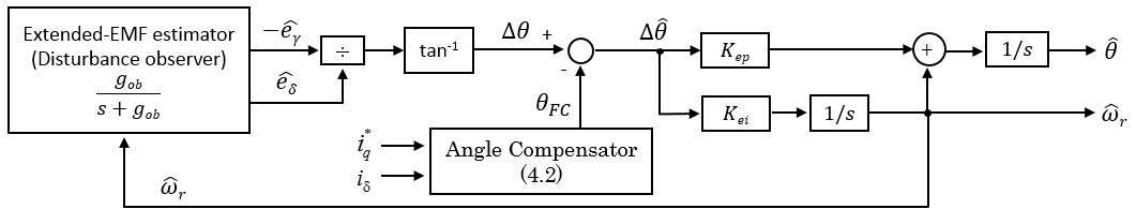


Fig. 4.23 Block diagram of proposed current feedback control

4.3.2 Stability analysis of current feedback control

For stability analysis, the error dynamics of estimator by (3.16), (4.16) and Fig. 4.23 are given as

$$\begin{aligned}\Delta\dot{\hat{\omega}}_r &= \rho^2 \cdot (\Delta\theta + \theta_{FC}) \\ \dot{\hat{\theta}} &= \hat{\omega}_r + 2\rho \cdot (\Delta\theta + \theta_{FC})\end{aligned}\quad (4.17)$$

The error dynamics can be expressed as (4.18) in nominal and high speeds with $\Delta\omega'_r \approx \Delta\omega_r$

$$\begin{aligned}\Delta\dot{\hat{\omega}}_r &= \dot{\omega}_r - \hat{\dot{\omega}}_r = -\dot{\hat{\omega}}_r = -\rho^2 \cdot \Delta\theta - \rho^2 \cdot \theta_{FC} \\ \Delta\dot{\hat{\theta}} &= \dot{\theta} - \hat{\dot{\theta}} = \omega_r - (\hat{\omega}_r + 2\rho \cdot (\Delta\theta + \theta_{FC})) = \Delta\omega_r - 2\rho \cdot \Delta\theta - 2\rho \cdot \theta_{FC}\end{aligned}\quad (4.18)$$

The stability of nonlinear system can be defined by the coefficients of characteristic polynomial.

$$\det(sI - (A - BK)) = \det\left(\begin{bmatrix} s & 0 \\ 0 & s \end{bmatrix} - \left(\begin{bmatrix} 0 & -\rho^2 \\ 1 & -2\rho \end{bmatrix} - \begin{bmatrix} -\rho^2 \\ -2\rho \end{bmatrix} \begin{bmatrix} k_1 & k_2 \end{bmatrix}\right)\right)\quad (4.19)$$

$$\det(sI - (A - BK)) = s^2 - (k_1\rho + 2(k_2 - 1) \cdot \rho) \cdot s + (1 + k_2) \cdot \rho^2\quad (4.20)$$

In accordance with stable gain selection process of section 3.7, PLL-type estimator bandwidth is set to 100 rad/s. Therefore, characteristic polynomial equation is given by

$$\begin{aligned}\det(sI - (A - BK)) &= s^2 - (100k_1 + 200(k_2 - 1)) \cdot s + (1 + k_2) \cdot 10000 \\ &= s^2 + m_1 \cdot s + m_2\end{aligned}\quad (4.21)$$

Using the Routh-Hurwitz stability criterion, if the coefficients of the characteristic polynomial are positive such as $m_1 > 0$ and $m_2 > 0$, the nonlinear system is stable.

Therefore, the stability condition can be defined as

$$\therefore -K_1 > 2(K_2 - 1), \quad K_2 > -1\quad (4.22)$$

If K_2 is set to 0.15, K_1 should set less value than 1.7.

Also, the closed loop poles, damping ratio and undamped natural frequency are defined as below

$$s_{1,2} = \frac{-m_1 \pm \sqrt{m_1^2 - 4m_2}}{2}\quad (4.23)$$

$$\zeta = \frac{m_1}{2\sqrt{m_2}}, \quad \omega_n = \sqrt{m_2}\quad (4.24)$$

4.3.3 Simulation and experimental results

The configuration of the sensorless drive system is shown in Fig. 4.23. From stable gain selection process, the sensorless control parameters can be set as below

$$t_r = 0.7 \text{ ms}, \quad \alpha_c = 3140 \text{ rad/s}, \quad |\Delta\theta|_{max} = 10 \text{ degree}, \quad |\dot{\omega}_r|_{max} = 2073 \text{ rad/s}^2, \quad g_{ob} = 1000 \text{ rad/s},$$

$$m_{ob} = 0.12, \quad m_{ac} = 0.15, \quad \rho = 100 \text{ rad/s}, \quad \omega_{r,min} = 476 \text{ min}^{-1} \doteq 500 \text{ min}^{-1}$$

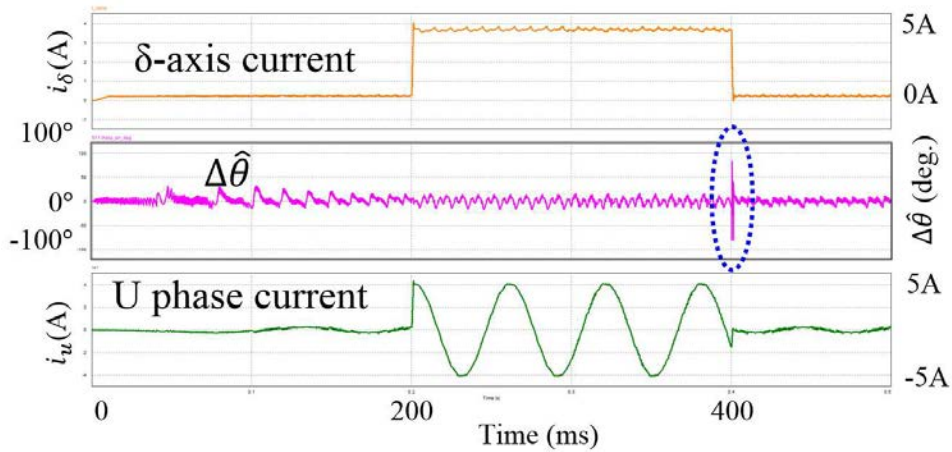
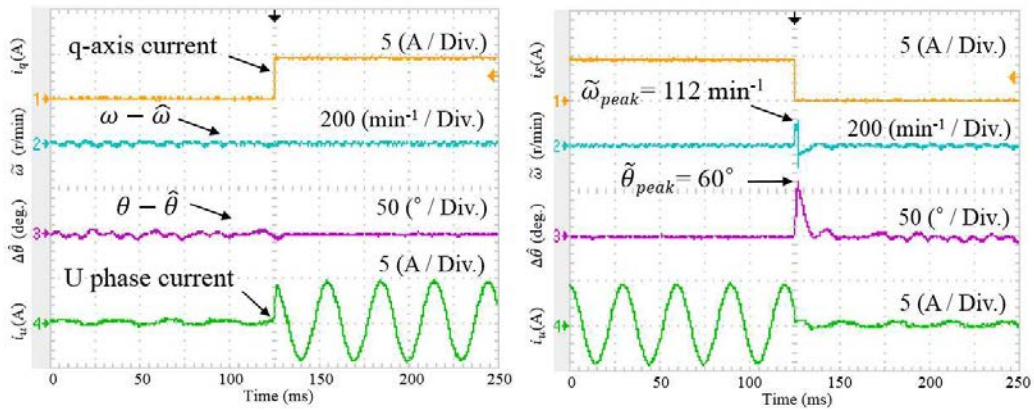


Fig. 4.24 Overshoot of estimated position error on rapidly torque variation in sensorless control

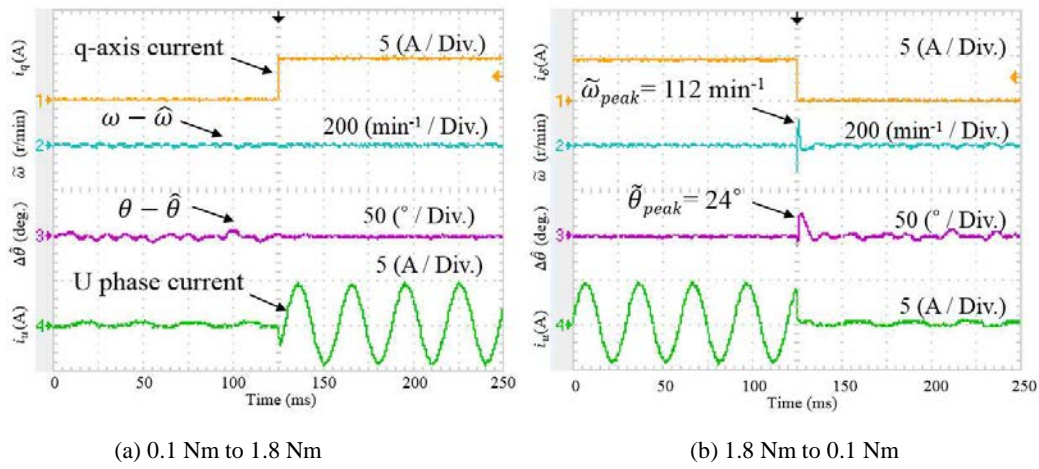
Fig. 4.24 shows the simulation result on the overshoot of estimated position error when the reference torque is rapidly decreased at 500 min^{-1} . This overshoot can be decreased by proposed angle compensation method using current feedback control to improve a stable sensorless control.



(a) 0.1 Nm to 1.8 Nm

(b) 1.8 Nm to 0.1 Nm

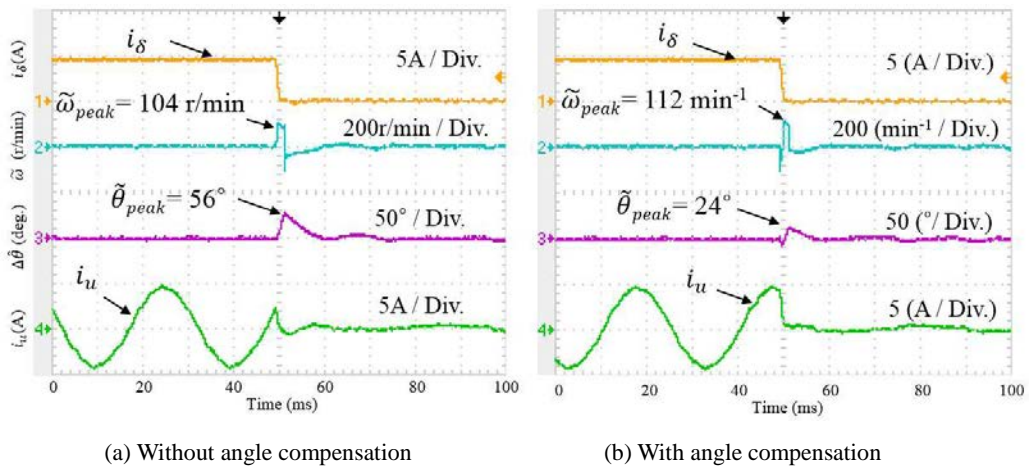
Fig. 4.25 Overshoot response without angle compensation at 1000 min^{-1}



(a) 0.1 Nm to 1.8 Nm (b) 1.8 Nm to 0.1 Nm

Fig. 4.26 Overshoot response with angle compensation at 1000 min^{-1}

Fig. 4.25 shows the overshoot waveforms without proposed current feedback control at 1000 min^{-1} . The overshoot angle is 60 degree, whereas the overshoot angle of sensorless control with proposed method in Fig. 4.26 is 24 degree, which is lower than that of the uncompensation algorithm.



(a) Without angle compensation (b) With angle compensation

Fig. 4.27 Overshoot response comparison at 1000 min^{-1} (from 1.8 to 0.1 Nm)

Fig. 4.27 represents the comparison results of overshoot waveform with proposed current feedback control and without it when the m_{ac} value was selected to 0.15 in (4.16). In the proposed compensation method, the overshoot values of estimated position error show lower value than the overshoot value of uncompensated sensorless control.

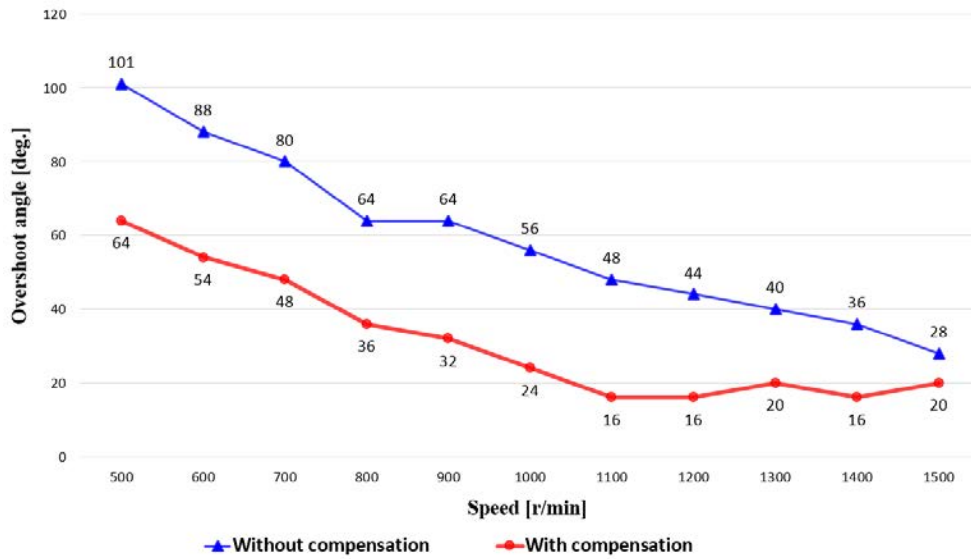


Fig. 4.28 Comparison results of overshoot value at $\rho=100$ rad/s in transient state

Fig. 4.28 shows the comparison results of overshoot value on different speed. The red line is overshoot value of estimated position error with compensation method. There is lower value than the overshoot value of conventional sensorless control. So, the good dynamics is obtained with the proposed feedback current control method.

4.4 Performance comparison on speed and position estimator

Various estimators for the speed and position estimation are shown in Fig. 4.29. The performance of estimators on position and speed estimation and the maximum overshoot of estimated speed and position error is compared under step torque variation and rampwise speed variation by PSIM simulation such as Fig 4.30. The comparison results are shown in Table. 4.1. From this result, the maximum overshoot of estimator using proposed current feedback method is lower than other estimator methods although the overshoot of estimated speed error $\Delta\omega_{err}$ in rampwise speed variation is higher than other methods. However, this overshoot can be decreased by the proposed method for speed response improvement in the section 4.3. Therefore, the high performance of PLL-type estimator can be achieved with proposed control strategy.

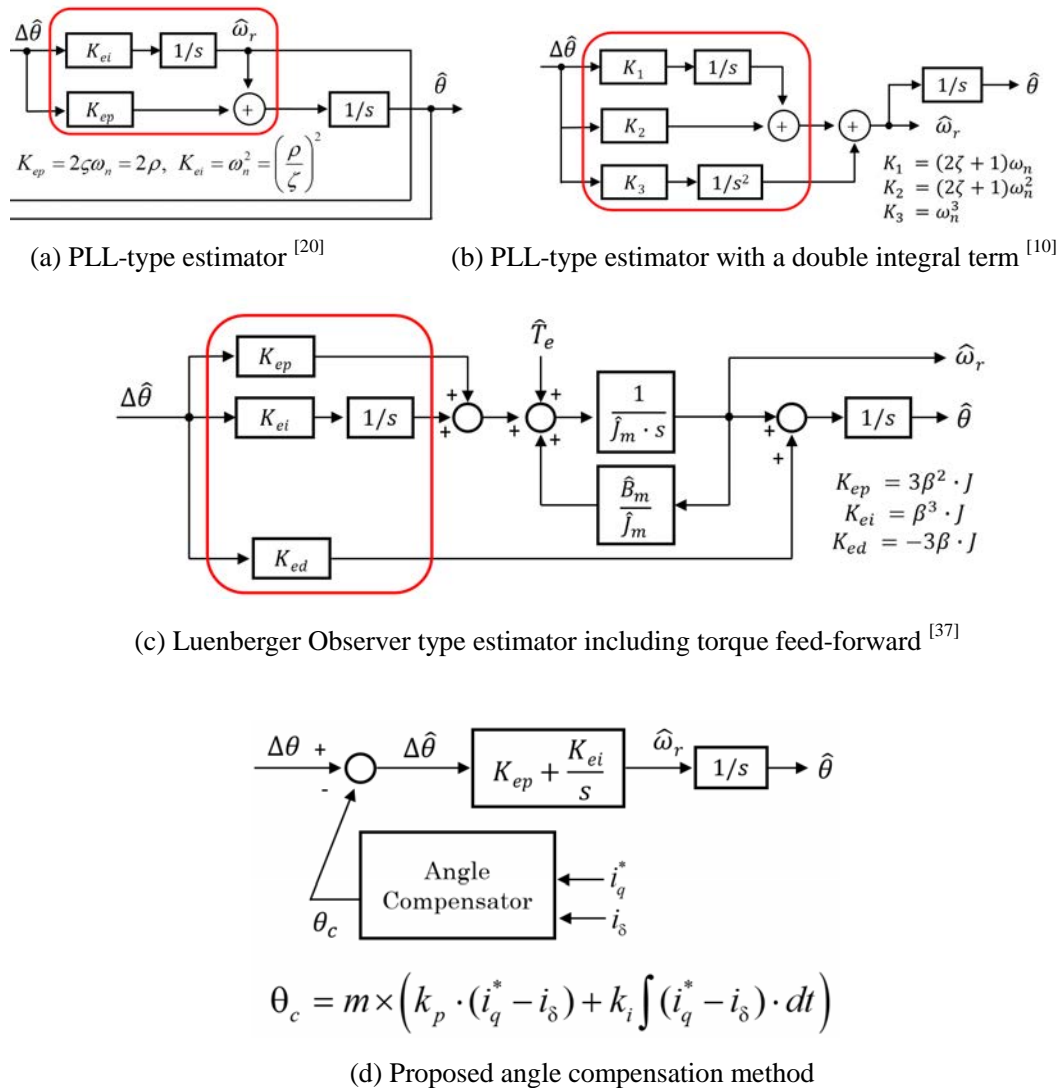


Fig. 4.29 Various position and speed estimators using back-EMF estimation method

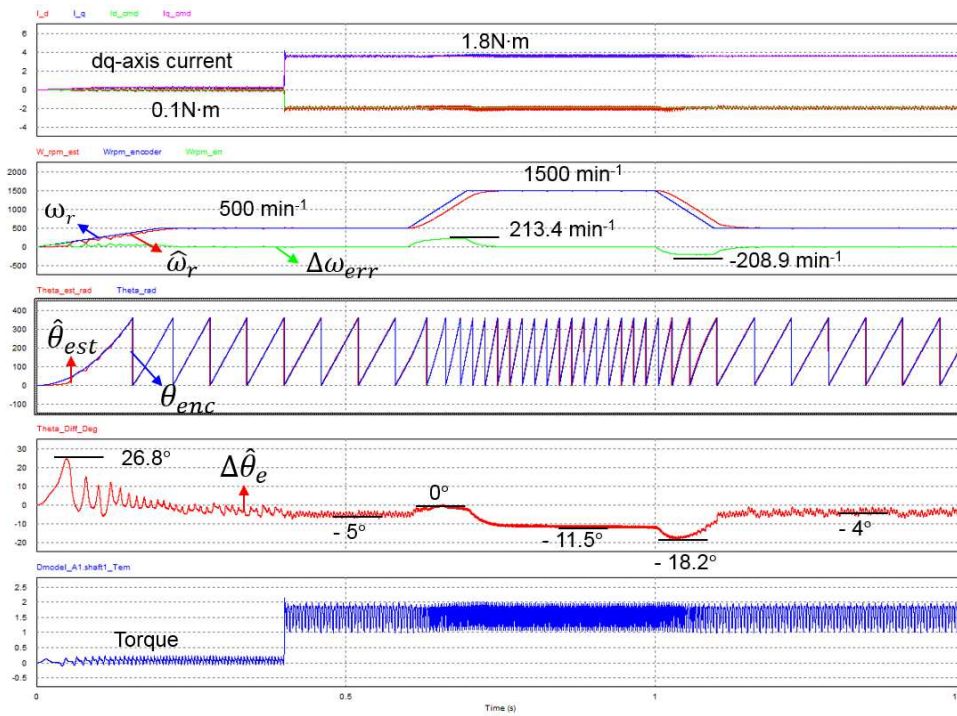


Fig. 4.30 Overshoot waveforms of PLL-type estimator

Table 4.2 Estimator comparison results on the torque and speed variation

Item	PLL-type (a)	Double Integral PLL (b)	LO-type estimator (c)	Proposed current feedback (d)
Step torque (Max. $\Delta\omega_{err}$ [min^{-1}])	26.8	81.4	144	22.5
Rampwise speed (Max. $\Delta\omega_{err}$ [min^{-1}])	213.4	130.6	73.5	209
Step torque in rising (Max. $\Delta\theta_{err}$ [degree])	-7.4	-10.2	-8.9	-6.5
Step torque in falling (Max. $\Delta\theta_{err}$ [degree])	3.6	5.8	4.3	3.3

4.5 Chapter summary

In this chapter, the bandwidth of PLL estimator for the rotor and speed estimation of IPMSM has been analyzed regarding stable range from test results. And, the overshoot peak values of estimated position error are limited a lower value than the results of uncompensated sensorless control from the proposed current feedback control and the estimator bandwidth selection considering stable bandwidth range.

The bandwidth of conventional PLL-type estimator for the rotor and speed estimation of IPMSM has been analyzed in speed variation. In steady state, the stable bandwidth of estimator can be selected by gain selection process. But, the high overshoot of estimated $\Delta\omega_r$ in fast acceleration represents under stable bandwidth. In order to increase the stability of sensorless control, the compensation method of PLL-type estimator is proposed. When using the proposed strategy in fast speed variation, the transient performance could be improved. The proposed method includes the angle compensation term and speed compensation term. So, the fast compensation is possible. The test results show that the overshoot peak values of estimated position and speed error and overshoot torque values in the compensated PLL-type estimator are limited to a lower value than the overshoot peak values of uncompensated PLL-type estimator.

Various estimators for the speed and position estimation are introduced and compared with proposed method by simulation on performance in speed and torque variation.

Chapter 5 Sensor fault detection and algorithm transition

5.1 Introduction

Recently, for the traction control of electric/hybrid vehicle, fault detection and fault tolerance of position sensor such as encoder and resolver are important not only for the reliability of the control system but also for the normal operation despite position sensor fault. The faulty position sensor should be detected quickly to avoid a serious damage of the control system^[27]. Then, a fast fault detection and isolation is required to eliminate the fault effects. A Fault Detection and Isolation (FDI) method and algorithm transition from sensed to sensorless control have been developed for PMSM drives^{[23]-[25]}. If the difference between the measured value and the estimated value is higher than a selected threshold value, the control algorithm should be changed from sensed to sensorless control. However, most of them focused on the faults in steady state of a control system and the threshold value for fault detection was defined in steady state. Also, the parameter variation such as stator resistance and q-axis inductance affects the estimated position error in low speed region^[48]. Therefore, this effect have to be considered when the threshold value is selected^{[52]-[56]}.

This chapter presents the fault detection and algorithm transition considering the maximum overshoot value of estimated speed and position difference error on designed gains of speed and position estimator in the healthy operation of current sensors. Also, the selection method of threshold value to detect the fault condition of speed and position sensor using CUSUM algorithm (Cumulative-SUM) is studied with the effect of motor parameter variation. The main advantage of CUSUM algorithm is robustness on parameter variation and uncertainty^{[25][26]}.

5.2 Encoder sensor fault detection

The faults of a rotor position sensor can be detected by the difference value between measured angle and estimated angle or measured speed and estimated speed. The fault detection process of encoder is shown in Fig. 5.1 and Fig. 5.2. If the fault occurs, the control angle θ_c and ω_c have the same value continuously during holding time t_h because the difference value $\theta_{err} = \theta_{enc} - \theta_{est}$ and $\omega_{err} = \omega_{enc} - \omega_{est}$ do not reach the threshold value θ_{Th} and ω_{Th} . Then, the algorithm transition from sensed to sensorless control can be achieved when θ_{err} and ω_{err} exceed the threshold value.

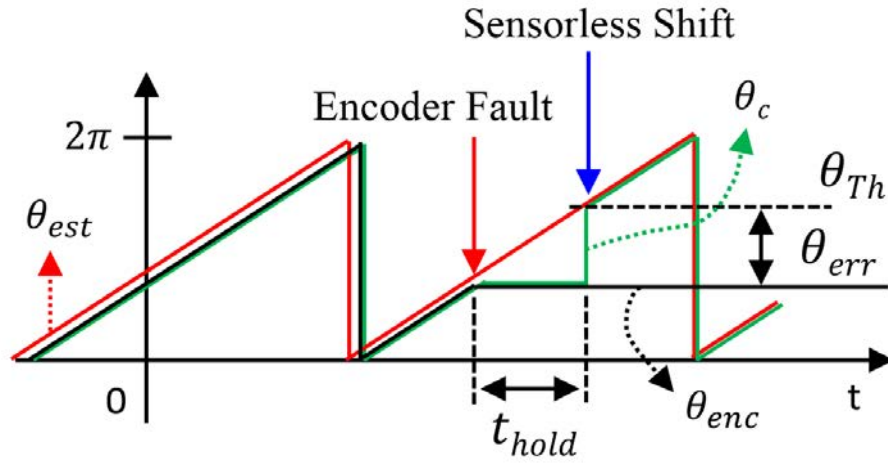


Fig. 5.1 Encoder fault detection using rotor position error

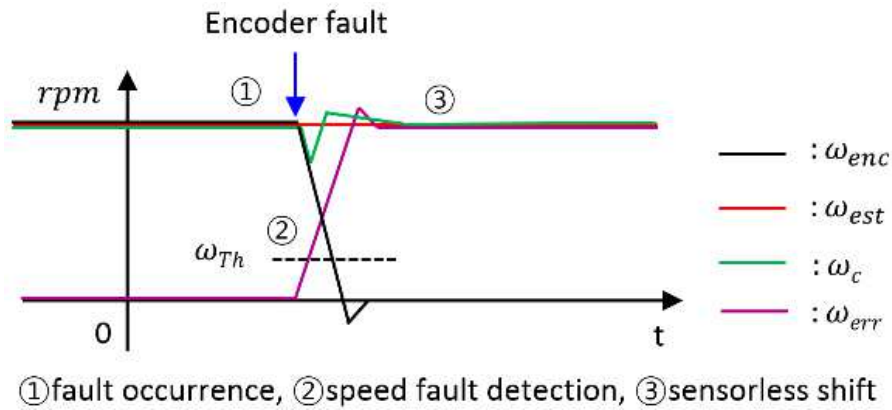


Fig. 5.2 Encoder fault detection using rotor speed error

Hence, the low threshold value can be set to short holding time and fast fault detection ^{[64] [65]}

However, the difference angle θ_{err} has a high overshoot in acceleration and deceleration by selecting the PLL-type estimator gain. The high overshoot of θ_{err} makes θ_{Th} higher value than necessity. The high θ_{Th} has a long holding time t_{hold} which will tend to increase the current ripple of dq-axis. Therefore, the threshold value selection considering the overshoot value θ_{err} with estimator gain is vital for fast fault detection and stable algorithm transition ^{[26] [49] [50]}. The flow chart for encoder fault detection using rotor angle error is shown in Fig. 5.3. The sensorless algorithm selection can be carried out from difference value between θ_{err} and θ_{Th} . In the case of rotor speed error, there is also same flow chart.

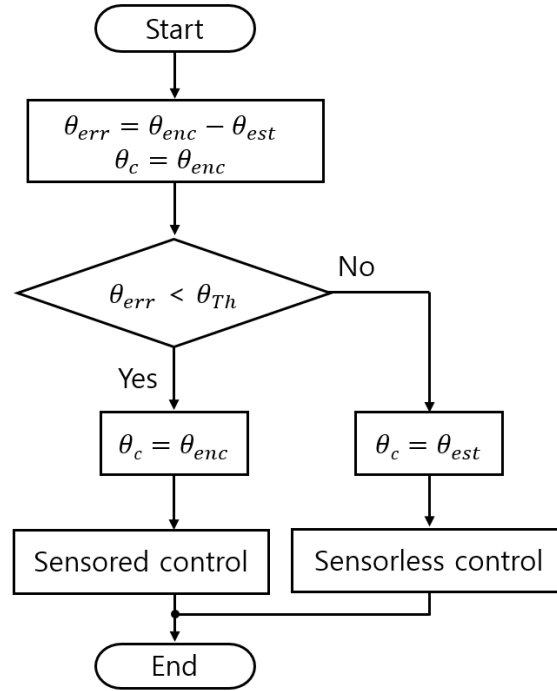


Fig. 5.3 Flow chart for encoder fault detection using rotor angle error

5.3 CUSUM algorithm application

The selection of threshold values is important for stable algorithm transition. If a low threshold value is set to fault detection, the fast algorithm transition is possible. However, the sensitivity on noise signal and overshoot value of θ_{err} and ω_{err} during acceleration and deceleration will be increased. On the other hand, if a high threshold value is set, the fault detection time will be increased. The delayed fault detection has a disadvantage on torque ripple and unstable algorithm transition. To solve this problem, we consider a CUSUM algorithm to define the stable threshold value. Sensor fault detection and isolation (FDI) method using CUSUM algorithm are studied by many authors in [25]. The merit of CUSUM algorithm is robustness on parameter variation and uncertainty. A mathematical theory of the CUSUM algorithm is defined as below ^[26].

$$g(k) = \text{MAX} \left(0, g(k-1) + \left(r(k) - \frac{\mu_0 + \mu_1}{2} \right) \right) \quad (5.1)$$

where μ_0 and μ_1 are the mean value of signal θ_{err} or ω_{err} before and after respectively when the fault occurs. The mean value μ_0 and μ_1 can be defined as $\mu_0 = |\Delta\theta_{Lq}| + |\Delta\theta_{\max_st} -$

$\Delta\theta_{\min_st}$, $\mu_1 = \mu_0 + |\Delta\theta_\rho|$ respectively. Where $\Delta\theta_{Lq}$ is the angle variance of estimated position error $\Delta\theta$ caused by L_q variation. The $\Delta\theta_{\max_st}$ and $\Delta\theta_{\min_st}$ are maximum and minimum angle variance of $\Delta\theta$ by influencing the motor parameter variation and noise signals in steady state. Also, $\Delta\theta_\rho$ is the angle variance of $\Delta\theta$ by selecting the PLL-type estimator bandwidth in transient state. $r(k)$ is the input signal of the CUSUM algorithm. $g(k)$ is set to zero value before the fault detection because the $r(k)$ is more low value than $(\mu_0 + \mu_1)/2$ in right side term of *MAX* function. However, if the fault occurs, the output of *MAX* function becomes positive value and is rapidly increased as the value of $r(k)$ is increased. Fig. 5.4 shows this logic flow on fault detection. Therefore, the fault detection can be defined by selected threshold value. The threshold value h can be calculated as follows ^[26].

$$h = \frac{\Delta t_{det}}{t_s} \left(\mu_1 - \frac{\mu_0 + \mu_1}{2} \right) \quad (5.2)$$

where Δt_{det} is fault detection delay time and t_s is sampling time. Hence, the selection of μ_0 and μ_1 considering errors in steady state and transient state is important to detect the fault.

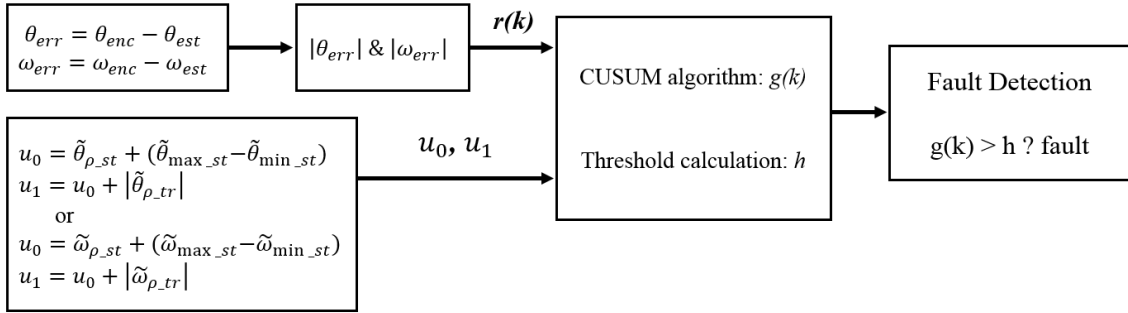


Fig. 5.4 Block diagram on position and speed sensor fault detection

5.4 Adaptive threshold design

Under the transient state condition, the last term of (3.5.b) cannot be ignored since the speed error could be large. So, from (3.5.b), we can be defined as is (5.3)

$$\tan^{-1} \left(\frac{\hat{e}_\gamma}{\hat{e}_\delta} \right) = \Delta\hat{\theta} + \tan^{-1} \left(\frac{\Delta\omega_r \cdot L_d \cdot i_q}{E_{ex} + \Delta\omega_r \cdot L_d \cdot i_d} \right) \quad (5.3)$$

$$y = \tan^{-1} \left(\frac{\Delta\omega_r \cdot L_d \cdot i_q}{E_{ex} + \Delta\omega_r \cdot L_d \cdot i_d} \right) = \theta_{ac} \quad (5.4)$$

Where $y' = 0$ is maximum or minimum value of θ_{ac} . Therefore we can find maximum overshoot value in transient state such as acceleration or deceleration.

$$\frac{dy}{dt} \frac{d}{dy} [\tan(y)] = \frac{d}{dt} \left(\frac{\Delta\omega_r \cdot L_d \cdot i_q}{E_{ex} + \Delta\omega_r \cdot L_d \cdot i_d} \right) \quad (5.5)$$

$$\frac{dy}{dt} \sec^2(y) = \left(\frac{(\Delta\omega_r \cdot L_d \cdot i_q)' (E_{ex} + \Delta\omega_r \cdot L_d \cdot i_d) - (\Delta\omega_r \cdot L_d \cdot i_q) (E_{ex} + \Delta\omega_r \cdot L_d \cdot i_d)'}{(E_{ex} + \Delta\omega_r \cdot L_d \cdot i_d)^2} \right) \quad (5.5)$$

Assuming i_d, i_q, L_{dq} are constant during sampling time,

$$E_{ex} = \omega_r (\Delta L \cdot i_d + \phi) - \Delta L \cdot p \cdot i_q \quad (5.6)$$

$$\frac{dy}{dt} = \left(\frac{(\Delta\theta_r'' L_d i_q)(\omega_r (\Delta L \cdot i_d + \phi) + \Delta\omega_r L_d i_d) - (\Delta\omega_r L_d i_q)(\omega_r' (\Delta L \cdot i_d + \phi) + \Delta\theta_r'' L_d i_d)'}{\sec^2(y) \cdot (E_{ex} + \Delta\omega_r \cdot L_d \cdot i_d)^2} \right) \quad (5.7)$$

Where ΔL is $L_d - L_q$. And If $\frac{dy}{dt} = 0$ and $\Delta\theta_r$ is a limited value, the numerator can be set to zero.

$$\begin{aligned} & (\Delta\theta_r'' L_d i_q)(\omega_r (\Delta L \cdot i_d + \phi) + \Delta\omega_r L_d i_d) - (\Delta\omega_r L_d i_q)(\omega_r' (\Delta L \cdot i_d + \phi) + \Delta\theta_r'' L_d i_d) \\ & = K \omega_r \Delta\theta_r'' - K \omega_r' \Delta\theta_r' = K \omega_r y'' - K \omega_r y' = 0 \end{aligned} \quad (5.8)$$

Where K is $(\Delta L i_d + \phi) \cdot L_d i_q$. From general solution

$$y = C_1 + C_2 e^{\left(\frac{\omega_r}{\omega_r'} \right) t} \quad (5.9)$$

Assuming initial condition is $\Delta\theta_r(0) = \Delta\theta_{r0}$ and $\Delta\theta_r'(0) = \Delta\omega_{r0}$,

$$\Delta\hat{\theta}_{Th_r} = \Delta\hat{\theta}_{Th_r0} - \Delta\hat{\omega}_{Th_r0} \cdot \frac{\omega_r}{\omega_r'} + \Delta\hat{\omega}_{Th_r0} \cdot \frac{\omega_r}{\omega_r'} \cdot e^{\left(\frac{\omega_r}{\omega_r'} \right) t} \quad (5.10)$$

Therefore, $\Delta\hat{\theta}_{Th_r}$ can be used to adaptive threshold design to fast fault detection instead of maximum error value $\Delta\theta_p$ in transient state such as acceleration and deceleration.

5.5 Algorithm transition analysis

5.5.1 Experimental results on parameter variation

Fig. 5.5 shows the position difference error θ_{err} on the variation of motor parameters in constant speed. Motor parameters were modified by control variables of inverter system. θ_{err} is increased by twice in low speed. Fig. 5.6 shows the variation of θ_{err} under 1.8 Nm (100% load). The variation of q-axis inductance L_q increases the rapid change of θ_{err} about twice. Therefore, the increased θ_{err} and ω_{err} due to motor parameter variation have to be applied μ_0 related to (5.1) and (5.2).

Fig. 5.7 shows the difference error of speed and position on ρ value from 50 rad/s to 300 rad/s at 500 min^{-1} . The θ_{err} and ω_{err} are gradually increased as ρ value is increased. The bandwidth ρ of PLL-type estimator is set to 100 rad/s considering minimum speed 300 min^{-1} of sensorless control.

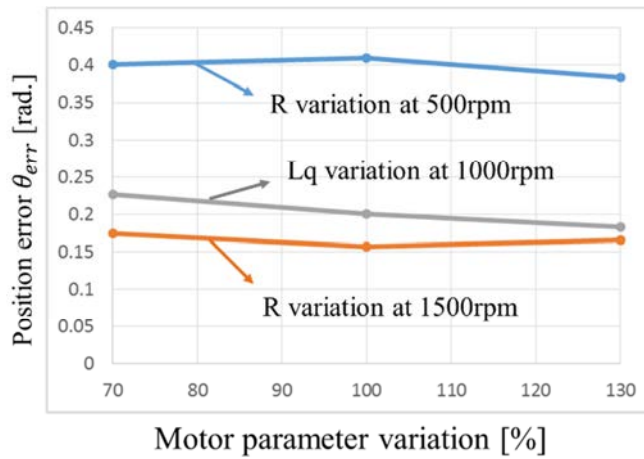


Fig. 5.5 Position error on variation of parameters under 0.1 Nm

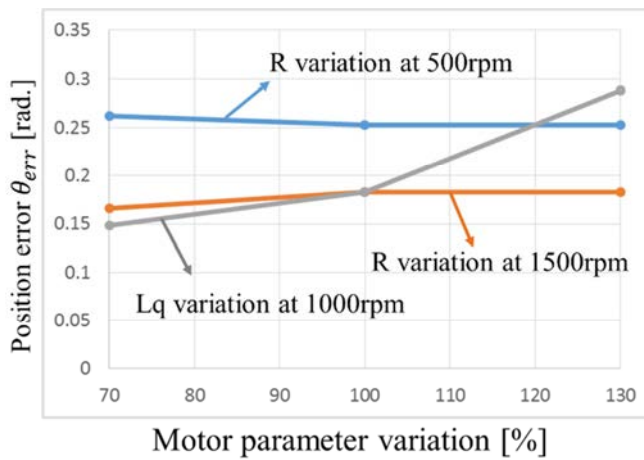


Fig. 5.6 Position error on variation of parameters under 1.8 Nm

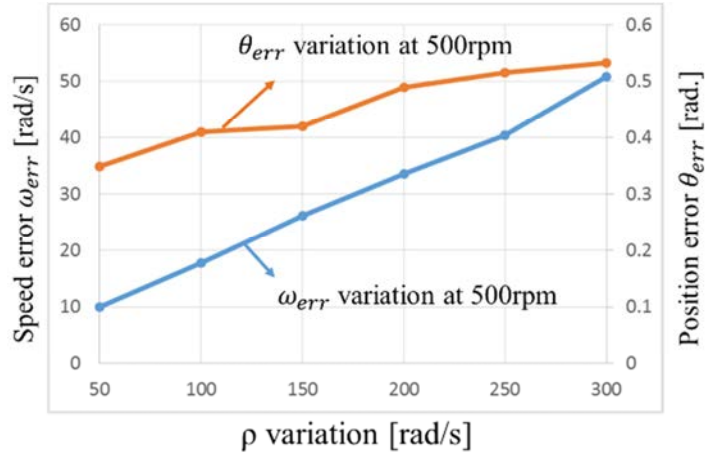


Fig. 5.7 Speed and position error on ρ variation under 0.1 Nm

5.5.2 Simulation and experimental results

The holding time during algorithm transition is occurred. This effect makes the overshoot of dq-axis current such as the simulation results of Fig. 5.8. Therefore, the performance comparison between conventional sensorless algorithm and sensorless algorithm including proposed method can be validated by the overshoot value of dq-axis current during holding time. Fig. 5.9 and Fig. 5.10 show the simulation results on the overshoot of estimated position error in algorithm transition with the gain variation of ρ and g_{ob} . In accordance with proposed stable gain selection process, If ρ is set to 100 rad/s and g_{ob} is set to 1000 rad/s, the estimated position errors are limited to 50 degree.

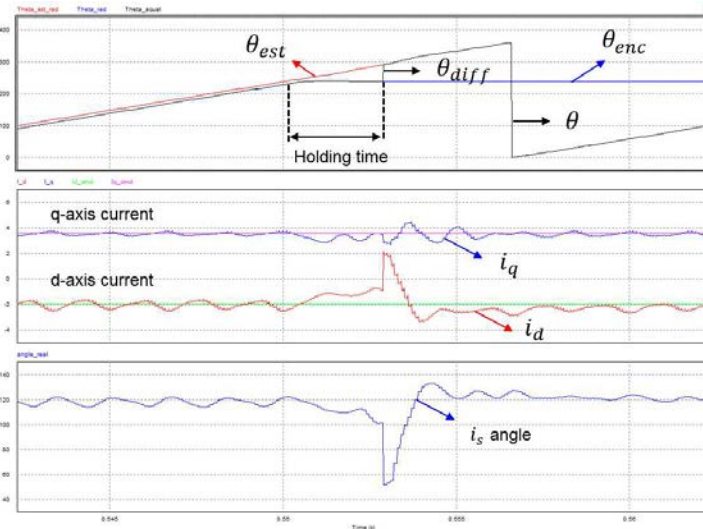


Fig. 5.8 Overshoot of dq-axis current during holding time at 1500 min^{-1} under 1.8 Nm

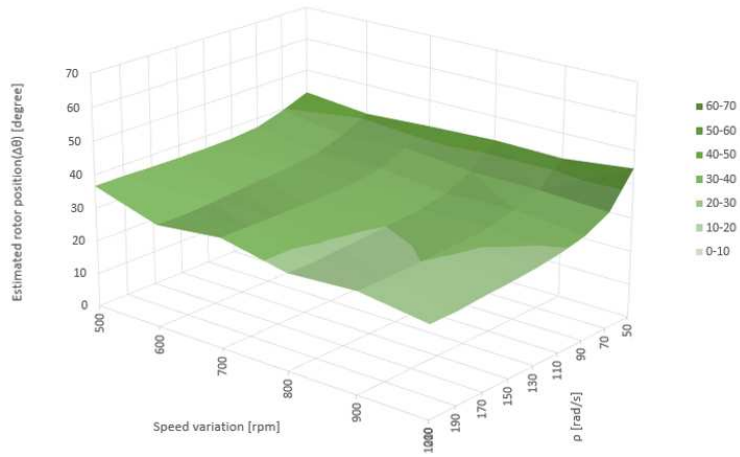
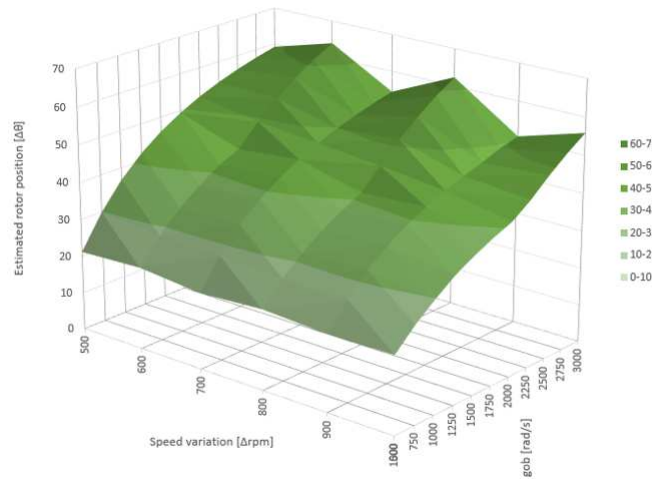
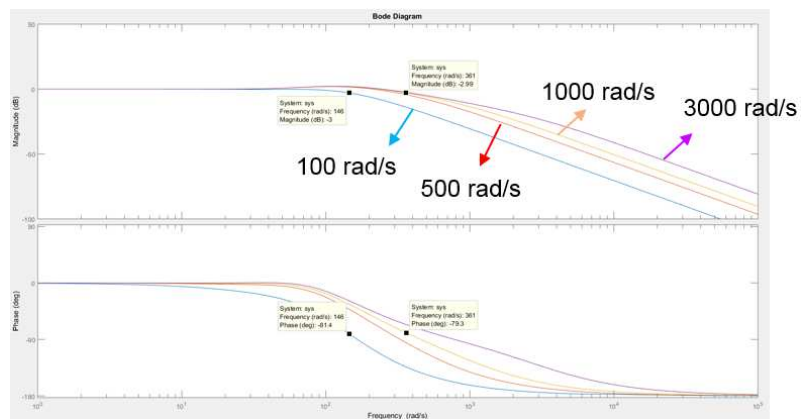


Fig. 5.9 Overshoot of $\Delta\hat{\theta}$ on the variation of PLL-type estimator gain ρ under 1.8 Nm



(a) Overshoot of $\Delta\hat{\theta}$ on the variation of disturbance observer gain g_{ob}



(b) Frequency response on disturbance observer gain g_{ob}

Fig. 5.10 Overshoot of estimated position error in algorithm transition under 1.8 Nm

In accordance with experimental result in section 5.5.1, The parameters of CUSUM algorithm in (5.1) and (5.2) is selected as below

For, $\mu_0 = 21.36$ rad/s, $\mu_1 = 52.4$ rad/s for speed error threshold h_s , $\mu_0 = 0.45$ rad., $\mu_1 = 0.88$ rad. for position error threshold h_p , $\Delta t_{det} = 1$ ms, $t_s = 0.1$ ms, it gives $h_s = 155.19$ and $h_p = 2.14$. Also, the error effect of parameter variation are reflected in μ_0 and μ_1 .

Fig. 5.11 and Fig. 5.12 show the algorithm transition waveforms using ω_{err} . Although high ripple is included in ω_{err} , the fault detection and algorithm transition are controlled by CUSUM algorithm. The sensorless flag is set to 1 when $g(k)$ value exceeds the h_s value in Fig. 5.12. However, the ω_{err} waveform shows high overshoot under 1.8 Nm load in Fig. 5.13. Also, high torque ripple occurs during algorithm transition by q-axis current variation.

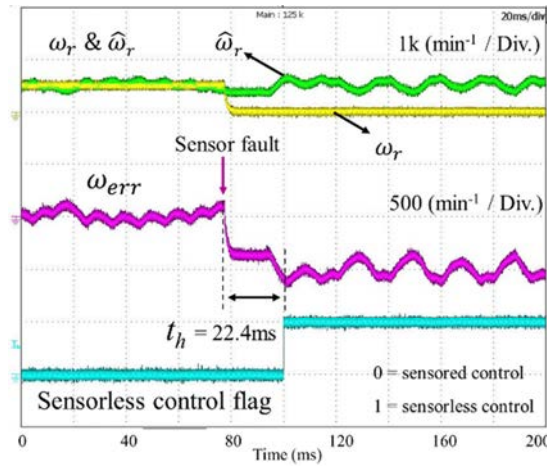


Fig. 5.11 Algorithm transition using ω_{err} under 0.1 Nm

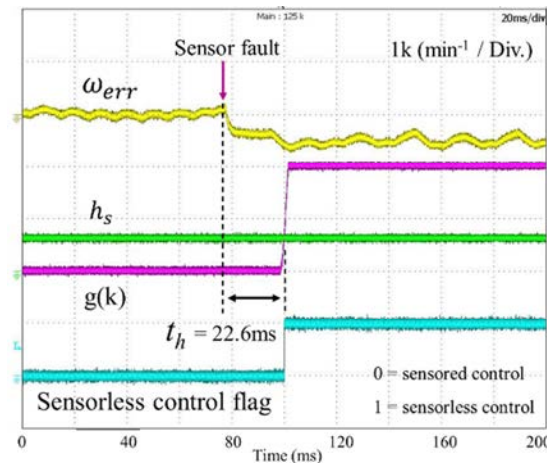


Fig. 5.12 Threshold value of CUSUM algorithm under 0.1 Nm

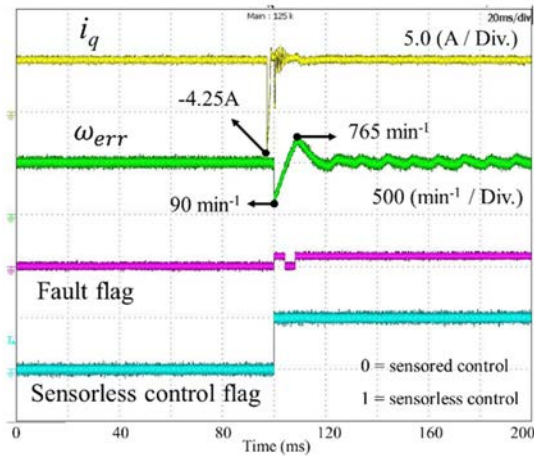


Fig. 5.13 Overshoot waveforms under 1.8 Nm

Fig. 5.14 shows the simulation result of adaptive threshold using proposed method in sensed control under 0.1 Nm. The $\Delta\hat{\theta}_{Th_r}$ have a higher value than $r(k)$ maximum value during acceleration and deceleration in normal operating condition. Therefore, the lower threshold value is available and fast fault detection can be achieved.

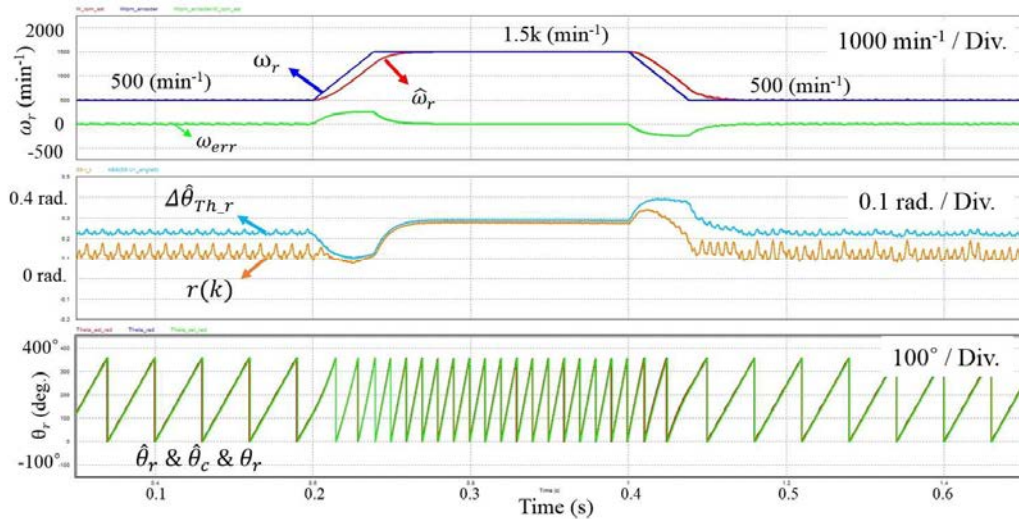


Fig. 5.14 Waveforms of adaptive threshold method in transient state under 0.1 Nm

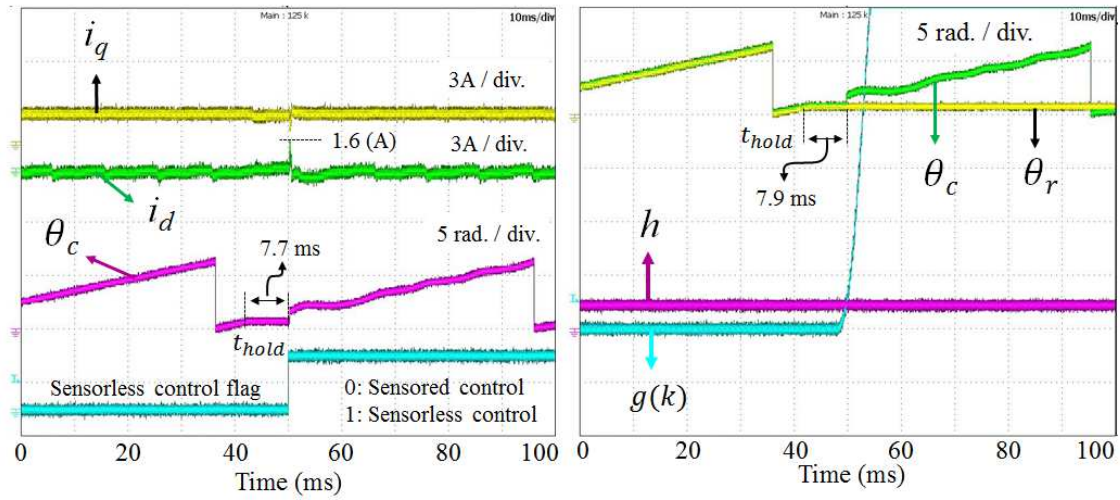


Fig. 5.15 Overshoot of d-q axis current and holding time in conventional threshold method at 500 min^{-1} under 0.5 Nm

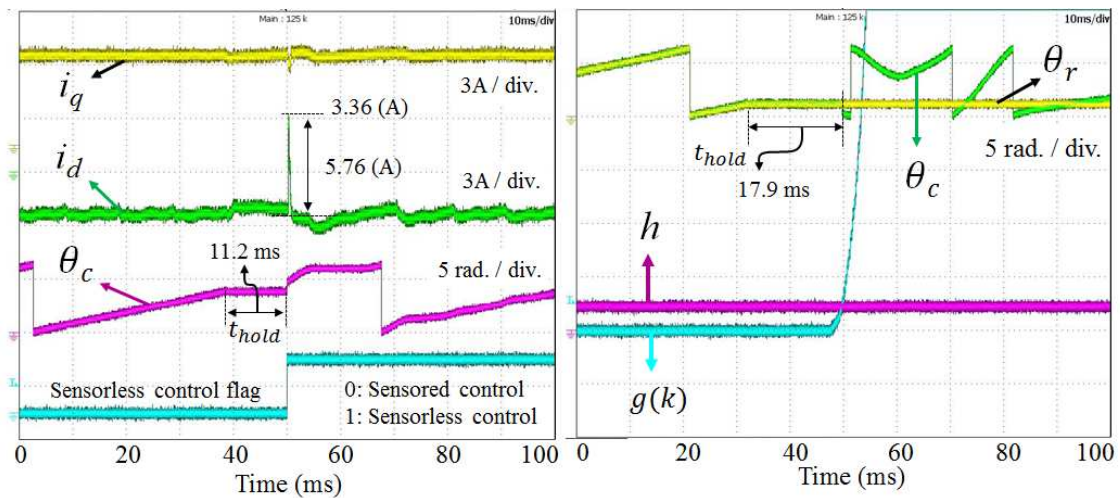


Fig. 5.16 Overshoot of d-q axis current and holding time in conventional threshold method at 500 min^{-1} under 1.8 Nm

Fig. 5.15 and Fig. 5.16 show the experimental results on the overshoot of d-q axis current and holding time t_{hold} in conventional method at 500 min^{-1} . The t_{hold} is 11.2 ms and the overshoot current of d-axis is 5.76 A under 1.8 Nm. In this condition, the algorithm transition is unstable due to long holding time.

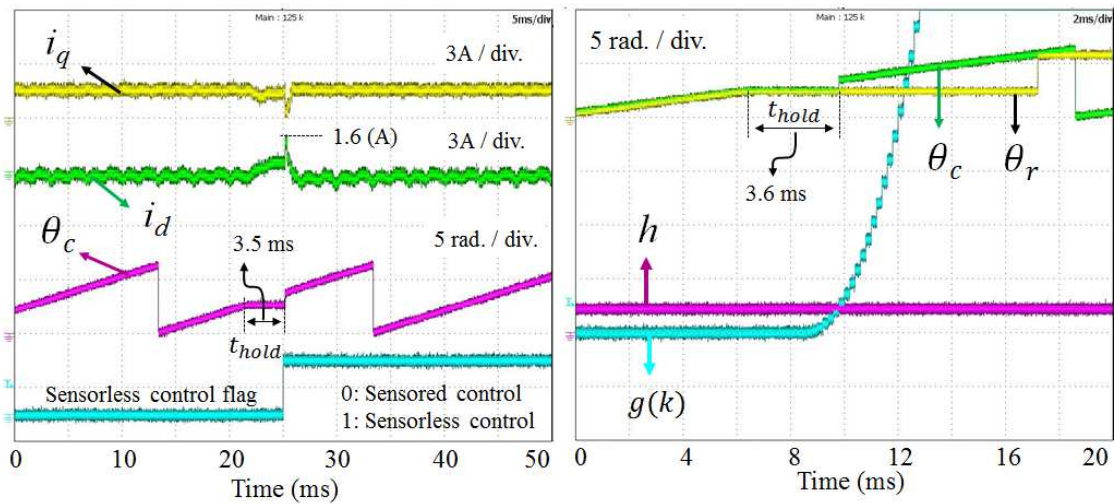


Fig. 5.17 Overshoot of d-q axis current and holding time in conventional threshold method under 1500 min^{-1} & 0.5 Nm

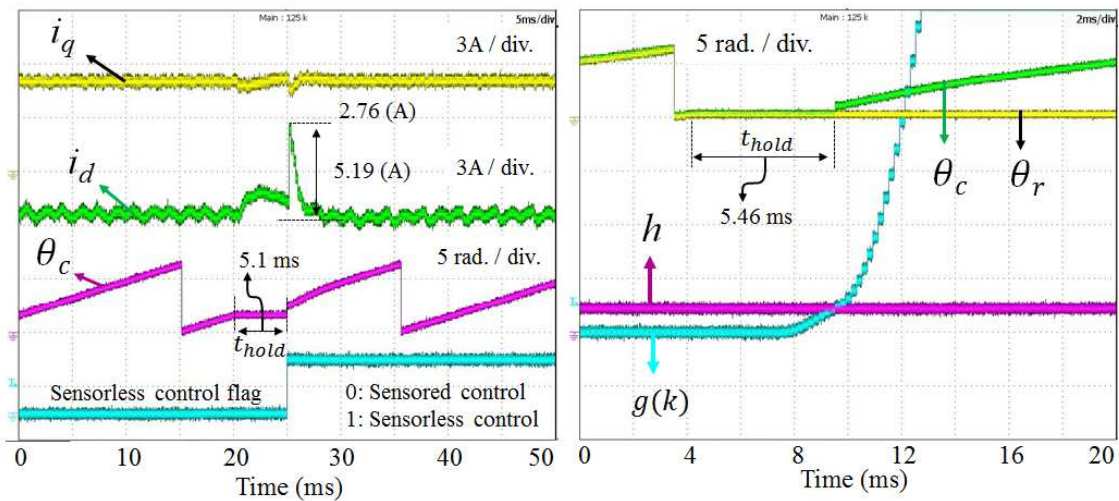


Fig. 5.18 Overshoot of d-q axis current and holding time in conventional threshold method under 1500 min^{-1} & 1.8 Nm

Fig. 5.17 and Fig. 5.18 show the experimental results on the overshoot of d-q axis current and holding time t_{hold} in conventional method at 1500 min^{-1} . The t_{hold} is 5.1 ms and the overshoot current of d-axis is 5.19 A under 1.8 Nm. In this condition, the algorithm transition is possible. However, d-axis current ripple is still high.

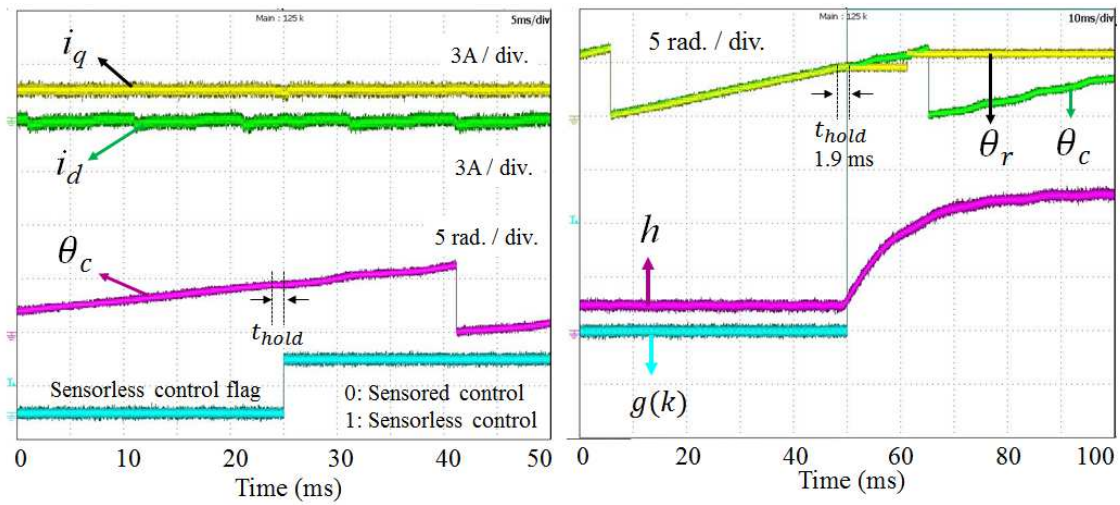


Fig. 5.19 The overshoot of d-q axis current and rotor angle error in adaptive threshold method under 500 min^{-1} & 0.5 Nm

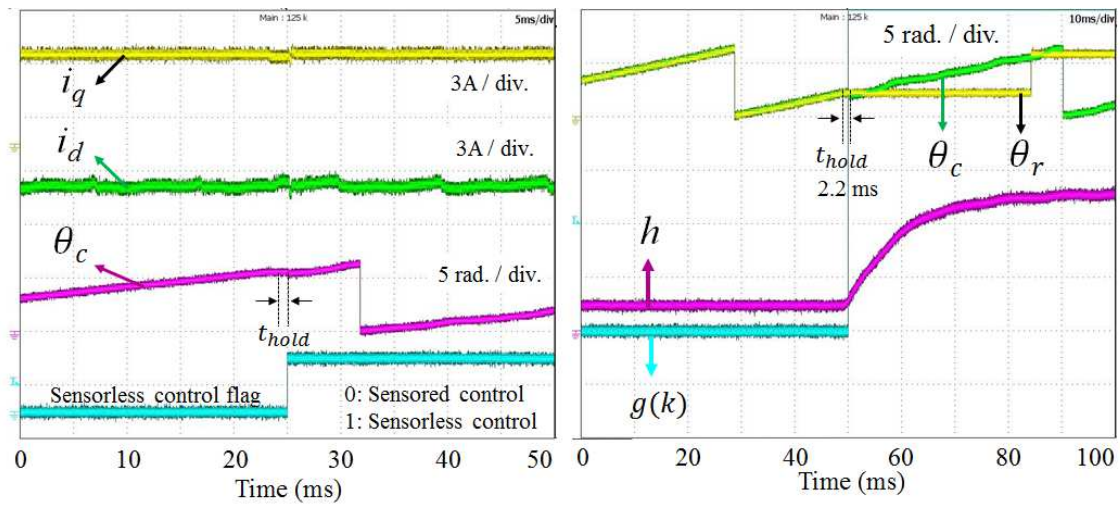


Fig. 5.20 The overshoot of d-q axis current and rotor angle error in adaptive threshold method under 500 min^{-1} & 1.8 Nm

Fig. 5.19 and Fig. 5.20 show the d-q axis current and t_{hold} under proposed method at 500 min^{-1} . The d-q axis current ripple is decreased by the adaptive threshold method because the holding time is decreased from 11.2 ms to 2.2ms under 1.8 Nm. Therefore, the algorithm transition is stable with low current ripple.

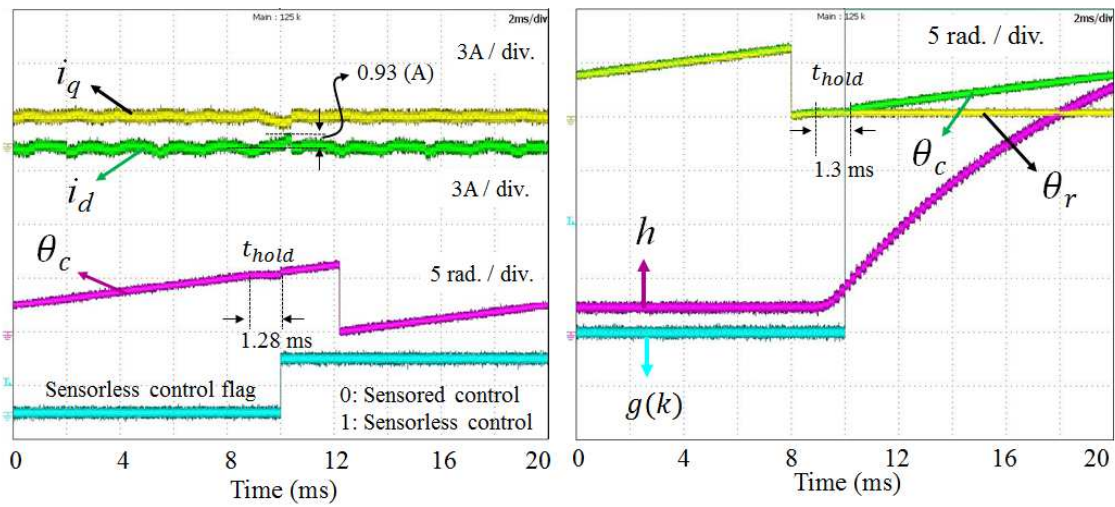


Fig. 5.21 The overshoot of d-q axis current and rotor angle error in adaptive threshold method under 1500 min^{-1} & 0.5 Nm

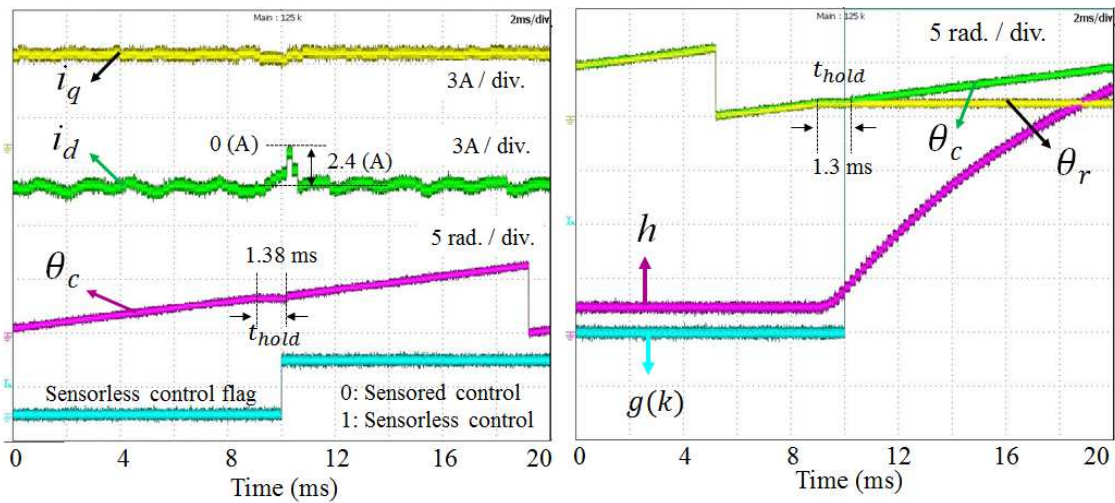


Fig. 5.22 The overshoot of d-q axis current and rotor angle error in adaptive threshold method under 1500 min^{-1} & 1.8 Nm

Fig. 5.21 and Fig. 5.22 show the d-q axis current and t_{hold} under proposed method at 1500 min^{-1} . The d-q axis current ripple is decreased by the adaptive threshold method because the holding time is decreased from 5.1 ms to 1.38 ms under 1.8 Nm. Therefore, the algorithm transition is stable with low current ripple.

5.6 xEV application of proposed algorithms

Fig. 5.23 presents the block diagram of proposed algorithm for xEV. The controller gains can be selected by stable gain selection process in section 3.7. Next, the compensated angle and speed are defined from proposed current feedback control and compensated PLL-type estimator. Lastly, the sensor fault detection and algorithm transition can be calculated in (5.1) and (5.2) from difference between estimated value and sensor value. Therefore, the algorithm design for stable sensorless control, fast fault detection and algorithm transition can be defined.

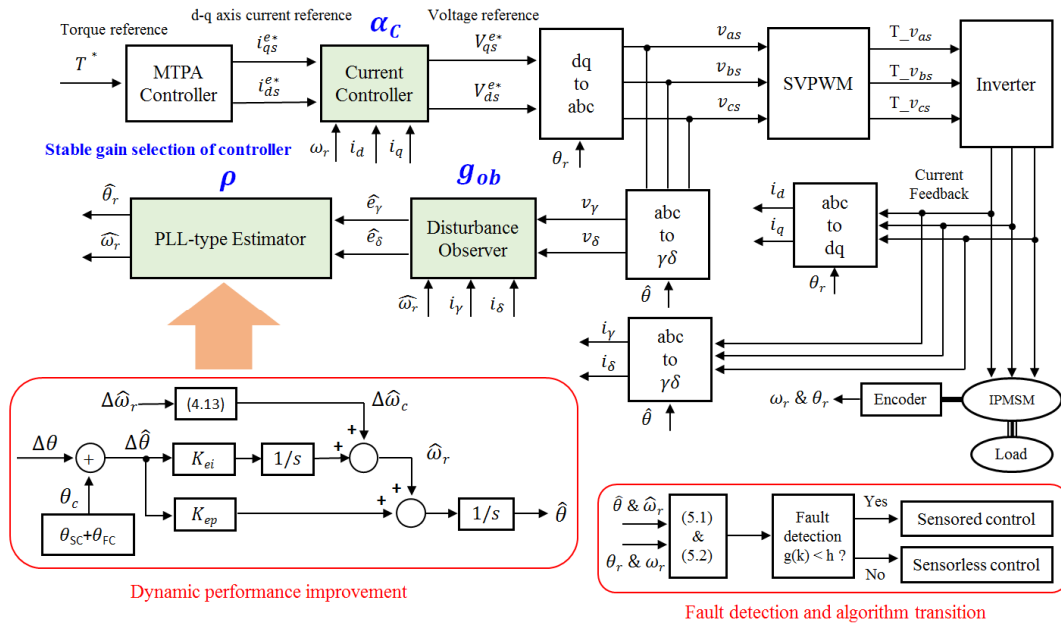


Fig. 5.23 Proposed algorithm application for xEV drive system

5.7 Chapter summary

This chapter has proposed a stable fault detection method using the CUSUM algorithm and the selection method of threshold value considering relation between PLL-type estimator gain and overshoot value of θ_{err} and ω_{err} . When position sensor fault occurs, the stable algorithm transition can be observed with the calculated threshold value considering the errors of steady state and transient state such as acceleration and deceleration with θ_{err} error. However, the conventional method using ω_{err} threshold value is unstable under high torque due to the increased overshoot value of ω_{err} . Also, the algorithm transition using θ_{err} which does not utilize adaptive threshold method is unstable at low speed under 1.8 Nm. Therefore, the proposed method can be helpful for the algorithm transition of xEV application.

Chapter 6 Conclusion

6.1 Conclusion of this paper

This paper proposes a stable gain selection method considering the fast dynamics and low noise sensitivity for sensorless control and easy algorithm conversion when position sensor fault occurs. The bandwidth of PLL-type estimator for IPMSM has been analyzed regarding stable range. When using a 100 rad/s for PLL-type estimator, the torque step response and speed rampwise response are stable. The disturbance observer gain for the extended back-EMF estimation has been studied. By the selection strategy of sensorless control factors, the stable operation point could be defined and verified through experiment. Also, the computer simulation and experimental results show the effectiveness of our proposed selection strategy in the transient state of speed and torque.

The overshoot peak values of estimated position error are limited a lower value than the results of uncompensated sensorless control from the proposed control method and the estimator bandwidth selection considering stable bandwidth range. Also, the bandwidth of conventional PLL-type estimator for the rotor and speed estimation of IPMSM has been analyzed in speed variation. When using the proposed strategy in fast speed variation, the transient performance could be improved. The proposed methods include the angle compensation term and speed compensation term. So, the fast fault detection and algorithm transition are possible.

A stable fault detection method using the CUSUM algorithm and the selection method of threshold value considering relation between PLL-type estimator gain and overshoot value of θ_{err} and ω_{err} has discussed. The proposed method using adaptive threshold value could reduce the holding time for fault detection because the high threshold value considering the overshoot value of $\Delta\theta_{err}$ in motor acceleration and deceleration could be decreased. Therefore, the algorithm transition period could be decreased and the overshoot of d - q axis current and torque response could be lower with proposed fault detection method.

6.2 Issue and future task

When position sensor fault occurs, the stable algorithm transition can be observed with the calculated threshold value considering the errors of steady state and transient state such as acceleration and deceleration with θ_{err} error. However, the method using ω_{err} threshold value is unstable under high torque due to the increased overshoot value of ω_{err} in acceleration or deceleration. Therefore, the additional research about low overshoot of ω_{err} will be carried to

stable control system for fault detection. Also, Since the fast fault detection and stable algorithm transition are related to threshold value considering the overshoot value of θ_{err} and ω_{err} , the additional study on the variation of threshold value is necessary with the effect of current sensor error and motor parameter variation ^{[48][69]}.

Reference

- [1] U.S. department of energy <https://www.metroplugin.com/2012/02/ev-industry-myth-vs-fact/>
- [2] UBS(Union Bank Switzerland) estimates <https://neo.ubs.com/shared/d1ZTxnvF2k/>
- [3] Global EV outlook 2018 <https://www.iea.org/>
- [4] S. Christiaens, J. Ogrzewalla, and S. Pischinger, “Functional safety for hybrid and electric vehicles,” Soc. Automative Eng. Int., Geneva, Switzerland, SAE Tech. Paper 2012-01-0032, 2012.
- [5] A. Cordoba Arenas, J. Zhang, and G. Rizzoni, “Diagnostics and prognostics needs and requirements for electrified vehicles powertrains,” in Proc. IFAC, pp. 524–529, 2013.
- [6] K.Rajashekara, “Present status and future trends in electric vehicle propulsion technologies,” IEEE J. Emerg. Sel. Topics Power Electron., vol. 1, no. 1, pp. 3–10, Mar. 2013.
- [7] P. Pillay and R. Krishnan, “Application characteristics of permanent magnet synchronous and brushless dc motors for servo drives,” IEEE Transactions on Industry Applications, vol. 27, no. 5, pp. 986–996, Sep. 1991.
- [8] R. Wu and G. Slemon, “A permanent magnet motor drive without a shaft sensor,” IEEE Trans. Ind. Applicat., vol 27, pp. 1005-1011, Sept./Oct. 1991.
- [9] P. Pillay and R. Krishnan, “Application characteristics of permanent magnet synchronous and brushless dc motors for servo drives,” in Conf. Rec. IEEEIAS Annual. Meeting, vol.3, no. pp.1814-1819, 2000.
- [10]S. Morimoto, K. Kawamoto, M. Sanada and Y. Takeda, “Sensorless control strategy for salient-pole PMSM based on extended EMF in rotating reference frame,” IEEE Trans. Ind. Application, vol.38, no. pp.1054-1061, 2002.
- [11]J.-S. Kim and S.-K. Sul, “High performance PMSM drives without rotational position sensors using reduced order observer,” in Industry Applications Conference, 1995. Thirtieth IAS Annual Meeting, IAS '95., Conference Record of the 1995 IEEE, 1995.
- [12]Z. Chen, M. Tomita, S. Ichikawa, S. Doki, and S. Okuma, “Sensorless control of interior permanent magnet synchronous motor by estimation of an extended electromotive force, in Proc. Conf. Rec. IEEE-IAS, vol. 3, pp. 1814–1819, Oct., 2000.
- [13]L. Ribeiro, M.C.Harke, and R. Lorenz, “Dynamic properties of backemf based sensorless drives,” Proc. of the IAS Annual Meeting, vol. 1, pp. 2026–2033, Oct. 2006.

Reference

- [14]S. Ichikawa, C. Zhiqian, M. Tomita, S. Doki, and S. Okuma, "Sensorless control of an interior permanent magnet synchronous motor on the rotating coordinate using an extended electromotive force," Proc. IECON'01, vol. 3, no. 29, pp. 1667–1672, Dec. 2001.
- [15]J. S. Kim and S. K. Sul, "New approach for high performance PMSM drives without rotational position sensors," IEEE Trans. Power Electron., vol. 12, pp. 904–911, Sept. 1997.
- [16]H. Jang, S. K. Sul, J. I. Ha, K. Ide, and M. Sawamura, "Sensorless drive of surface-mounted permanent-magnet motor by high-frequency signal injection based on magnetic saliency," IEEE Trans. Ind. Appl., vol.39, no.4, pp.1031–1039, 2003.
- [17]Ji-Hoon Jang, Jung-Ik Ha, Motomichi Ohto, Kozo Ide, Seung-Ki Sul, "Analysis of Permanent-Magnet Machine for Sensorless Control Based on High-Frequency Signal Injection," IEEE Transaction on Industry Application, vol.40, no.6, pp 1595-1604, November 2004.
- [18]Y. D. Yoon, S. K. Sul, S. Morimoto and K. Ide, "High bandwidth sensorless algorithm for AC machines based on square-wave type voltage injection," in Conf. Rec. IEEE ECCE, pp. 2123-2130, 20-24 Sep. 2009.
- [19]H. Kim and R. Lorenz, "Carrier signal injection based sensorless control methods for IPM synchronous machine drives," in Conf. Rec. IEEE IAS Annu. Meeting, vol. 2, pp. 977–984, 2004.
- [20]Lennart Harnefors and Hans-Peter Nee, "A General Algorithm for Speed and Position Estimation of AC Motors," IEEE Trans. Ind. Elec., vol.47, no.1, pp.77-83, 2000.
- [21]Oskar Wallmark, Lennart Harnefors, and Ola Carlson, "An Improved Speed and Position Estimator for Salient Permanent-Magnet Synchronous Motors," IEEE Trans. Power Electron., vol.52, no.1, pp.255-262, 2005.
- [22]K.Rajashekara, "Present status and future trends in electric vehicle propulsion technologies," IEEE J. Emerg. Sel. Topics Power Electron., vol. 1, no. 1, pp. 3–10, Mar. 2013.
- [23]H. Berriri, M. W. Naouar, and I. Slama-Belkhdja, "Easy and fast sensor fault detection and isolation algorithm for electrical drives," IEEE Trans. Power Electron., vol.27, no.2, pp.490–499, 2012.
- [24]S. Huang, K. K. Tan, and T. H. Lee, "Fault diagnosis and fault-tolerant control in linear drives using the Kalman filter," IEEE Trans. Ind. Electron., vol.59, no.11, pp.4285–4292, 2012.
- [25]K. Rothenhagenand and F. W. Fuchs, "Doubly fed induction generator model-based sensor fault detection and control loop reconfiguration," IEEE Trans. Ind. Electron., vol. 56, no. 10, pp. 4229–4238, Oct. 2009.
- [26]F. Meinguet, P. Sandulescu, X. Kestelyn, and E. Semail, "A method for fault detection and isolation based on the processing of multiple diagnostic indices: Application to inverter faults in AC drives," IEEE Trans. Veh. Technol., vol. 62, no. 3, pp. 995–1009, Dec. 2012.

Reference

- [27] Y.-S. Jeong, S.-K. Sul, S. E. Schulz, and N. R. Patel, "Fault detection and fault-tolerant control of interior permanent-magnet motor drive system for electric vehicle," *IEEE Trans. Ind. Appl.*, vol. 41, no. 1, pp. 46–51, Jan./Feb. 2005.
- [28] K. Rothenhagen and F. W. Fuchs, "Current sensor fault detection, isolation, and reconfiguration for doubly fed induction generators", *IEEE Transactions on Industrial Electronics*, vol. 56, no. 10, pp. 4239-4245, Oct. 2009.
- [29] K.-S. Lee, J.-S. Ryu, "Instrument fault detection and compensation scheme for direct torque controlled induction motor drivers", *IEEE Proc.-Control Theory Appl.*, vol. 150, no. 4, 2003.
- [30] G. H. B. Foo, X. Zhang, and D.M. Vilathgamuwa, "A sensor fault detection and isolation method in interior permanent-magnet synchronous motor drives based on an extended Kalman filter," *IEEE Trans. Ind. Electron.*, vol. 60, no. 8, pp. 3485–3495, Aug. 2013.
- [31] O. Wallmark, L. Harnefors, and O. Carlson, "Control algorithms for a fault-tolerant PMSM drive," *IEEE Trans. Ind. Electron.*, vol. 54, no. 4, pp. 1973–1980, Aug. 2007.
- [32] Z. Gao, C. Cecati, S. X. Ding, "A survey of fault diagnosis and fault-tolerant techniques part I: fault diagnosis with model-based and signal-based approaches," *IEEE Trans. Ind. Electron.* vol. 62, no.6, pp. 3757–3767, 2015.
- [33] M. E.H. Benbouzid, D. Diallo, and M. Zeraouia, "Advanced fault-tolerant control of induction-motor drives for EV/HEV traction applications: From conventional to modern and intelligent control techniques," *IEEE Trans. Veh. Technol.*, vol. 56, no. 2, pp. 519–528, Mar. 2007.
- [34] B. Akin, S. B. Ozturk, H. A. Toliyat, and M. Rayner, "DSP-based sensorless electric motor fault diagnosis tools for electric and hybrid electric vehicle powertrain applications," *IEEE Trans. Veh. Technol.*, vol. 58, no. 5, pp. 2150–2159, Jun. 2009.
- [35] Z. Q. Chen, M. Tomita, S. Doki, and S. Okuma, "An extended electromotive force model for sensorless control of interior permanent magnet synchronous motors," *IEEE Trans. Ind. Electron.*, vol. 50, no. 2, pp. 288–295, 2003.
- [36] R. Bojoi, M. Pastorelli, J. Bottomley, P. Giangrande, C. Gerada, "Sensorless control of PM motor drives — A technology status review," *IEEE Workshop on Electrical Machines Design Control and Diagnosis (WEMDCD)*, pp. 168-182, 2013.
- [37] H. Kim, M. C. Harke, and R. D. Lorenz, "Sensorless control of interior permanent-magnet machine drives with zero-phase lag position estimation," *IEEE Trans. Ind. Appl.*, vol. 39, no. 6, pp. 1726–1733, 2003.
- [38] G. C. Hsieh and J. C. Hung, "Phase-locked loop techniques. A survey," *IEEE Trans. Ind. Electron.*, vol. 43, no. 6, pp. 609–615, 1996.

Reference

- [39]K. W. Lee, S. Park, and S. Jeong, "A seamless transition control of sensorless PMSM compressor drives for improving efficiency based on a dual-mode operation," *IEEE Trans. Power Electron.*, vol. 30, no. 3, pp. 1446–1456, Mar. 2015.
- [40]R. Burgos, P. Kshirsagar, A. Lidozzi, J. Jang, F. Wang, D. Boroyevich, P. Rodriguez, and S.-K. Sul, "Design and evaluation of a PLL-based position controller for sensorless vector control of permanent-magnet synchronous machines," in *IECON 2006*, pp. 5081–5086, Nov 2006.
- [41]V. Kaura, V. Blasko, "Operation of a phase locked loop system under distorted utility conditions," *IEEE Transactions on Industry Applications*, vol.33, no.1 pp. 58-63, 1997.
- [42]S. Golestan, J. M. Guerrero, and J. C. Vasquez, "Three-phase PLLs: A review of recent advances," *IEEE Trans. Power Electron.*, vol. 32, no. 3, pp. 1894-1907, Mar. 2017.
- [43]O. Wallmark and L. Harnefors, "Sensorless control of salient PMSM drives in the transition region," *IEEE Trans. Ind. Electron.*, vol.53, no.4, pp.1179–1187, 2006.
- [44]D. Lee and K. Akatsu, "The study on gain selecting method of position sensorless control algorithm for IPMSM," in *2017 IEEE 12th International Conference on Power Electronics and Drive Systems (PEDS)*, pp.728-733, 2017.
- [45]D. Lee and K. Akatsu, "The study on transient performance improvement of position sensorless control algorithm for IPMSM," in *2017 IEEE Symposium on Sensorless Control for Electrical Drives (SLED)*, pp.67-72, 2017.
- [46]Stephen J. Chapman, "Electric machinery fundamentals" 2005.
- [47]R. W. Hejny, and R. D. Lorenz, "Evaluating the practical low-speed limits for back-EMF tracking-based sensorless speed control using drive stiffness as a key metric," *IEEE Trans. on Ind. Appl.*, vol.47, pp.1337–1343, 2011.
- [48]Y. Inoue, Y. Kawaguchi, S. Morimoto, and M. Sanada, "Performance improvement of sensorless IPMSM drives in a low-speed region using online parameter identification," *IEEE Trans. Ind. Appl.*, vol. 47, no. 2, pp. 798–804, 2011.
- [49]F. Meinguet, X. Kestelynx, E. Semailx, and J. Gyselinck, "Fault detection, isolation and control reconfiguration of three-phase PMSM drives," in *Proc. IEEE Int. Symp. Ind. Electron.*, pp. 2091–2096, 2011.
- [50]K. Rothenhagen and F. W. Fuchs, "Position estimator including saturation and iron losses for encoder fault detection of doubly-fed induction machine," in *13th International Power Electronics and Motion Control Conference*, pp. 1390–1397, 2008.
- [51]P. P. Vas, *Sensorless Vector and Direct Torque Control*. London, U.K.: Oxford Univ. Press, 1998.

Reference

- [52]D. Diallo, M. Benbouzid, A. Makouf, "A fault- tolerant control for induction motor drives in automotive applications," *IEEE Trans. Veh. Technol.*, vol.53, no.6, pp 1847-1855, 2004.
- [53]A. Akrad and M. Hilairret, "Design of a fault-tolerant controller based on observers for a PMSM drive," *IEEE Trans. Ind. Electron.*, vol. 58, no. 4, pp. 1416–1427, Apr. 2011.
- [54]S. Dwari and L. Parsa, "Fault-tolerant control of five-phase permanentmagnet motors with trapezoidal back EMF," *IEEE Trans. Ind. Electron.*, vol. 58, no. 2, pp. 476–485, Feb. 2011.
- [55]I. Hwang, S. Kim, Y. Kim, and C. E. Seah, "A survey of fault detection, isolation, and reconfiguration methods," *IEEE Transactions on Control Systems Technology*, vol. 18, no. 3, pp. 636–653, May 2010.
- [56]B. A. Welchko, T. A. Lipo, T. M. Jahns, and S. E. Schulz, "Fault tolerant three-phase AC motor drive topologies: A comparison of features, costs, and limitations," *IEEE Trans. Power Electron.*, vol. 19, no. 4, pp. 1108–1116, Jul. 2004.
- [57]Y. Leung, "Maximum likelihood voting for fault-tolerant software with finite output-space," *IEEE Trans. Rel.*, vol. 14, no. 3, pp. 419–427, Sep. 1995.
- [58]O. Wallmark, L. Hernefors, and O. Carlson, "Sensorless control of PMSM drives for hybrid electric vehicles," *IEEE PESC'04*, pp. 4017-4023, June 2004.
- [59]A. Piippo, M. Hinkkanen, and J. Luomi, "Analysis of an adaptive observer for sensorless control of interior permanent magnet synchronous motors," *IEEE Trans. Ind. Electron.*, vol. 55, no. 2, pp. 570–576, Feb. 2008.
- [60]G. Zhu, A. Kaddouri, L. A. Dessaint, and O. Akhrif, "A nonlinear state observer for the sensorless control of a permanent-magnet ac machine," *IEEE Trans. Ind. Electron.*, vol. 48, no. 6, pp. 1098–1108, Dec. 2001.
- [61]M. J. Corley, and R. D. Lorenz, "Rotor position and velocity estimation for a salient-pole permanent magnet synchronous machine at standstill and high speeds," *IEEE Trans. Ind. Appl.*, vol. 34, no. 4, pp. 784-789, Jul./Aug. 1998.
- [62]F.-J. Lin, Y.-C. Hung, J.-M. Chen, and C.-M. Yeh, "Sensorless IPMSM drive system using saliency back-EMF-based intelligent torque observer with MTPA control," *IEEE Trans. Ind. Informat.*, vol. 10, no. 2, pp. 1226–1241, May 2014.
- [63]M. N. Uddin, T. S. Radwan, and M. A. Rahman, "Performance of interior permanent magnet motor drive over wide speed range," *IEEE Trans. Energy Convers.*, vol. 17, no. 1, pp. 79–84, Mar. 2002.
- [64]S. K. Sul, Y. C. Kwon, and Y. Lee, "Sensorless control of IPMSM for last 10 years and next 5 years," *CES Transactions on Electrical Machines and Systems*, vol. 1, no. 2, pp. 91–99, 2017.

Reference

- [65]D.-W. Chung and S.-K. Sul, "Analysis and compensation of current measurement error in vector-controlled AC motor drives," *IEEE Trans. Ind. Appl.*, vol. 34, no. 2, pp. 340–345, Mar./Apr. 1998.
- [66]M. Bourogaoui, I. Jlassi, S. K. El Khil, and H. B. A. Sethom, "An effective encoder fault detection in pmsm drives at different speed ranges," in *Diagnostics for Electrical Machines, Power Electronics and Drives (SDEMPED)*, 2015 IEEE 10th International Symposium on. IEEE, pp. 90–96, 2015.
- [67]Kennel R., "Encoders for Simultaneous Sensing of Position and Speed in Electrical Drives with Digital Control," *IEEE Transactions on Industry Applications*, vol 43, no. 6, pp. 1572-1577, Nov/Dec 2007.
- [68]Yves Mollet and Johan Gyselinck, "Mechanical-state estimator for doubly-fed induction generators Application to encoder-fault tolerance and sensorless control," in *Electrical Machines (ICEM)*, 2014 International Conference on. IEEE, pp. 1-7, 2014.
- [69]B. Nahid-Mobarakeh, F. Meibody-Tabar, and F. Sargos, "Mechanical sensorless control of PMSM with online estimation of stator resistance," *IEEE Trans. Ind. Appl.*, vol. 40, no. 2, pp. 457–471, Mar./Apr. 2004.
- [70]M. Hinkkanen, T. Tuovinen, L. Harnefors and J. Luomi, "A Combined Position and Stator-Resistance Observer for Salient PMSM Drives: Design and Stability Analysis, " *IEEE Trans. Power Electron.*, vol. 27, no. 2, pp. 601-609, Feb. 2012.

Research Achievement

■ Journal Paper

1. DONGWOO LEE, and Kan Akatsu, "The Selection Method of Controller Gains for Position Sensorless Control of IPMSM Drives", IEEJ Journal of Industry Applications, Vol. 8, No. 4, pp.720-726, 2019.

■ International Conference Paper (with review)

2. D. Lee and K. Akatsu: "The study on gain selecting method of position sensorless control algorithm for IPMSM," in 2017 IEEE 12th International Conference on Power Electronics and Drive Systems (PEDS), pp.728-733, 2017.
3. D. Lee and K. Akatsu: "An improved speed and position estimator for transient performance of Back-EMF self-sensing for IPMSM," in 2018 The 44th Annual Conference of the IEEE Industrial Electronics Society (IECON2018), pp.397-402, 2018.
4. D. Lee and K. Akatsu: "The Study on Position Sensor Fault Detection and Algorithm Transition from Sensored to Sensorless Control for IPMSM," in 2019 International Conference on Power Electronics-ECCE Asia (ICPE 2019-ECCE Asia), 2019.
5. D. Lee and K. Akatsu: "An Improved Position Sensor Fault Detection and Algorithm Transition Using Adaptive Threshold for Sensorless Control of IPMSM," The 45th Annual Conference of the IEEE Industrial Electronics Society (IECON2019), 2019.10 (Pre-presentation).

■ International Symposium Paper (with review)

6. D. Lee and K. Akatsu: "The study on transient performance improvement of position sensorless control algorithm for IPMSM," in 2017 IEEE Symposium on Sensorless Control for Electrical Drives (SLED), pp.67-72, 2017

■ Domestic Paper (without review)

7. D. Lee and K. Akatsu: "The study on transient-state stability of sensorless control algorithm for PMSM without position sensor," 電気学会 モータドライブ-回転機/自動車合同研究会, 2016.07.
8. D. Lee and K. Akatsu: "The study on transient-state stability of sensorless control algorithm for PMSM without position sensor," 19th Power Electronics and Motion Control-Camp 2016, 2016.11.
9. D. Lee and K. Akatsu: "A study on relationship between the transient state and the overshoot rate of estimated position error," IEE-Japan Industry Applications Society Conference (JIASC2017), 2017.08
10. D. Lee and K. Akatsu: "A study on relationship between the transient state and the overshoot rate of estimated position error for Sensorless controlled IPMSM," 20th Power Electronics and Motion Control-Camp 2017, 2017.09.